



저작자표시-비영리-변경금지 2.0 대한민국

이용자는 아래의 조건을 따르는 경우에 한하여 자유롭게

- 이 저작물을 복제, 배포, 전송, 전시, 공연 및 방송할 수 있습니다.

다음과 같은 조건을 따라야 합니다:



저작자표시. 귀하는 원저작자를 표시하여야 합니다.



비영리. 귀하는 이 저작물을 영리 목적으로 이용할 수 없습니다.



변경금지. 귀하는 이 저작물을 개작, 변형 또는 가공할 수 없습니다.

- 귀하는, 이 저작물의 재이용이나 배포의 경우, 이 저작물에 적용된 이용허락조건을 명확하게 나타내어야 합니다.
- 저작권자로부터 별도의 허가를 받으면 이러한 조건들은 적용되지 않습니다.

저작권법에 따른 이용자의 권리는 위의 내용에 의하여 영향을 받지 않습니다.

이것은 [이용허락규약\(Legal Code\)](#)을 이해하기 쉽게 요약한 것입니다.

[Disclaimer](#)

Master of Science

***Optimization of Triboelectric Energy Harvesting from Falling Water
Droplet onto Wrinkled Polydimethylsiloxane-Reduced Graphene
Oxide Nanocomposite Surface***

Graduate School of the University of Ulsan

School of Mechanical & Automotive Engineering

ABU NAUSHAD PARVEZ

*Optimization of Triboelectric Energy Harvesting from Falling Water
Droplet onto Wrinkled Polydimethylsiloxane-Reduced Graphene
Oxide Nanocomposite Surface*

Supervisor: Professor **Kyoung Kwan Ahn**

A Thesis

Submitted to

the graduate school of University of Ulsan

in partial fulfillment of the requirements

for the degree of

Master of Science

in Mechanical & Automotive Engineering

By

Abu Naushad Parvez

School of Mechanical & Automotive Engineering

University of Ulsan, Ulsan, South Korea.

May 2019

***Optimization of Triboelectric Energy Harvesting from Falling Water
Droplet onto Wrinkled Polydimethylsiloxane-Reduced Graphene
Oxide Nanocomposite Surface***

This certifies that the Master's thesis of
Abu Naushad Parvez
has been approved by the following committee personnel



Committee Chair, Professor Byung Ryong Lee



Committee Member, Professor Soon Young Yang



Committee Member, Professor Kyoung Kwan Ahn

School of Mechanical & Automotive Engineering

University of Ulsan

Ulsan, South Korea

May 2019

ABU NAUSHAD PARVEZ 의
공학석사 학위 논문을 인준함

심사위원

이병룡



심사위원

양순용



심사위원

안경관



울산대학교 대학원

기계자동차공학과

2019 년 05월

Acknowledgement

All praise and gratitude belong to the Almighty Allah (SWT). Without His blessings nothing would be possible so far.

I would like to express my sincere thanks and appreciation to my advisor Professor Kyoung Kwan Ahn (of School of Mechanical & Automotive Engineering at University of Ulsan) for his kind guidance, continuous support, supervision and persistent motivation throughout the duration of my graduate study and research. Furthermore, his open-minded attitude towards research, amiability and flexibility also assisted me to broaden the horizon of my thinking and to do creative works without much hindrance. Along with my advisor, I am also very thankful to the thesis committee members: Professor Kyoung Kwan Ahn, Professor Byung Ryong Lee, Professor Soon Young Yang for their valuable comments, insightful suggestion and encouragement to improve the quality of my research considering broader prospects.

My following sincere gratefulness goes to University of Ulsan for providing me with a very wonderful environment to pursue my academic study and research. The diverse community of this university also has unlocked a greater scope for me to know, communicate and work with people of different nationalities from all around the world. This will help me to suit myself with different environment either in academic research or in professional career in the upcoming future. Moreover, my heartiest thanks to the course instructors of this university, who not only delivered their lecture in the best way possible but also their direction and crucial discussion on educative contents have imparted me with an insight to think and work efficiently. Besides, my cordial thanks go to National Research Foundation (NRF) of Korea and Brain of Korea 21 (BK 21) plus for supporting me financially throughout my study period.

I am also grateful to Professor Hyeon Cheol Kim and Mr. Md Habibur Rahaman of Smart Microsystems Laboratory of School of Electrical Engineering for their kind support and assistance during performing several experiments on this very work with them. Especially, I would like to thank Mr. Md Habibur for his time, effort and crucial suggestions in several stages of my research.

Last but not least, my special gratitude goes to my parents, who worked really hard to raise me up and sacrificed a lot in their life to help me achieve everything whatever I have gained so far. Particularly, I am thankful to my mother who worked and is still working as a lifelong mentor and guide for me. Her support, affection and dedication worked as an impetus for me to aim for the best in life and to come this far. I also would like to thank my other family members for their continuous support and blessings.

Abu Naushad Parvez

University of Ulsan

May, 2019

Abstract

This thesis investigates the triboelectric energy harvesting phenomenon of falling water droplets on a novel nanocomposite surface, chemically synthesized from reduced graphene oxide (rGO) and polydimethylsiloxane (PDMS) polymer. Filler amount variations in pristine polymer matrix and their effect on the resultant triboelectric films have been investigated thoroughly while vertically falling consecutive water droplets contact and slide over the as synthesized triboelectric nanocomposite film surfaces. Based on the output performance, proper optimization has been made and explained theoretically with respect to the effect of filler incorporation

Six nanocomposite samples have been prepared by varying filler's concentration in polymer matrix to optimize the triboelectric performance. Optimization has been explained based on determination of several parameters e.g. rGO flakes' thickness, water contact angles, dielectric properties, and nano-characterization of the pristine and nanocomposite film samples. Several nano-characterization technique includes Field Emission Scanning Electron Microscopy (FE-SEM) for the analysis of surface and cross-sectional morphologies, Energy-Dispersive X-ray (EDX) spectroscopy for quantitative elemental analysis, and confocal Raman spectroscopy have been performed to analyze the as prepared samples for critical optimization.

In addition, thickness effect of as prepared films has also been studied by varying the thickness. After analyzing outputs of a single electrode mode triboelectric nanogenerator (SEM-TENG) based on Pristine PDMS and nanocomposite samples, it has been found that thinner films perform better in comparison to apparently thicker films. Moreover, it has been also investigated that lower quantity of filler inclusion can impart the best desired triboelectric properties to resultant nanocomposite matrix than higher amount of filler comprehended matrix. After proper

optimization, it has been found that 0.5 mg rGO incorporated PDMS matrix of 141 μm thickness revealed highest output potential difference of $\sim 2\text{V}$ upon contact and separation of water droplet over the nanocomposite film surface. The maximum close circuit current (I_{SC}) value has been obtained $\sim 2\text{ nA}$ from triboelectrification for the same sample.

This work demonstrates a unique way to get a hydrophobic surface and improved dielectric thin triboelectric nanocomposite film simultaneously by optimizing rGO filler inclusion in PDMS matrix, which is able to harvest energy from a tiny moving water droplet.

Contents

Abstract	1
Chapter 1	8
Introduction	8
1.1 Organization of Thesis	8
1.2 Motivation and purpose of this research	9
1.3 Objectives of this research	13
Chapter 2	15
Literature Review	15
2.1 Energy Harvesting	15
2.1.1 What is energy harvesting?	15
2.1.2 Importance of Energy Harvesting	16
2.1.3 Methods of Vibration Energy Harvesting	18
2.2 Detail Analysis on Triboelectrification	24
I. Electron Transfer Mechanism	25
II. Ion Transfer Mechanism	26
III. Material Transfer Mechanism	26
2.3 Working Modes and Mechanism of Triboelectric Nanogenerator	27
a) Vertical Contact Separation Mode	27
b) In-plane Sliding Mode	30
c) Single Electrode Mode	32
2.4 State-of-art Overview of Devices Structures based on purpose of applications	38
2.4.1 TENG-based on Biokinetic Energy Harvesting	39
2.4.2 TENG-based on Wind Energy Harvesting	42
2.4.3 TENG-based on Liquid Energy Harvesting	45
Drawbacks of previous works and Originality of the present work	56
Chapter 3	57
Experimental Procedures and Material Characterization	57
3.1 Experimental Procedures	57
3.1.1 Materials	59
3.1.2 Preparation of PDMS-rGO nanocomposite solution	59

3.1.3	Fabrication of Single Electrode Mode TENG	59
3.2	Quantitative Measurements & Material Characterization.....	61
3.2.1	Scanning Electron Microscopy (SEM)	62
3.2.2	Energy-Dispersive X-ray (EDX) Spectroscopy	63
3.2.3	Fourier Transformed Infrared (FTIR) spectroscopy	63
3.2.4	Raman Spectroscopy.....	64
3.2.5	Confocal Microscopy.....	64
3.2.6	Water Contact Angle	64
3.2.6	X-ray Photoelectron Spectroscopy	65
Chapter 4	66
Analysis of Results and Working Mechanism.....		66
4.1	Results and Discussion.....	66
4.2	Working Mechanism	85
Chapter 5	92
Conclusion and Future Work Direction		92
5.1	Conclusion.....	92
5.2	Future Work Direction	92
5.3	Publications	93
References	94

Table of Figures

Fig. 1 Fundamental working principle of Vertical Contact Separation Mode TENG (a) Open-circuit condition (b) Short-Circuit Condition	29
Fig. 2: Theoretical model for dielectric to dielectric vertical contact separation mode TENG ...	30
Fig. 3. Schematics of in-plane sliding mode- TENG.....	31
Fig. 4 (a): Schematics of Single-electrode Mode TENG based on in-plane sliding	33
Fig. 4(b): Schematics of Single-electrode Mode TENG on vertical contact separation	34
Fig. 6: Free-standing layer (a) device structure; (b) contact sliding mode between dielectric-to-conductor; (c) non-contact sliding mode between dielectric-to-conductor; and (d) contact sliding mode between dielectric-to-dielectric.....	37
Fig 7: (a) schematic illustration of working mechanism and real-time photographs of TEG working upon bending and releasing process, (b) Electrical Outputs of the as fabricated TEG device	39
Fig. 8: (a) schematics of TENG structure, and (b) electrical outputs representation.	40
Fig. 9: (a,b) Schematics and real-time device structure; (c) TENG device placement in shoe insole; and (d) 30 white LED light lighting during device operation upon stepping up onto and stepping down from shoe insole	41
Fig. 10: (a) Schematics TENG device; (b) measured weight of TENG device; (c) optical image of the prepared TENG; and (d) lighting of 20 LED lights powered by finger tapping	42
Fig. 11: (a) Schematics of TENG device; (b) PANI NFs grown on Kapton film; (c) Top view of the TENG structure; (d, e) side view of fabricated device; and (f) lighting of 58 LEDs when mouth blown air is used and 1240 LEDs were lit up when 15 m/s wind speed was passed	43
Fig. 12: (a) wind-cup device schematics; and (b) Real-time setup	44
Fig. 13: Rotating TENG structure using micro-patterned electrode	45
Fig. 14: (a) device structure; (b) working mechanism; and (c) output performances using tap, DI water and NaCl solution.....	47
Fig.15. (a) Synthesis procedure of PRNC thin film (b) SEM-TENG structure.....	61
Fig 16. Optical Images of (a) Pristine PDMS films (thickness 141 μm , 149 μm and 537 μm respectively-from left to right); (b) 0.5 PRNC films (thickness 149 μm , 537 μm and 141 μm respectively-from left to right); (c) 0.8 PRNC, 1.2 PRNC, 1.8 PRNC and 2.8 PRNC films respectively with 141 μm thickness- from left to right and; and (d) Real SEM-TENG device ...	61

Fig.17. EDS elemental analysis of (a) Pristine PDMS, (b) 0.5 PRNC, (c) 0.8 PRNC, (d) 1.2 PRNC, (e) 1.8 PRNC, and (f) 2.8 PRNC	67
Fig. 18. FE-SEM surface images of (a) Pristine PDMS, (b) 0.5 PRNC, (c) 0.8 PRNC, (d) 1.2 PRNC, (e) 1.8 PRNC, and (f) 2.8 PRNC	69
Fig. 19. Optical water-contact angle images of (a) Pristine PDMS, (b) 0.5 PRNC, (c) 0.8 PRNC, (d) 1.2 PRNC, (e) 1.8 PRNC, and (f) 2.8 PRNC	69
Fig. 20. FE-SEM cross-section images of (a) Pristine PDMS, (b) 0.5 PRNC, (c) 0.8 PRNC, (d) 1.2 PRNC, (e) 1.8 PRNC, and (f) 2.8 PRNC	70
Fig. 21. Confocal Raman Spectroscopy	72
Fig. 22. FTIR Spectra of pristine PDMS and nanocomposite films.....	73
Fig. 23. XPS survey scan spectra for Pristine PDMS and nanocomposite films.....	75
Fig. 24. XPS Core spectra for (a) Pristine PDMS; (b) 0.5 PRNC; (c) 0.8 PRNC; (d) 1.2 PRNC; (e) 1.8 PRNC; and (f) 2.8 PRNC.	77
Fig. 25. Average rGO flakes' thickness for (a) 0.5 mg, (b) 0.8 mg, (c) 1.2 mg, (d) 1.8 mg and (e) 2.8 mg	78
Fig. 26. Open Circuit Voltage (V_{OC}) of (a) Pristine PDMS, (b) 0.5 PRNC, (c) 0.8 PRNC, (d) 1.2 PRNC, (e) 1.8 PRNC, and (f) 2.8 PRNC	80
Fig. 27. (a) Dielectric Constant, (b) AC conductivity	82
Fig. 28. (a,b,c) SEM Cross-sectional thickness of gradually thinning films	83
Fig. 29. Open Circuit Voltage (V_{OC}) comparison of Pristine PDMS with thickness variation	84
Fig. 30 Open Circuit Voltage (V_{OC}) comparison of 0.5 PRNC with thickness variation.....	84
Fig. 31. Open Circuit Voltage (V_{OC}) of PP with (a) 537 μm , (b) 149 μm (c) 141 μm	85
Fig. 32. Open Circuit Voltage (V_{OC}) of 0.5 PRNC with (a) 537 μm , (b) 149 μm (c) 141 μm	85
Fig. 33. working mechanism of SEM-TENG device (a) when droplet was pre-charged due to triboelectrification with Pipette/air, (b) when contact electrification occurred between droplet and thin triboelectric films, and (c) micro-capacitor model due to optimized filler addition.	88
property and capacitance of the matrix. The capacitance of this new nanocomposite can be estimated by the following equation:	89
Fig. 34. Close Circuit Current (I_{SC}) of (a) Pristine PDMS, (b) 0.5 PRNC, (c) 0.8 PRNC, (d) 1.2 PRNC, (e) 1.8 PRNC, and (f) 2.8 PRNC	91

List of Tables

Table 1: Triboelectric Series of Some Common Materials.....	22
Table 2. State-of-art Works on Solid -water contact triboelectrification.....	47
Table 3: Recently reported articles on droplet-solid surface contact based triboelectrification ..	52
Table 4. EDS elemental analysis.....	67
Table 5. XPS analysis results for Pristine PDMS and nanocomposite samples	77
Table 6. Average and Maximum thickness of dispersed rGO flakes with varied quantity.....	78
Table 7. Dielectric Constant and Capacitance of as synthesized films	89

Chapter 1

Introduction

This very chapter is focused on illustrating the organization of this full thesis work, literature review and state-of-the-art of the related works, motivation and objectives of this thesis. The complete chapter is categorized in three sections, which include organization of thesis, literature review, and objectives

1.1 Organization of Thesis

This thesis has been organized according the theoretical investigation and experimental findings conducted by the author. The theoretical representation includes several hypothesis to comply with the found phenomenon, assumptions and formulation of several parameters to explain everything in a prudent way. These hypothesis and assumptions have been further clarified using several material characterization techniques. Further justification has been made by the experimental outputs of the fabricated devices. The author has tried to demonstrate that how lower quantity of graphene derivative filler incorporated polymer nanocomposite matrix can give optimized energy harvesting output from sliding tiny water droplet sliding over its surface. The organization has been made as follows:

- Chapter 1: Introduction

This chapter introduces the need, purpose and summary of this whole work in brief for proper comprehension of the following chapters

- Chapter 2: Literature Review

Background study of energy harvesting techniques, triboelectrification, working modes of triboelectric nanogenerator, state-of-art of triboelectric energy harvesting from different kinetic motions around us and finally recent progress on liquid energy harvesting have been explained in detail in this chapter.

- Chapter 3: Experimental Procedures and Material Characterization

In this section, description of the used materials, polymer/filler nanocomposite synthesis procedure, triboelectric energy harvesting device fabrication, all the performance measuring and nano-characterization equipment have been addressed clearly.

- Chapter 4: Analysis of Results and Working Mechanism

Analysis of the obtained experimental results have been explained here with logical reasoning and evidences found from appropriate characterization of the as prepared samples

- Chapter 6: Conclusion

Outcome of this research has been stated in a nutshell. Moreover, some suggestions have been made based on reasonable assumptions to improve the performance of this proposed triboelectric nanogenerator. In addition, publications and references have been put at the end of this chapter.

1.2 Motivation and purpose of this research

Consumption of petroleum fuels to an extensive degree not only contaminates our present environment but also causes detrimental climate change in the upcoming future. Moreover, due to

continuous depletion of this finite resource, price hike will also be occurring in the upcoming future. To address all these issues, researchers are now putting their concern on harvesting renewable and clean energy ubiquitous around us. This drives them to develop new technology to utilize those omnipresent energy in usable form. Nanogenerators are one of the most efficient approaches that have been promoted to harvest the ambient energy [1]. Several nanogenerators named as piezoelectric [2–4], triboelectric [5–8] and pyroelectric [9–11] nanogenerators have been developed so far to collect the mechanically available energy in the environment and to convert this in electrical energy following their individual working principle. Among these proposed nanodevices, TENGs are very efficient in its own way, which work based on the conjugation of triboelectrification and electrostatic induction [12]. Triboelectric phenomenon is explained by the generation of electrical energy when two materials of unlike polarities come in contact with each other through friction [13]. Continuous output can be generated by establishing potential difference during periodic contact-separation [14]. This contact separation basically happens based on four fundamental modes, which can be named as Vertical contact separation mode [7,15–17], Lateral sliding mode [18–21], Single electrode mode [22–25], free standing layer mode [26,27]. TENG can efficiently harvest mechanical energy available from human motion [28–31], wind energy [32–34], wave energy [35–38], mechanical vibration & rotation [39–41] etc. for utilizing these collected energy to power up sensors [42–44], wearable electronics [28,30,31] and other nanodevices [45].

It has already been well-established that the output performance of TENG is quite dependent on the contact materials' interfacial surface state. Therefore, choice of materials itself is a very pivotal step to fabricate an efficient TENG device. According to triboelectric series proposed in literature [14], materials are well-organized according to their affinity to lose or gain electrons upon mutual

contact. Among them PDMS is one of the most frequently used tribo-surfaces because of higher electronegativity, transparency, flexibility, biocompatibility and its adaptability to make any desired structures [46]. To increase the efficiency of PDMS to be used as a triboelectric polymer, several research efforts- like growing varied shaped nano/micro-structures to increase surface roughness [47,48], injection of ions [49], plasma etching [50], filling high dielectric nanoparticles [46] or carbon based nanofillers [23,50–53] for increasing the capacitance- have been made so far. Harchana et al. have recently proposed a surfactant incorporated PDMS-graphene oxide (GO) based porous composite structure, which enhanced the output performance three times higher than flat PDMS film [54]. In addition, carbon nanotubes (CNTs) and multi-wall carbon nanotubes (MWCNTs) have been used as nanofillers in PDMS matrix in order to tune higher internal resistance of pristine polymer matrix, to increase surface charge density so that the enhanced output energy can be applied to charge capacitors and to power sensors or LED lights [50,51] etc. Furthermore, several works have been reported on using GO layer as triboelectric surface, growing several number of graphene layers on a substrate to find the triboelectric effect and GO doped with nanofiber mats to produce a better triboelectric phenomenon [5,55,56] and so on.

Given most of the earlier mentioned works have been focused on solid-solid (SS) contact based TENG, where contact frequency, contact force and contact areas were quite higher, as they were controlled manually, to bring about a surge in TENG's performance. But such controlled phenomenon is quite difficult to obtain while aiming for harvesting energy available in nature e.g. solar energy, wind energy, raindrops etc. In this work, our research is mainly concerned on harvesting energy from moving water droplets, which is clearly very much related to the nature of raindrops. Different research groups have already put their concern on droplet energy harvesting, and they have certainly come up with improved outputs by following their own way of fabricating

superhydrophobic polymer surface. However, most of those efforts have been given on growing complicated micro/nano structures [57–59], micro/nanowires [60], creating layer of superhydrophobic nanoparticles [61] etc. to increase water repellency on surface-which require sophisticated and costly techniques for implementation. Furthermore, the above-mentioned research did not show any effect of thickness variation of triboelectric film on device performance. Recently, Kwak et al. and coworkers have reported a TENG, which has the ability to generate large amount of power from the movement of a single droplet over a monolayer of graphene deposited on PTFE [62]. This work has certain limitations like the droplet was moved forcefully by manual interference and the spread of droplet over the surface proved that the surface lacked hydrophobicity. A recent work on graphene's attraction to water [63] (hydrophilicity) further confirmed that this work failed to consider real life application. Considering such drawbacks, we considered to work on a novel nanocomposite structure and several parameters of the proposed nanocomposite film was taken into account to harvest energy from the droplet movement over it. In this work, rGO was selected as filler material due to its unique properties and structure [64]. In addition, its higher electronegativity compared to graphene and other carbon nanofillers [65,66], simple synthesis technique and long lasting storage potential without agglomeration than pure graphene and carbon nanotubes, electron trapping potentiality [67] and higher capacitance [66,68] offer a great compatibility to be used as filler in triboelectric polymers to improve the energy harvesting performance. The optimized oxygen containing functional groups also impart it better dispersion, higher electrical conductivity and less adsorption [66,69–71]. These functional groups also possibly may bless this graphene derivative with the utility to create bonding with its host matrix for electrical/mechanical property improvement, whereas graphene/other carbon nanofillers do not have such functional groups in their pristine condition [72]. Moreover, optimized

conductivity of rGO mostly avoids the risk of dielectric breakdown, which may happen for highly conductive graphene [73], carbon nanospheres [74], carbon nanotube [75] filler included composites at a very lower percolation threshold. Furthermore, while graphene oxide (GO) has poor conductivity, higher hydrophilicity due to presence of numerous oxygen based functional groups [76–78], rGO has comparatively higher conductivity and hydrophobicity because of the reduction of these functional groups. Owing to such interesting properties of rGO, the effect of this filler in PDMS matrix was studied to optimize the desired triboelectric properties by varying the filler concentration. Six PDMS-rGO nanocomposite (PRNC) samples were prepared in this regard by using lower quantity of filler addition i.e. 0 mg, 0.5 mg, 0.8 mg, 1.2 mg, 1.8 mg, 2.8 mg. Optimization was made based on nano characterization of these filler integrated nanocomposites, contact angle measurement, dielectric property assessment and most importantly on device outputs. Variation of thickness of these as fabricated nanocomposites was made as well to examine its effect on device performance. Finally, a SEM-TENG has been presented in this paper based on PRNC film-water droplet contact electrification.

1.3 Objectives of this research

In this research, we have proposed a novel triboelectric nanocomposite surface for harvesting energy generated due to triboelectrification while a minuscule droplet is sliding and rolling off the proposed surface. Therefore, the diminutive mechanical motion can be converted in to electrical energy, which is the prime motive of Nano energy harvesting. Since hydrophobicity and other properties should be optimized of the nanocomposite film for making a proper optimization, the objectives of this study include the following-

- Optimization of hydrophobicity due to addition of fillers in polymer matrix
- Ensuring better dispersion, alignment and interaction of filler in polymer matrix

- Checking the dielectric properties (dielectric constant, ac conductivity) and capacitance effect for the prepared nanocomposite samples
- Filler size optimization for imparting the resultant nanocomposite matrix the above-mentioned favorable properties
- In addition, the effect of film thickness on energy harvesting output has also been considered
- Finally, considering all the aforementioned parameters and the measured output performance, a comparison has been made and an optimized condition has been suggested for triboelectric energy harvesting of this proposed phenomenon.

Chapter 2

Literature Review

2.1 Energy Harvesting

2.1.1 What is energy harvesting?

Scavenging of energy or power is usually termed as energy harvesting, in which process energy from the omnipresent environment is converted into another form for utilizing it for some specific purposes. For example, in electrical power generation facility when the strong water stream hit the turbine blades planted, which consequently moves and gives rotation motion to the connected shaft mounted in a generator. This shaft subsequently creates varying magnetic flux and produces electricity in that generator. Another example can be provided, where wind turbine does the same thing by utilizing the higher wind flow instead. In the very recent past, preceding wind turbine, windmill was used for milling grains, pumping water or sawing woods by using strong force of wind. However, these energy harvesting techniques require fixed spacious place, sophisticated and expensive setup, processes as well as higher maintenance cost to continue their operation. Therefore, in modern days, energy harvesting and storage has been addressed in a very miniature range and several portable devices have already been introduced to harness the ubiquitous energy around us [1–11].

In our surrounding atmosphere, energy usually exists in ambient form e.g. heat/thermal energy, solar energy, wind energy, kinetic/vibration energy. Although there are special methods for harvesting each type of energy, most of those available energy are not regularly available due change in environmental condition in different times and places, and day-night cyclic rules [79]. Among them only heat/thermal energy and mechanical energy can be found with more availability,

and regardless of weather and location restrictions. Since the focus of this study is to harvest energy from mechanical/vibration, therefore in detail study on this energy harvesting will be concerned onwards. There are several methods [80–82] have been proposed so far for harvesting energy even from a subtle kinetic/mechanical motion or vibration and to convert it in to useful electrical energy. These methods are piezoelectric energy harvesting [83–85], triboelectric energy harvesting [5–8,12–15], electromagnetic energy harvesting [86–88] and electrostatic energy harvesting [79,89,90]. These methods will be described in brief individually and the triboelectric energy harvesting will be discussed thoroughly in particular as this work has been conducted on this special type of energy harvesting.

2.1.2 Importance of Energy Harvesting

First of all, the most crucial energy source “Fossil Fuels” of the present time is not an efficient solution for future energy needs. The report from World Energy Outlook (WEO) 2007 already has claimed that fossil fuel will be sufficient to meet the energy demand until 2030 if its consumption is retained at the same rate as it is now [91]. The consequence of this depletion can result in detrimental effect. It has been predicted that if we run out of this resource, the production of food, plants for water distribution/refining and other systems might be collapsed. Furthermore, the powerplants which are run by petroleum fuel will lose their productivity and electricity generation will be cut short as a consequence. The transportation system will suffer the most as well due to continuous depletion of fossil fuels as most of the vehicles running on the road use petrol, diesel or gasoline as prime source to put their engine in operation. Along with the upcoming scarcity, there are several negative impacts of using fossil fuels. Due to continuous use of fossil fuels noticeable amount of CO₂, CO, SO₂, NO_x are continuously being added to the atmosphere. It is already known that the prevailing greenhouse gas effect is accelerated by CO₂ gas and almost 70%

of CO₂ emissions are due to the combustion of fossil fuels [92]. This increasing greenhouse effect is endangering the mankind and other animal kingdom by raising the temperature every year. Nowadays several new papers have reported that excessive heatwaves are striking several parts of the world due to the worsened global warming impact, which consequently. To keep the situation in limit, it has been proposed that the use of petroleum fuels should be in limit although the world has mass of amount of reserves for now. McGlade et al. suggested that if 1/3 of oil, 1/2 of natural gas and 80% of coal reserves are kept unused between 2010 and 2050, then the global warming can be limited by 2°C [93]. However, the real scenario always vary with the estimated scenario and such controlled use is sometimes not plausible to achieve. Moreover, the processing of fossil fuels from mining to emission form also causes several disadvantages like land degradation, water pollution, acidification of ocean. These not only damage the human life but also the wild habitats and marine lives. Therefore, some clean and renewable solutions are urgently required to meet up the energy demand as well as to save the world from being perished before time.

In addition, most of the electricity generation infrastructure, currently in operation, are not very efficient as their energy conversion loss is extremely high. For example, while gas/steam turbines convert the input gas/stream into electricity, 2/3 of total input energy are lost as heat energy. Moreover, the incandescent light bulbs squander 99% of the total input electrical energy by dissipating it as heat. That much loss is unacceptable and therefore by 2014 most of the developed nations have phased out these bulbs and replaced it with energy saving bulbs [94]. The most convenient devices we use in our regular life e.g. computers, laptops, tablets, smartphones etc are also a great instance for energy loss as well since they dissipate a significant amount of heat as waste while running. Furthermore, vibration generated during refrigerator, engine operation is also undesired and can be considered as waste energy. In this context, some efficient materials and

technological improvement can be a suitable choice to utilize these waste energies and to convert it in to useful energy. Additionally, the commonly used batteries in electronic devices are not an efficient way to power those devices as batteries have limited life time and get exhausted completely after a certain period. Nowadays, several extreme accidents are being occurred due to hazardous battery condition and it costs even lives in worst case scenario. Different research works conducted in very recent time have already shown that energy can be harvested from the vibration energy sources e.g. walking, running, body parts movements and even from rain drops (already mentioned with reference in INTRODUCTION section). These multiple forms of energy can be stored and supplied to power wearable devices, which indicates the “no need of battery” days are not far away. These several forms of energy, which are usually wasted beyond our knowledge, can be an inexhaustible resource for the battery-free applications.

2.1.3 Methods of Vibration Energy Harvesting

Piezoelectric Energy Harvesting

In order to introduce piezoelectric energy harvesting, it is important to define piezoelectricity beforehand for proper understanding on this phenomenon. Piezoelectricity is defined as the generation of electricity/electric charge accumulated in a target material, when it becomes polarized under the application of certain mechanical strain. Such piezoelectric materials are classified into inorganic piezoelectric materials, bio-piezoelectric materials and piezoelectric polymers. Piezoelectric inorganics include piezoelectric crystals (such as quartz film and ZnO nanowires) [95,96] and piezoelectric ceramics (such as Barium Titanate [BaTiO₃], Lead Zirconate Titanate (PZT- Pb[Zr_xTi_{1-x}]O₃), Strontium Titanate (SrTiO₃), etc. [96]). Piezoelectric polymer like PVDF and its co-polymer P(VDF-TrFE) has favorable energy harvesting potentials [97–100]. The most popular piezoelectric materials are PZT and PVDF, although each has its own advantages

and drawbacks [101]. The next category is bio-piezoelectric materials e.g. various viruses, silks and bones, which also demonstrate a possible approach for energy harvesting although their usability lasts only for short period and output performance is quite lower in comparison to the aforementioned choices [96]. Beyond these materials, a new class of materials has been invented i.e. piezoelectric foams, which are literally a porous structure and shows piezoelectric properties. This type of piezoelectric responsive matrix is made of polymers usually treated with corona discharge. Piezoelectric foams have higher mechanical strength and are therefore very convenient for vibration energy harvesting [101–103]. Anton et. al have shown that most of these porous piezoelectric matrix structure were fabricated from polymers like Polyethylene Terephthalate (PET) and Polypropylene (PP) [101].

Electrostatic Energy Harvesting

This energy harvesting typically uses structures comprised of two parallel metal plates separated by dielectric or insulator medium [80]. An electrical field is generated between two plates by charging these plates, using external power supply source, with opposite polarities. Electrostatic effect occurred between the plates of the capacitor induces electrical charge storage. Moreover, physical separation of one conductor plate is needed, while the other will be fixed, to generate current. This movement of the plate is made by mechanical vibration [104]. This capacitor structure is quite suitable for microelectromechanical systems (MEMS) and for low frequency energy harvesting applications [105]. Moreover, flexibility of size modification to increase power density, low fabrication cost and higher output voltage generation potential make this energy harvesting probably an efficient option [105]. Considering the negative aspect for this energy harvesting device due to the necessity of external voltage supply, a permanent polarized dielectric material was proposed by Sterken et. al to overcome this limitation [106]. However, this electret

materials degrade overtime. However, dielectric breakdown, lower capacitance, existing external power source requirement and higher internal resistance [105] resist its applicability to most of the sources of vibration energy other than MEMS devices.

Electromagnetic Energy Harvesting

This energy harvesting technique is solely based on Faraday's law of electromagnetic induction. This law states that when an electrically conductive coil is placed within a magnetic field, then the movement of the coil or change in magnetic flux of the dominant magnetic field will induce electrical charge flow in the conductor coil [107]. This principle can be applied to harvest the vibrational energy from the numerous ambient resources available in the atmosphere. If the ambient vibration is connected with the moving part of electromagnetic system, then electrical energy will be obtained intermittently as long as the movement of coil and magnetic field are retained in the uniform condition [82]. Although several materials choices are available for this energy harvesting technique and unlike electrostatic energy harvesting devices it does not require any separate voltage source, the circuit is quite complex to integrate with small devices. In addition, a permanent magnet is always needed to retain the magnetic field intact, which is very bulky and therefore arduous to mount in micro/nano devices [86,108]. Moreover, it has significant ohmic losses in the conductive coils, lower efficiencies when being operated in lower frequencies [105]. The lower results from electromagnetic energy harvesting results also indicate its ineffectiveness for the widespread use as to do such various additional equipment will be required for its continuous operation [108].

Triboelectric Energy Harvesting

Triboelectric energy harvesting is a very novel energy scavenging technique, which has been invented by professor Zhong Lin Wang's group in 2012 at Georgia TECH [109] to harvest the nanoscale level energy. The working principle of this very technique lies in conversion of ambient mechanical/kinetic energy in to electrical energy based on the conjugation of triboelectrification and electrostatic induction [12]. Triboelectrification occurs when two different materials come in contact with each other through friction. This friction results in charging of two surfaces with opposite polarities. These charges remain on the surfaces since charge cannot flow in the dielectric medium and therefore, they are called as "static charges". These static charges induce potential difference between the electrodes of two contacting surfaces. Therefore, uninterrupted flow of electrons in the outer circuit occurs when there is periodic contact and separation between the surfaces. The amount of electric charge flow depends on the electron attracting or donating affinities of the contact materials. Therefore, depending on this property, a new series of materials [14] have been presented in **Table 1**. The series is named "Triboelectric Series". The color code in the arrow clearly indicates the gradual progress towards the most positive and negative triboelectric materials choices. The positive materials act as electron donor, while the negative materials has tendency to receive electrons. Moreover, the relative position of the materials in the given series also can anticipate the intensity of charges generated upon friction of the two contact surfaces. As much further as the materials go from the central section of the table, charge density becomes higher on the surface after contact electrification due to the chemical properties of the materials. Although all these enlisted ones and unlisted materials can be used as triboelectric surface materials, most of the reported TENG structures are made from polydimethylsiloxane (PDMS), Polytetrafluoroethylene (PTFE), Polyvinylidene Fluoride (PVDF) which when attached with conductor materials such as Gold (Au), Silver (Ag), Aluminum (Al), Copper (Cu) can yield

the best material combinations [14,110]. Therefore, depending upon the application, several materials options can be selected for fabricating numerous TENG Devices.

Table 1: Triboelectric Series of Some Common Materials

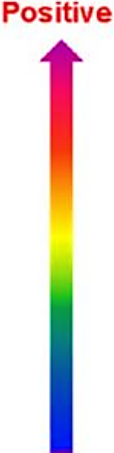
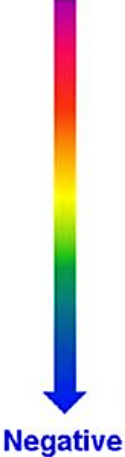
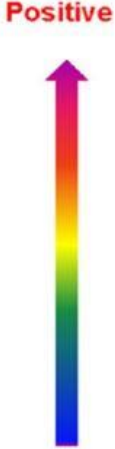
	Polyformaldehyde 1.3-1.4	(continued)	
	Etylcellulose	Polyester (Dacron)	
	Polyamide 11	Polyisobutylene	
	Polyamide 6-6	Polyurethane flexible sponge	
	Melanime formol	Polyethylene Terephthalate	
	Wool, knitted	Polyvinyl butyral	
	Silk, woven	Polychlorobutadiene	
	Aluminum	Natural rubber	
	paper	Polyacrilonitrile	
	Cotton, woven	Acrylonitrile-vinyl chloride	
	Steel	Polybisphenol carbonate	
	Wood	Polychloroether	
	Hard rubber	Polyvinylidene chloride (Saran)	
	Nickel, copper	Polystyrene	
	Sulfur	Polyethylene	
	Brass, silver	Polypropylene	
	Acetate, Rayon	Polyimide (Kapton)	
	Polymethyl methacrylate (Lucite)	Polyvinyl Chloride (PVC)	
	Polyvinyl alcohol	Polydimethylsiloxane (PDMS)	
	(continued)	Polytetrafluoroethylene (Teflon)	

Table 1 (Continued)

	Aniline-formol resin	Polyvinyl alcohol	
	Polyformaldehyde 1.3-1.4	Polyester (Dacron) (PET)	
	Etylcellulose	Polyisobutylene	
	Polyamide 11	Polyuretane flexible sponge	
	Polyamide 6-6	Polyethylene terephthalate	
	Melanime formol	Polyvinyl butyral	
	Wool, knitted	Formo-phenolique, hardened	
	Silk, woven	Polychlorobutadiene	
	Polyethylene glycol succinate	Butadiene-acrylonitrile copolymer	
	Cellulose	Nature rubber	
	Cellulose acetate	Polyacrilonitrile	
	Polyethylene glycol adipate	Acrylonitrile-vinyl chloride	
	Polydiallyl phthalate	Polybisphenol carbonate	
	Cellulose (regenerated) sponge	Polychloroether	
	Cotton, woven	Polyvinylidene chloride (Saran)	
	Polyurethane elastomer	Poly(2,6-dimethyl polyphenyleneoxide)	
	Styrene-acrylonitrile copolymer	Polystyrene	
	Styrene-butadiene copolymer	Polyethylene	
	Wood	Polypropylene	
	Hard rubber	Polydiphenyl propane carbonate	
	Acetate, Rayon	Polyimide (Kapton)	
	Polymethyl methacrylate (Lucite)	Polyethylene terephthalate	
	Polyvinyl alcohol	Polyvinyl Chloride (PVC)	
	(continued)	Polytrifluorochloroethylene	
		Polytetrafluoroethylene (Teflon)	

Along with the listed materials in the above-mentioned **Table 1**, surface morphologies and matrix structure were studied and modified by using physical and chemical modification techniques to boost up TENG's output performance. Various physical modification techniques like micro/nano patterning-pyramid, square, hemispherical, nanowire shaped structure have been grown on the surface for enhancing the efficient contact area, which consequently provide better output results

for energy harvesting. [60,111]. In addition, functionalization of surface e.g. ion injection, nanoparticle deposition etc. has been proven to offer a great potential to invigorate the pristine triboelectric surfaces [49,61,112]. Furthermore, composites made of fillers- like carbon or graphene nano/micro-shaped derivatives/ceramic/conductive nanoparticles- and polymer matrices have been proposed as contact surfaces, which not only bless the contact electrification but also boost the dielectric properties and energy storage capacity of the devices [46,52–54,67].

2.2 Detail Analysis on Triboelectrification

The term “Triboelectrification” is solely integrated to “Contact Electrification”. This can be defined as “generation of electrical charges upon contact and separation of two identical or different materials” [113]. Although for some industries including electronics, aerospace, automotive or polymer etc, this is quite undesirable, this is very beneficial for electrostatic coating, triboelectric energy harvesting generators/nanogenerators. Since this research is concerned on providing deep insight in triboelectric energy harvesting, therefore contact electrification will be addressed to discuss this specific energy harvesting scenario. In this case, contact electrification between identical materials is not efficient as this phenomenon does not convincingly let the electron flow due to same polarity of the generated electrical charges. Thus, the objective of obtaining energy gets failed, Therefore, materials with further unlike polarities are more preferred for gaining better triboelectrification upon contact-separation. The possible combination of materials could be metals, semiconductors or polymers (ionic/non-ionic). Among which contact electrification phenomenon between metals and semiconductors have been well-addressed [114–116] and charge transfer mechanism between metal-metal surface contact has already been explained by McCarty et. al [116]. However, the exact charge transfer mechanism between

dielectric-dielectric polymers remained vague and therefore the exact mechanism working behind the triboelectric output is questionable till date. Most of the polymers in triboelectric series do not have any ions on their surface unlike the ionic polymers and thus transfer of ions is not possible when two materials come in contact. However, it has already been observed that charge transfer happens when two non-ionic polymers contact each other. Therefore, it can be anticipated that there are some charge transfer mechanisms being involved in there. Three mechanisms have been proposed so far:

- I. Electron Transfer Mechanism
- II. Ion-transfer Mechanism
- III. Material Transfer Mechanism

A brief discussion on the above-mentioned mechanisms have been presented below:

I. Electron Transfer Mechanism

It has been inferred by Lowell J et. al that the charge generation because of contact electrification between polymer-metal is almost up to the same extent as for polymer-polymer mutual contact electrification [117]. However, it is important to notice that in order to obtain a charge transfer occurrence, two polymeric materials are needed- one will have acceptor state, while the other one will hold donor state. When these two asymmetric dielectric polymers are in mutual contact, empty electron states on the acceptor surface will only be filled by the full electron states on the donor surface [117,118]. The mutual contact literally creates strain on the bulk polymers, which also excite the energy state of the surface of these insulator polymers. These result in inducing free electrons, which can participate in electrification process. Liu C et. al further explained this charge transfer mechanism between insulators using electrochemical approach [119].

II. Ion Transfer Mechanism

Ion-transfer mechanism was first introduced by Whitesides and Diaz et. al. by including ionic compounds in pristine dielectric polymer matrix [119–121]. Very recently, our current research group has published two works using ion-transfer mechanism approach- using BNO-SPI and PTFE as triboelectric surfaces [122]; and triboelectrification between wCF-PANIES and PVDF contact surfaces [6]. In both cases one of the two contact surfaces were functionalized to make this mechanistic process to happen. However, various studies suggested that this mechanism can happen during triboelectrification of two insulating polymers [114,115,123]. In the open environment, moisture particles can accumulate on the contact surfaces and the presence of polar hydronium (H^+) and Hydroxide (OH^-) can induce charge transfer [124] by forming water-bridge. On the other hand, this charge transfer also has been observed to happen in vacuum medium in the absence of moisture contents, which indicates that other charge transfer mechanisms can be involved here [116,123]

III. Material Transfer Mechanism

Compositional analysis of surface has recently investigated that material transfer can occur from one surface to another upon contact and separation of two alike surfaces [125]. These materials transfer may happen in the form of molecular transport between the insulating materials. These molecules usually contain charges based on the polarity of mother material and thus, both positive and negative charges can be realized to present in both surfaces [125,126]. X-ray photoelectron spectroscopy (XPS) analysis has found the existence of these mutually transferred localized charged particles named as “mosaic surface charge”. Therefore, mass transfer is such a phenomenon that cannot be avoided and this scenario should be considered while modeling the contact charging as its presence has already been proved [125].

The above-mentioned three charge transfer mechanisms have been confirmed by several reports published so far. Depending on the property of materials, variance in- contact mechanisms, contact surface area and contact force- may come up with some divergence [116] and it's quite possible to observe simultaneous occurrence of these three mechanisms at the same time.

2.3 Working Modes and Mechanism of Triboelectric Nanogenerator

Triboelectric nanogenerator (TENG) principally works on four modes of contact electrification: vertical contact separation mode, in-plane/lateral sliding mode, single electrode mode and free-standing layer mode. Each of these modes represents different interaction phenomena between two contact surfaces and also concerns on various structure types that can be utilized to generate triboelectrification from several kinetic phenomena.

a) Vertical Contact Separation Mode

TENG has been first introduced with this working mode. Since the operation is based on contact and separation mode, thus a compact design with two surfaces separated by a certain distance is needed to put it in operation. Each surface should be contained with two different type of triboelectric layers with an attached electrode for charge transfer underneath. These two layers should continuous contact each other to generate static charges at the interface and also separate, following the contact, to induce potential difference. Electron transfer between the electrodes occur subsequently to neutralize the emerged potential difference. Therefore, electrical energy can be obtained at the external circuit which can be stored and power up the smart devices. Typical kinetic motions like walking [28,30,31,47], finger tapping [127] or vibrations from engine [128] can be utilized to excite this working mode.

The basic working principle of vertical contact separation mode TENG is based on the coupling of contact electrification and electrostatic induction [109]. **Fig. 1** illustrates the complete depiction

of power generation based on this working mode. At the initial state, there is no charge at the contact surfaces (**Fig. 1(a-I)**) and hence no output can be gained. When some external application of force is provided, the two polymers (polymethyl methacrylate (PMMA) & Kapton) comes in contact with each other. This mutual contact can give rise to static charges due to triboelectric effect [116,129,130]. Since the triboelectric series has been made based on electron receiving or donating affinity of materials, it can be noticed that PMMA lose electrons and became positive, whereas the lost electrons injected in Kapton surface and became negative. Due to the insulating properties of these both polymers charge remained on the surfaces for longer time. As long as they are in contact with each other, no potential difference can be induced between the electrodes (**Fig. 1(a-II)**).

As the applied force is released then these two polymers would tend to separate from each other, and the surface static charges would remain on the surface (**Fig. 1(a-III)**). As the two separated surfaces are oppositely charged, mutual separation from each other gave rise to higher potential difference. As much as the distance between these surfaces grows higher, the open circuit voltage (V_{OC}) keeps increasing. The increase reaches to the maximum value, when moving surface gets back to its original position (**Fig. 1(a-V)**).

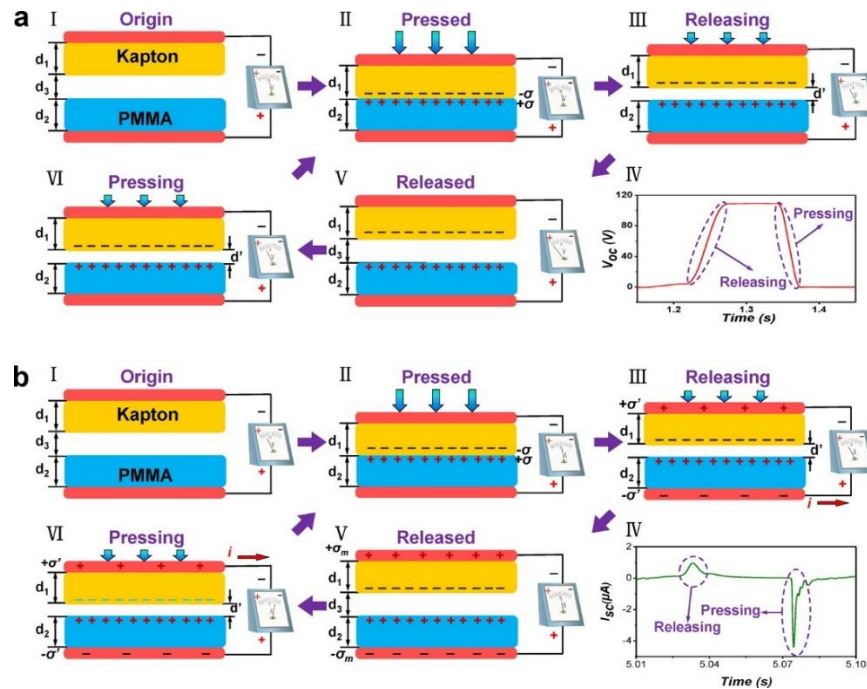


Fig. 1 Fundamental working principle of Vertical Contact Separation Mode TENG (a) Open-circuit condition (b) Short-Circuit Condition

If the two electrodes of attached with top and bottom polymer surfaces are made short, then induced higher potential difference will be neutralized by the flow of electron from top to bottom electrode (**Fig. 1(b-III)**), known as positive current. Again, if immediate contact is followed after separation then there will be created interfacial balanced charge region as much as two contact surface come closer. This left the top electrode with higher electrical potential than the bottom one, which consequently causes a flow of electron from bottom of electrode to the top electrode. The obtained current from such electron transfer in outer circuit is termed as negative current (**Fig. 1(b-VI)**)

The working principle of vertical contact separation mode TENG aligns with the mechanism of electrostatic energy harvester. Only the charge is being generated by the contact electrification

mechanism instead of power supply from outside resources. A general theoretical model has been developed and proposed by Niu et. al in 2013 [131]. According to the model (**Fig. 2**), the open circuit voltage (V_{oc}) and short-circuit current (I_{sc}) can be given by the following equations:

$$V_{oc} = \frac{\sigma x(t)}{\epsilon_0}$$

$$I_{sc} = \frac{S \sigma d_0 v(t)}{(d_0 + x(t))^2}$$

Here, σ = surface charge density of two individual surfaces; $x(t)$ = vertical distance between two triboelectric surfaces; ϵ_0 = dielectric permittivity of air; S = surface area of two contact layers; $v(t)$ = relative velocity between the surfaces; d_0 = effective thickness constant, which can be further mentioned as, $d_0 = \frac{d_1}{\epsilon_{r1}} + \frac{d_2}{\epsilon_{r2}}$, where, d_1, d_2 are the thicknesses of dielectric layer 1 and dielectric layer 2 respectively. In addition, ϵ_{r1} and ϵ_{r2} are the relative dielectric constants of tribo-layer 1&2 respectively.

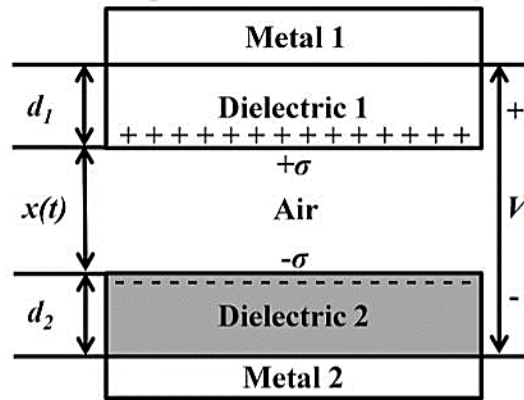


Fig. 2: Theoretical model for dielectric to dielectric vertical contact separation mode TENG

b) In-plane Sliding Mode

This contact electrification mechanism is primarily based on the relative motion between two triboelectric layers. **Fig. 3** depicts the schematics of in-plane sliding mechanism. When two

dielectric surfaces are in contact, there will be appeared static surface charges. These charges will be in neutral state as long as two surfaces persist their mutual contact, as seen in **Fig. 3(a)**. At this stage, no output can be observed. When the upper surface is moved outwards along with the attached electrode, potential difference emerges and electron flow will occur from top electrode to bottom electrode in case of these electrodes are connected with each other, shown in **Fig. 3(b)**. The flow of electrons will be happening until these surfaces are separated completely (**Fig. 3(c)**). On the other hand, when the triboelectric layer 1 slides inwards relative to the triboelectric layer 2, as indicated in **Fig. 3(d)**, then an electron flow can also be realized, which will be in the opposite direction of earlier mentioned moving out process.

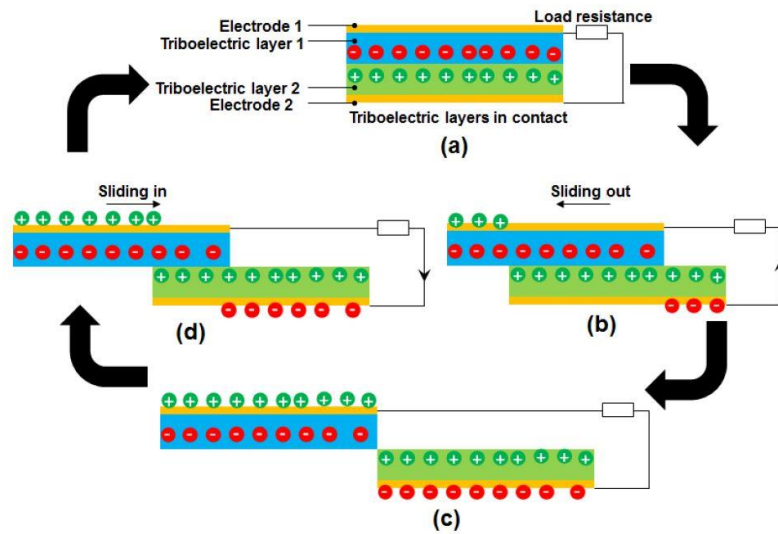


Fig. 3. Schematics of in-plane sliding mode- TENG

Niu et al. has proposed the theoretical model for in-plane sliding mode of TENGs [21]. The V_{oc} and I_{sc} have been given by the following equations in this developed model-

$$V_{oc} = \frac{\sigma x}{\epsilon_0(l-x)} \left(\frac{d_1}{\epsilon_{r1}} + \frac{d_2}{\epsilon_{r2}} \right)$$

$$I_{sc} = \sigma w v(t)$$

V_{oc} = Open-circuit voltage; I_{sc} = Short-circuit current; σ = surface charge density; x = separation distance between the triboelectric layers; l = length of tribo-layers; ϵ_0 = dielectric constant of air; d_1 and d_2 are the thicknesses of triboelectric layer 1&2 respectively; ϵ_{r1} & ϵ_{r2} are the relative dielectric constants of these as mentioned tribo-layers; w = width in in-plane direction perpendicular to the motion sliding direction; and $v(t)$ = relative velocity of triboelectric layers.

c) Single Electrode Mode

This mode based TENG has been introduced due to its simpler, more practical and feasible design for harvesting energy from real life kinetic motion. For the previous two modes of TENG devices, two moving surfaces were required along with an attached electrode with both of them. These electrodes were supposed to be connected with each other via a conductive wire. Such device structures mostly restrict their application to harvest energy from arbitrary environment or freely moving object over them as they require the both touching surfaces to be mutually connected [110]. This single-electrode mode has been proposed to solve this inconvenience.

The basic working principle has been explained through **Fig. 4 (a)**, where the two tribo-layers are polytetrafluoroethylene (PTFE) and Aluminum (Al) respectively. The PTFE can move forward and backward along the Al surface, whereas Al electrode is kept fixed and is also connected to ground with a conductive wire. When PTFE is pushed to move forward or backward, the friction between them would induce to transfer charges between them and in this case PTFE will be negative charges and Al will be charged positively [14]. When the PTFE slides out relative to the

fixed Al surface, then a charge imbalance will be evolved in Al surface and electrons from ground will flow towards the Al to compensate the incongruity. The obtained current due to this electron flow is positive. Similar to in-plane sliding mode, the charge transfer will be continued until complete separation between two surfaces, which will create an equilibrium state at which no output is observed. On the other hand, when the PTFE is reverted to slide in, electrons in Al will flow from itself to the ground in order to gain positive charges. Therefore, current output can be observed in the output circuit, which can be termed as Negative current. This negative current should be obtained until these two sliding surfaces come back into their overlapping position.

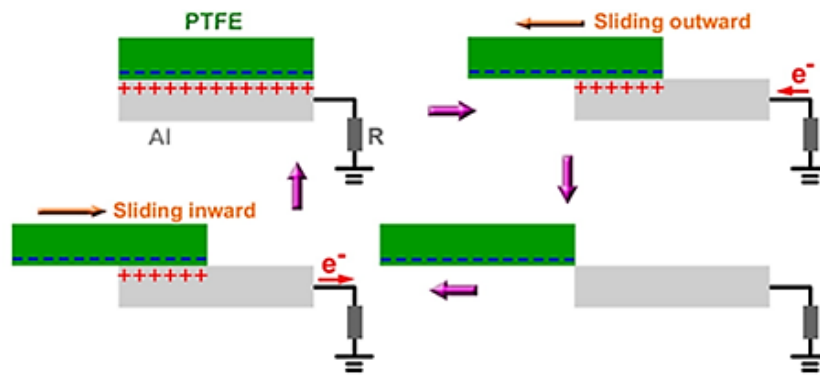


Fig. 4 (a): Schematics of Single-electrode Mode TENG based on in-plane sliding

Single electrode mode TENG can also operate in vertical contact separation mode as depicted in **Fig. 4 (b)**. Here, Fluorinated ethylene propylene (FEP) is one of the tribo-layers which is allowed to have free movement and is also triboelectrically negative in nature. On the other hand, Al is the triboelectrically positive surface, which is fixed and connected to the ground (Cu electrode) through a lead wire. When the FEP is brought into contact with Al, then the surface charge transfer from Al to FEP would cause static negative charge on FEP and static positive charge on Al. Due to insulating properties of FEP, charge will be sustained at its surface for longer time. Therefore, when the FEP is separated from Al, open circuit voltage appears, and this value continue increasing

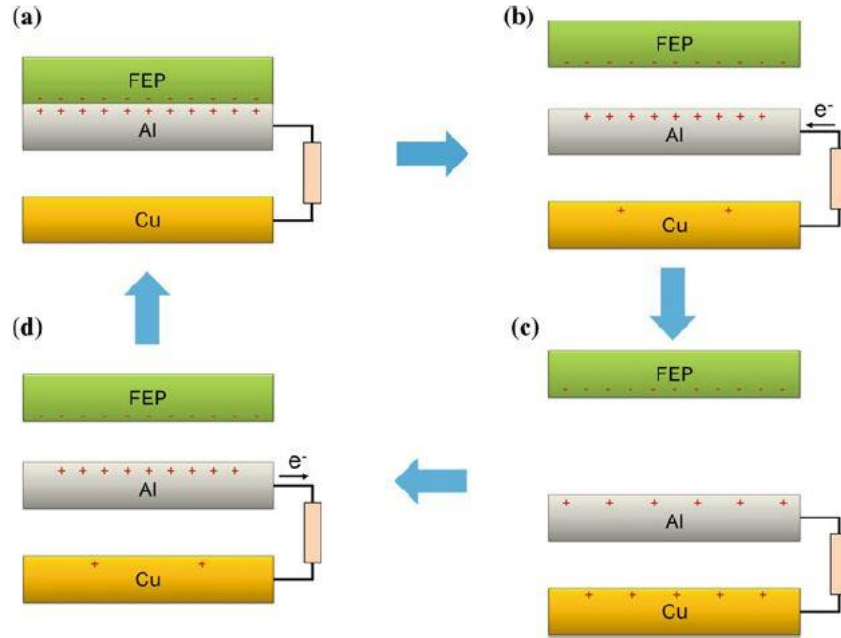


Fig. 4(b): Schematics of Single-electrode Mode TENG on vertical contact separation

until the FEP surface reaches to its maximum position. At the maximum separation height, V_{OC} will be highest. If Al and the ground are shorted via a conductive wire, then electron will flow from Cu electrode to Al in order to neutralize the imbalance, which results in an instantaneous positive current generation. However, if the FEP layer is reverted back closer to Al, then Al will be obtaining a lower electric potential than the ground electrode (Cu). This make the electron flow occur from Al to Cu and thus instantaneous negative current is observed. This current will continuously be generated as long as the FEP and Al comes in full contact again.

A theoretical investigation has been presented by Niu et al. in 2014 for single electrode mode-based triboelectric nanogenerators [132]. According to conductor-to-dielectric and dielectric-to-dielectric contact separation- single electrode mode TENGs (presented in **Fig. 5**), the open circuit voltage can be given by the following equation:

$$V_{oc} = \frac{\sigma w l C_2}{C_1 C_2 + C_2 C_3 + C_3 C_1}$$

Where, l = length of triboelectric layer (both conductor and dielectric surface); w = width of each layer; C_1 & C_3 = capacitance of capacitors connected in series between node 1 and 3 and C_2 = capacitance of capacitor connected with node 1

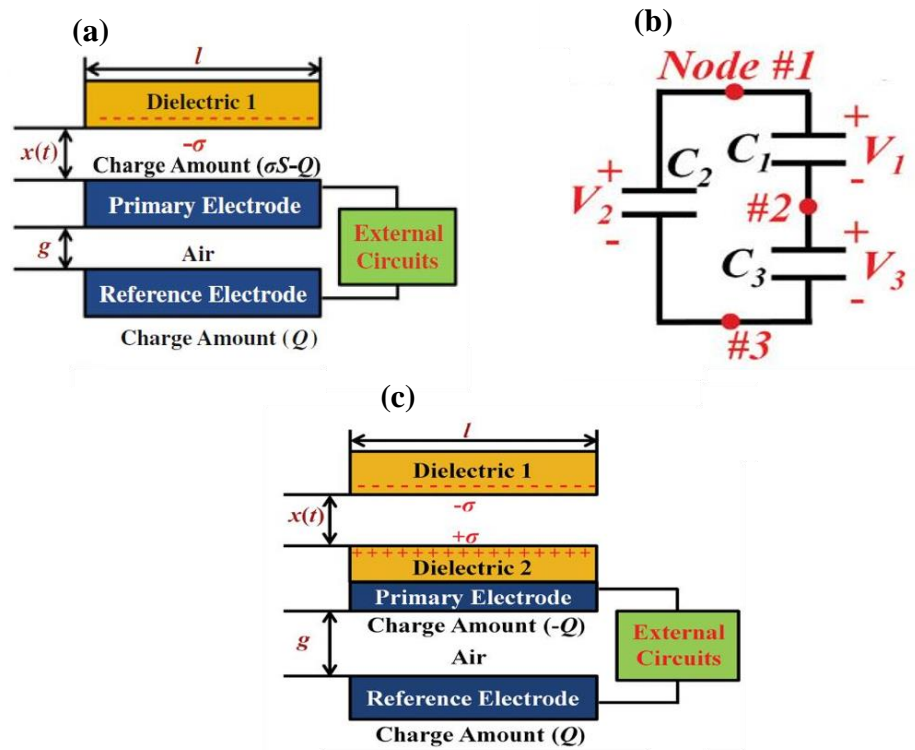


Fig. 5: Theoretical model for (a) dielectric-conductor contact separation-based SEM TENG, (b) Equivalent circuit of 3 capacitors for SEM TENG under open-circuit, (c) dielectric-dielectric contact separation-based SEM TENG.

d) Freestanding Layer Mode

In this working mode of TENG, transfer of charge occurs because of relative motion of a formerly charged tribo-layer and a conductive electrode [110]. When a kinetic motion comes nearby and

goes further away after sliding, then the resulted potential difference between the electrodes cause the electrons to flow from one electrode to other. Physical interaction is not mandatory for this mode. Since the triboelectric layer should be pre-charged, then it's better to use this mode of operation after going through one of the above functional modes or using charged triboelectric layers by the use of corona treatment, ion injection, plasma treatment etc. After charging it by the means necessary, this charged layer can be used then for the current mode.

Before proceeding to the working principle let's take a look at a typical device structure for this working mode of TENG. **Fig. 5(a)** demonstrates a structural design of a freestanding layer-based TENG device, where FEP is the free moving surface and two aluminum electrodes of uniform size are placed on acrylic sheet (substrate). When the FEP slides over the Al surfaces, the resultant triboelectric phenomenon makes FEP to be charged negatively, whereas Al will be charged positively. There are two phenomena for this working mode of TENG: i) when the moving dielectric surface and fixed electrodes are not charged; and ii) when the dielectric surface is already charged.

The first scenario is mostly identical with the SEM-based TENG. The only difference in this case is the charge transfer will be between the electrodes attached beneath the moving dielectric surface. When FEP is quietly overlapped on the left electrode of **Fig. 5(b-i)**, then injection of electron from Al surface to FEP surface makes generates negative static charges on FEP and positive charges on Al. When the FEP slides towards the right electrode, **Fig. 5(b-ii)**, then the positive charges from the left electrode will flow towards the right electrode to screen the negative charges of FEP surface.

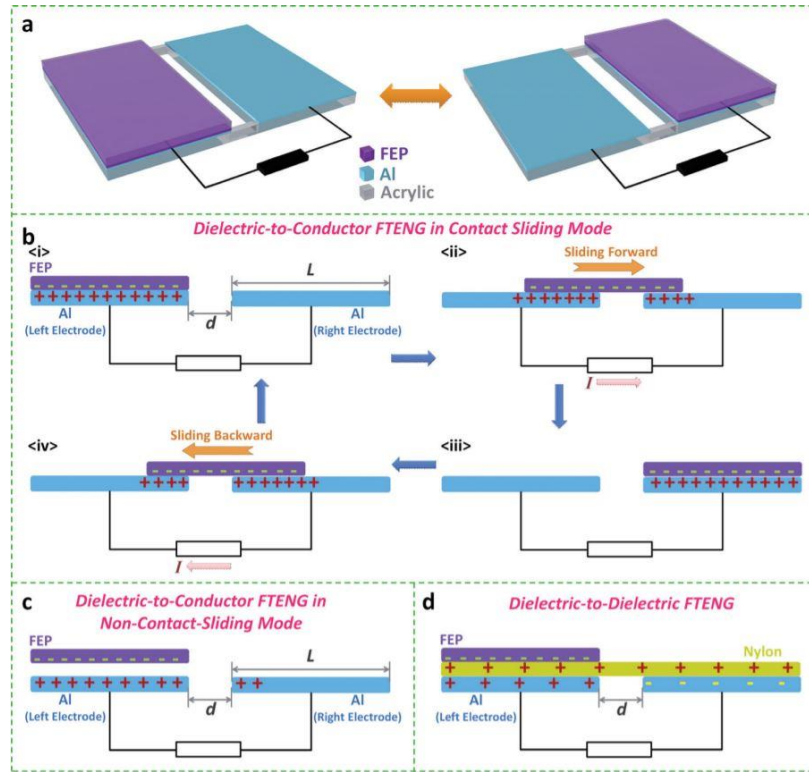


Fig. 6: Free-standing layer (a) device structure; (b) contact sliding mode between dielectric-to-conductor; (c) non-contact sliding mode between dielectric-to-conductor; and (d) contact sliding mode between dielectric-to-dielectric [27]

Until FEP film becomes completely overlapped on the right electrode, the flow of positive charge happens intermittently. There will be no flow of charge when they are in equilibrium position, as shown in **Fig. 5 (b-iii)**. The positive flow of charge will be happening in the reverse direction as soon as the FEP film starts to slide towards the left electrode (**Fig. 5(b-iv)**).

The second scenario is considered when the surface of FEP polymer is already charged negatively. Due to higher insulating properties, these charges remain on the surface for quite a longer time. If these pre-charged FEP approaches towards the Al, then without contacting the electrodes it is able to make charge flow between them with just swaying it from above (**Fig. 5(c)**). There is another design concept for free-standing layer mode of TENG. **Fig. 5(d)** shows the device configuration,

where between FEP and stationary Al array of electrodes, there another layer of nylon. Since both nylon and FEP are dielectric insulators and upon contact electrification FEP becomes negative and nylon will gain positive charges. These charges will be persistent on those surfaces because of their insulating properties. Therefore, nylon's potential will be constant on Al electrodes and also its unable to drive charges among these electrodes. Hence, only FEP movement can make the charge transfer happen. For this reason, this device principle is also same as the previous one.

2.4 State-of-art Overview of Devices Structures based on purpose of applications

In 2012, for the first time Fan et. al reported about the triboelectric generators (TEGs) as a potential power generator for running self-powered devices [109]. They also proposed a mechanism of triboelectrification through proper schematics, which has been shown in **Fig. 6**. In that work, they have come up with a sandwich-like device structure stacked by Polyester (PET) and Kapton film. A layer Au electrode was sputtered on both thin films and certain separation distance was maintained to function the device based on contact-separation concept. This phenomenon was excited by press-release scenario. The maximum output voltage was 6V (pk-pk) and current was 1.2 μ A (pk-pk). They also showed that the novel proposed triboelectric device operation can light a LED light. This work predicted a great potential for using this device a pressure or strain sensor.

Following this work, in the same year, the researchers have fabricated a TENG device as represented in **Fig. 7**, which includes material modification technique and outputs were quite higher [7]. The device structure was same as before, but this time they focused on increasing mutual contact area while the two tribo-layers come in contact. A thin, transparent, patterned-PDMS was used as negative tribo-surface, whereas PET was kept as tribo-positive one. They used three patterns-line, cubic, pyramid-shaped to induce high surface roughness. The output was found

greatest, voltage 34 V and current 1 μ A, for pyramid-shaped micro-structures. It was realized that the shape of pyramid structures overall increased the contact surface area than the other structures. Since device demonstrated in this research was regarded as self-powered sensor, it does not require any external power supply to support its operation.

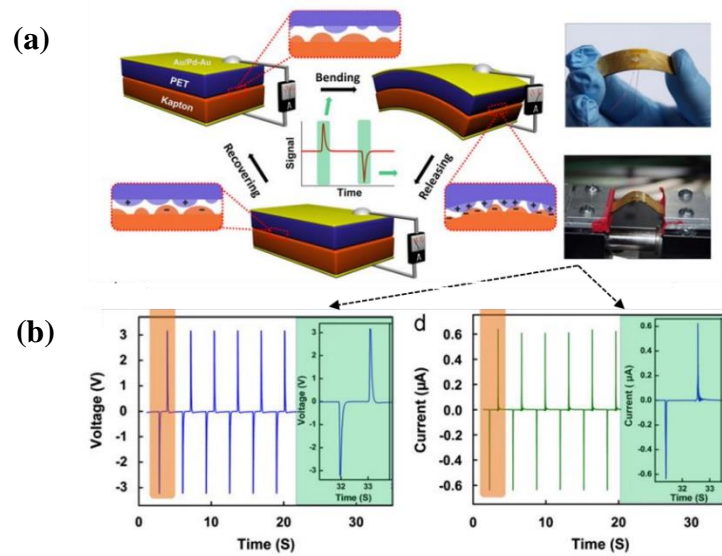


Fig 7: (a) schematic illustration of working mechanism and real-time photographs of TEG working upon bending and releasing process, (b) Electrical Outputs of the as fabricated TEG device

2.4.1 TENG-based on Biokinetic Energy Harvesting

This is the most ubiquitous form of energy in our surroundings which can be harvested to power several electronic devices like sensors, wrist watches, calculators or smartphones. Several works have been reported so far to harvest biomechanical energy. Hou. et al proposed a very simple mechanism to harvest energy from human walking [133] at the very beginning of TENG device evolution. **Fig. 9 (a, b)** demonstrates the schematics and real-time device structure. They have used

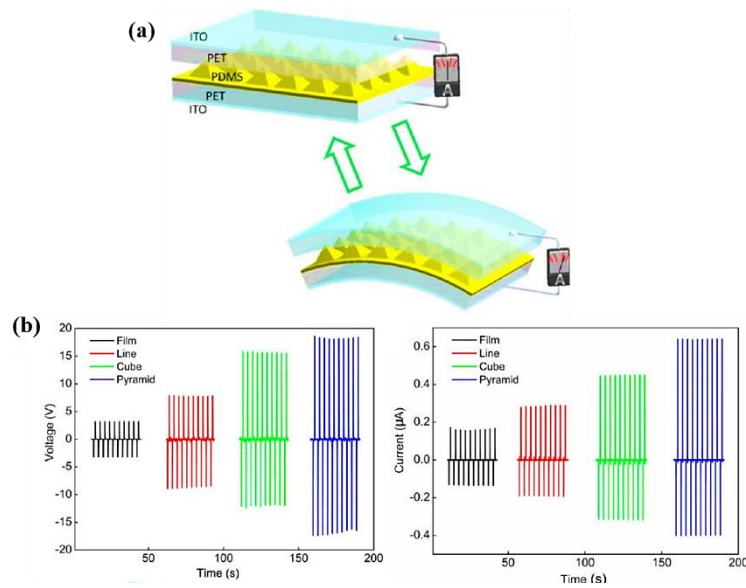


Fig. 8: (a) schematics of TENG structure, and (b) electrical outputs representation.

A thin PDMS polymer film- which was patterned with dome-shaped bump on its surface-was used as bottom electrode and polyethylene terephthalate (PET) was used as the top electrode. A spacer of soft foam was put as a spacer between these two electrodes. Several number and thickness of spacers were used to optimize the performance of TENG device. It was concluded that the output performance resulted highest in case of least of spacers. Finally, the device was put inside a shoe insole (**Fig. 9(c)**) to test practical feasibility. It was observed that while stepping up shoe insole and stepping down from shoe insole were maintained continuously, then the output power was high enough to light 30 LED lights, shown in **Fig. 9(d)**. The output voltage from this TENG device was 220 V and Output current was realized 40 μ A respectively. This output indicates that if several alike TENG devices are connected together, large scale of energy can be produced for powering far bigger utility instruments.

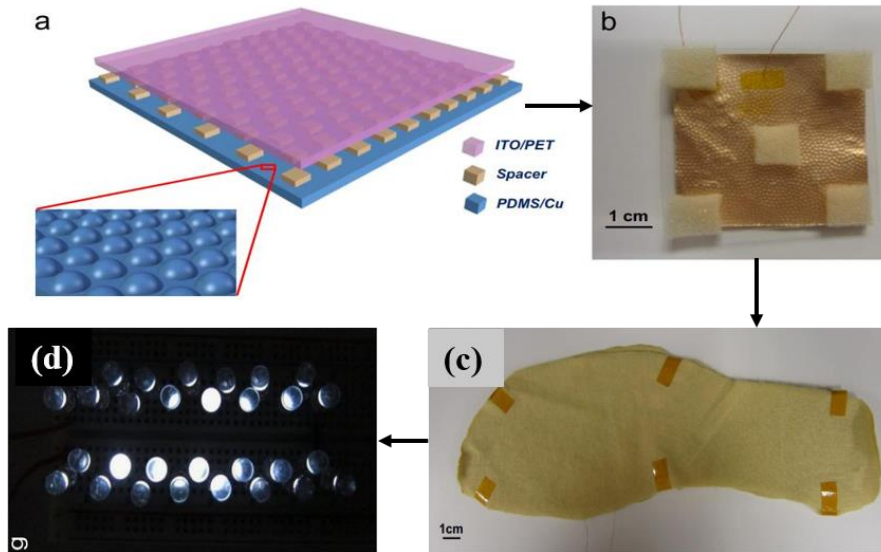


Fig. 9: (a,b) Schematics and real-time device structure; (c) TENG device placement in shoe insole; and (d) 30 white LED light lighting during device operation upon stepping up onto and stepping down from shoe insole

Most of the triboelectric energy harvesting devices reported were based on comparatively mass mechanical movements like running, walking or movement of hands etc. The harvested energy was then utilized for powering the earlier-mentioned devices. However, sometimes this mass resource of mechanical motion is not obtainable and, in such case, harvesting energy from slight movements of body parts is desired. Therefore, technological advancements have been made further to address this concern as well. Researchers have proposed a lightweight and arc-shaped TENG device, presented in **Fig. 10**, where carbon sponge was used as an electrode and a substrate. Due to the use of carbon sponge, the whole device weighted only 0.0992 gm. Nylon was used as the positive surface after triboelectrification. On the other hand, nanowire-grown polyvinylidene fluoride (PVDF)/PET/Polyimide (PI) was used as the negative friction layer. This device was used as an accelerator sensor, where single finger tap can generate power enough to light 20 LEDs.

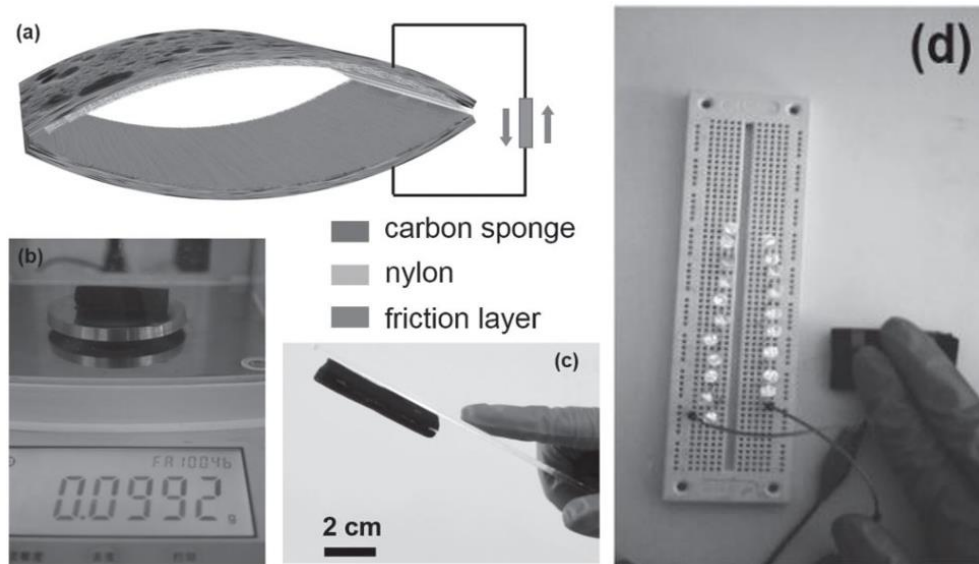


Fig. 10: (a) Schematics TENG device; (b) measured weight of TENG device; (c) optical image of the prepared TENG; and (d) lighting of 20 LED lights powered by finger tapping

2.4.2 TENG-based on Wind Energy Harvesting

The most alternative resource to the fossil fuel crisis in upcoming time is the renewable energy. Harvesting this omnipresent energy smartly can meet up the energy needs of the whole human kind. Wind energy is such a renewable energy that is always available in everywhere. Wind turbine or windmill have already been in use but some drawback like installation place, high installation expenditure, low outputs etc. hinder its use to be as an efficient energy harvesting structure. TENG has come up with a boon as a solution to this problem as it can convert a tiny kinetic movement in to useful electrical energy. Furthermore, several benefits such as less fabrication cost, less installation space, mobility, higher sensitivity to kinetic displacement make it a suitable choice for harvesting wind power.

Various research groups all around the world have already evaluated the potential of TENG devices operated by wind energy. For instance, Cui et. al. have proposed a TENG structure that was able to show higher output power being driven by a meagre mouth blow [134]. They have prepared a device, shown in **Fig. 11**, where a double-layered polyaniline (PANI) film with enhanced nanofibers on both sides of a reference Kapton film was placed at the middle of the structure; and two thin PVDF films were attached with bottom and top acrylic surface plates. They have reported that if a wind blow of 15 m/s speed was passed through the device then the resultant contact separation between the PANI NFs and PVDF would result in 190 μA short-circuit current with maximum peak $\sim 248 \mu\text{A}$, and average open circuit voltage of 280 V with maximum peak voltage $\sim 375 \text{ V}$. They have also shown that 1240 red LEDs can be lit if the wind velocity is too high. In addition, the TENG device provides cathodic protection against corrosion in sea environment.

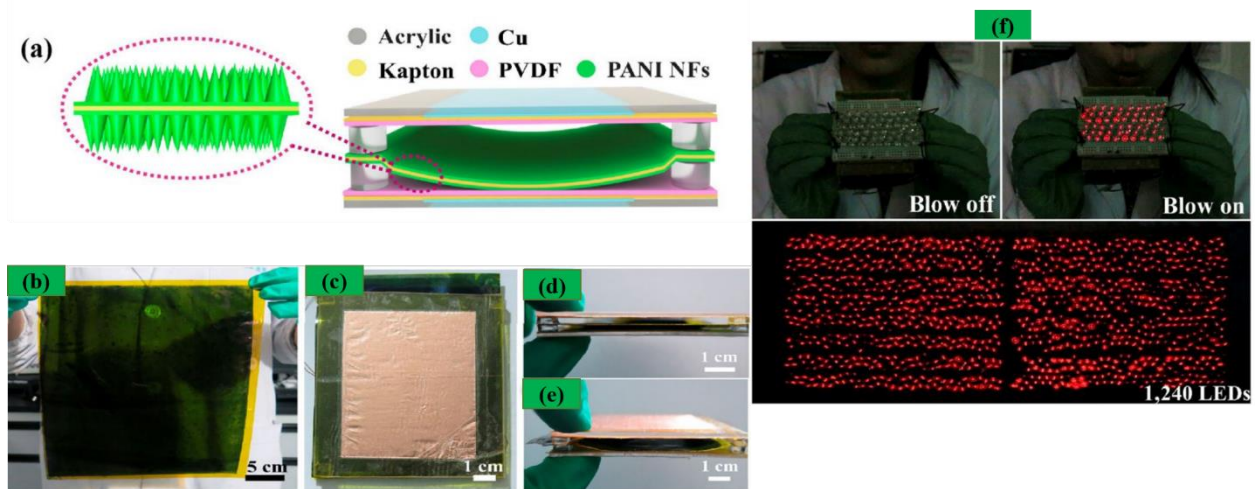


Fig. 11: (a) Schematics of TENG device; (b) PANI NFs grown on Kapton film; (c) Top view of the TENG structure; (d, e) side view of fabricated device; and (f) lighting of 58 LEDs when mouth blown air is used and 1240 LEDs were lit up when 15 m/s wind speed was passed through.

Moreover, Xie et al. have demonstrated a wind-cup structure [135], **Fig. 12(a,b)**, where the wind energy was converted into rotation energy. The rotation energy then provided the kinetic force to produce contact electrification between nanowire-grown PTFE surface and Al layers. 62.5 mW power was generated at maximum, when the wind energy was provided at a velocity of 15 m/s.

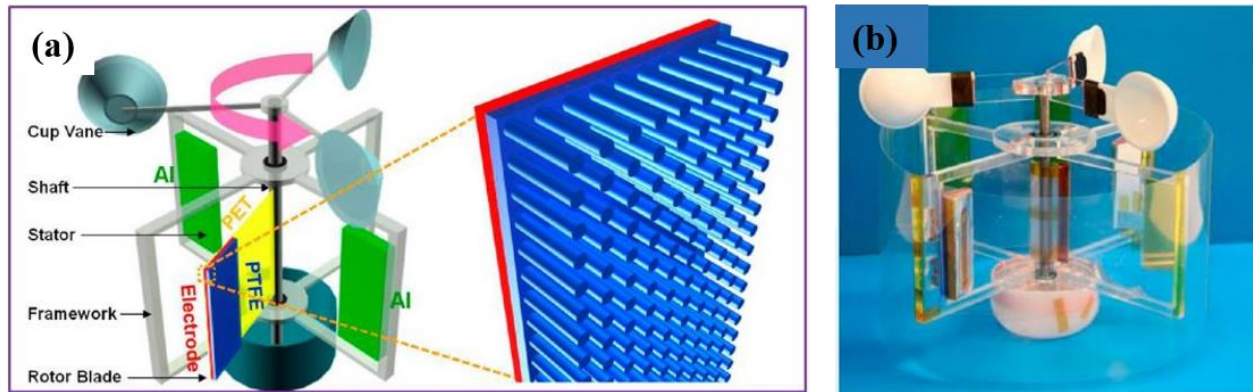


Fig. 12: (a) wind-cup device schematics; and (b) Real-time setup

In addition, A rotating TENG device, **Fig. 13**, has been reported by research group of Professor ZL Wang in 2014 [136]. The device worked on sliding based triboelectrification and it consisted of a rotor, which is made of Copper (Cu) and worked as one of tribo-surfaces, and a stator, which is made of micro-patterned electrode embedded under a FEP film. The as fabricated device generated power output of 1.5 W and is able to harvest energy from wind and water flow.

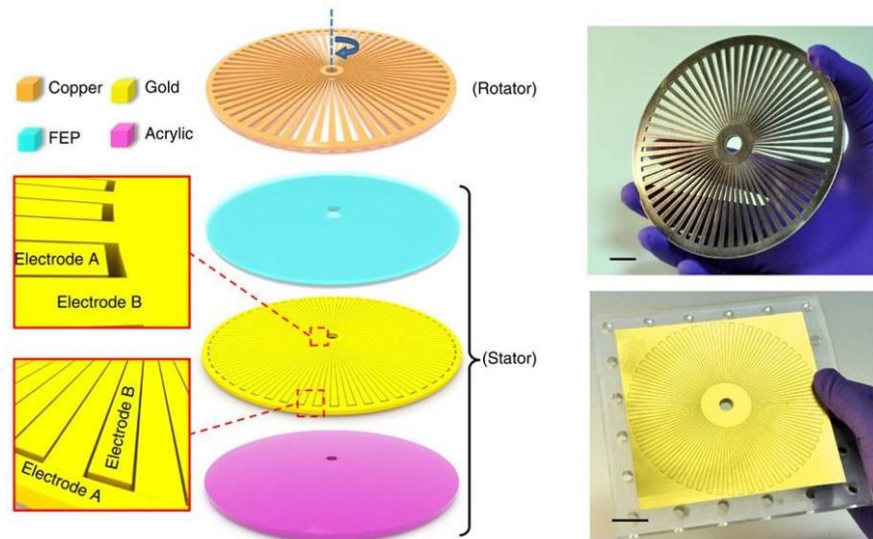


Fig. 13: Rotating TENG structure using micro-patterned electrode

2.4.3 TENG-based on Liquid Energy Harvesting

The TENG devices proposed earlier after its invention were primarily based on solid-solid contact based triboelectrification. These devices have a very common disadvantages like rapture of the surface due to long-term use or its vulnerability to humidity in open environment etc. These can gradually reduce the overall performance of the devices over time. Furthermore, the fabrication of TENGs for liquid energy harvesting is quite simpler unless the plan is for harvesting energy from huge water sources like lake, canal or sea etc. Most of the direct water-solid surface contact based TENG devices work on SEM or free-standing layer mode. However, several TENG devices have been reported recently that uses the wave energy of water to make solid-solid contact-separation phenomena for generating triboelectric power. There are two types of liquid energy harvesting works have been done so far-

- i. Wave energy harvesting

ii. Droplet-based energy harvesting

Since the current thesis is based on droplet-based triboelectric energy harvesting scenario, thus we will discuss it in detail after introducing wave energy harvesting in brief.

Professor ZL Wang and his research group first proposed their concept to harvest energy from water from vertical contact-separation method in 2013 [48]. Their as delineated device schematics and working mechanism have been presented in **Fig. 14**, where they used a water as one of the triboelectric layers kept inside a water tank with Cu thin film electrode attached in it. Another triboelectric layer was PDMS tribo-negative polymer, which surface was patterned with pyramid-shaped microstructures. These microstructures acted as regular gaps between the contact surfaces as well as increase of interfacial contact area between two surfaces. Moreover, due to rough surface topography the hydrophobicity was significantly increased, which helped the surface to get of addition water particles attached to it after separation process. If the insight in working mechanism is considered, then it can be realized that during mutual contact PDMS is negatively charged and the water is charged positively. The flow of current in the external load will be realized will be observed throughout the whole contact-separation phenomenon, as described earlier in the “working modes” part of this very chapter. This water-energy harvester TENG device produced almost 90 V and 2 mA m^{-2} current density, which would light up 60 commercial green LED lights. Moreover, this device also was also tested with deionized (DI) water and sodium chloride solution. Finally, it has been observed that the deionized water performed as an efficient contact surface than tap and NaCl solution. The reason behind this was the attachment of positive ions on negative PDMS surface and screening of negative charges on PDMS surface layer.

Afterwards several solid surface-water contact electrification reports have been proposed. The most pivotal works are being presented as summary in **Table 2**.

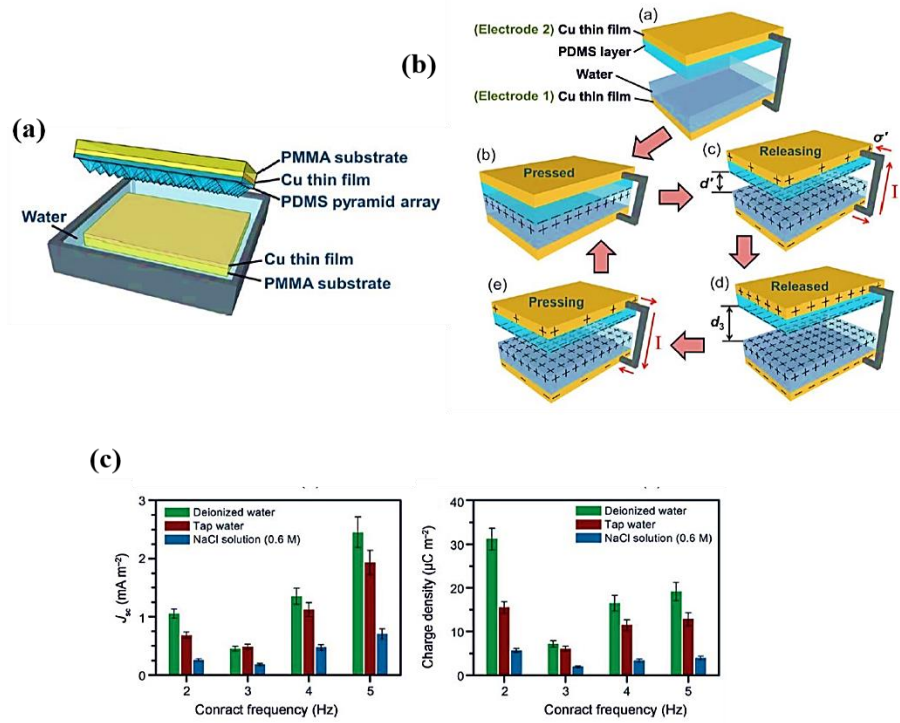
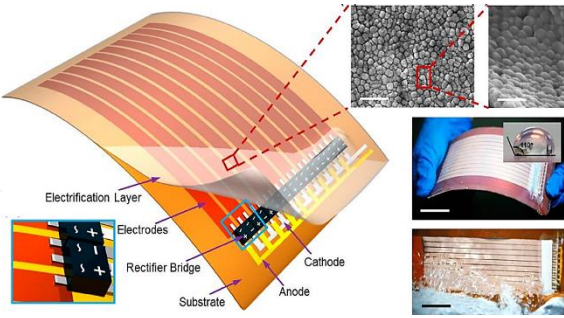
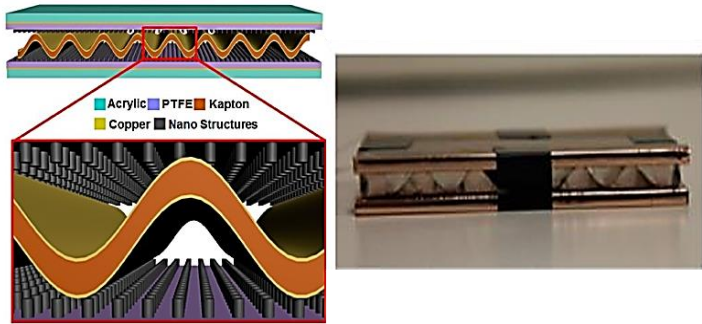
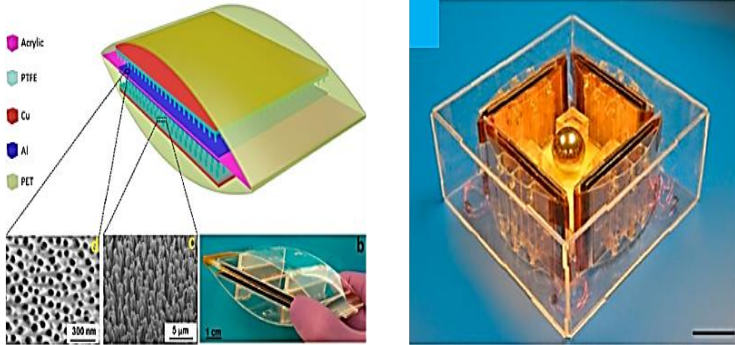


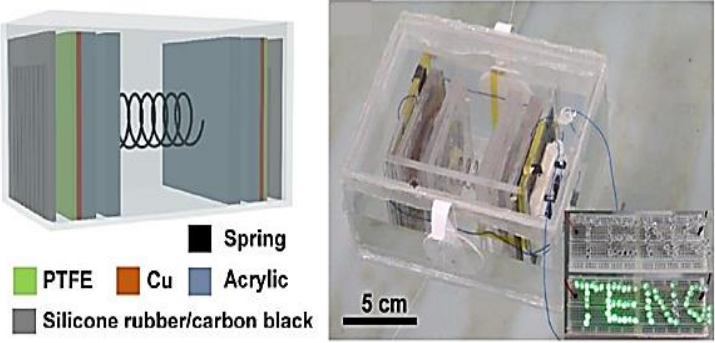
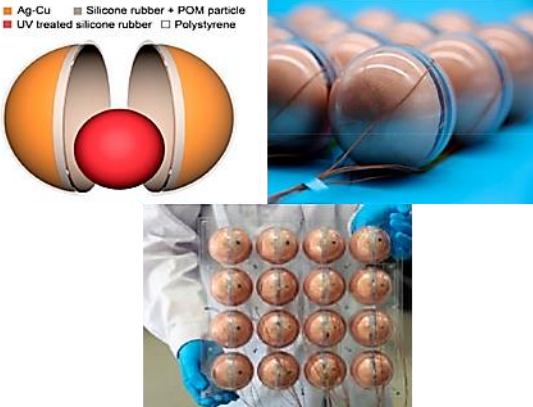
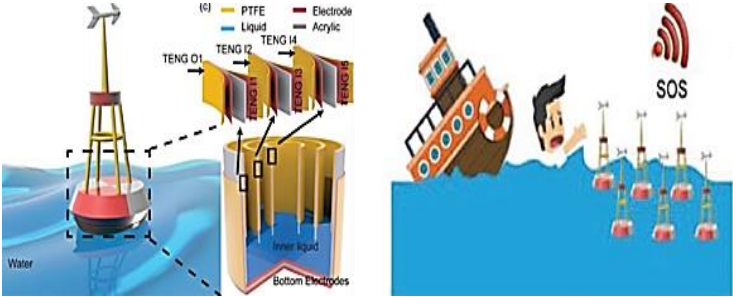
Fig. 14: (a) device structure; (b) working mechanism; and (c) output performances using tap, DI water and NaCl solution

Table 2. State-of-art Works on Solid -water contact triboelectrification

Research Institutes	Summary	Device Structure
Georgia Institute of Technology, USA; Beijing Institute of Nanoenergy & Nanosystems, China. 2014 [38]	<ul style="list-style-type: none"> ➤ Nanowire grown FEP thin film ➤ FEP surface-water wave triboelectric $I_{sc} = \sim 6 \mu A$ ➤ FEP surface-falling water drop triboelectric $I_{sc} = 3 \mu A$ 	

	<ul style="list-style-type: none"> ➤ Hydrophobic surface ➤ Electrical output efficiency 7.7% 	
<p>Georgia Institute of Technology, USA; Beijing Institute of Nanoenergy & Nanosystems, China. 2015 [137]</p>	<ul style="list-style-type: none"> ➤ Nanoparticle incorporated PTFE thin film surface ➤ Bendable solid surface structure ➤ Integration of electrodes were used to boost up the output performance ➤ $V_{oc} \sim 225$ V and $I_{sc} \sim 12$ μA ➤ Hydrophobicity is $\sim 110^\circ$ ➤ Device shows better corrosion protection, pollution reduction, water desalination performance in marine environment 	

<p>Georgia Institute of Technology, USA; Key Laboratory of Advanced Technologies of Materials; Southwest Jiaotong University; Chinese Academy of Sciences, China. 2014 [138]</p>	<ul style="list-style-type: none"> ➤ Wavy-shaped structure has been proposed ➤ Self-restorable design ➤ The device operates based on the impact created by waves ➤ $V_{oc} = 72V$; $I_{sc} = 32 \mu A$, Power = $0.4 W/m^2$ 	
<p>Georgia Institute of Technology, USA; Key Chongqing University, China; Donghua University, China; Chinese Academy of Sciences, China. 2015 [37]</p>	<ul style="list-style-type: none"> ➤ A close packed TENG network has been proposed here ➤ Based on the number of units, outputs can be increased noticeably ➤ 4 units have been showed $I_{sc} = 0.32 mA$ and $V_{oc} = 200 V$ 	
<p>GeorgiaTech, USA; University of Electronic Science and Technology, China; Beijing Institute of Nanoenergy & Nanosystems 2014 [139]</p>	<ul style="list-style-type: none"> ➤ Hybrid TENG comprised of water-solid interfacial interaction TENG and Impact TENG has been shown. ➤ IE TENG and impact showed $5.1 \mu A$ and 4.3 	

	<p>μA current respectively</p> <ul style="list-style-type: none"> ➤ The proposed TENG has been used as a self-powered distress signal application 	
<p>Beijing Institute of Nanoenergy and Nanosystems, China; University of Chinese Academy of Sciences, China; Georgia Tech, USA 2018 [140]</p>	<ul style="list-style-type: none"> ➤ Spring-assisted TENG has been reported based on water-impact excited triboelectrification ➤ Max. output power density was 2.40 Wm^{-3} 	
<p>Georgia Tech USA; University of Chinese Academy of Sciences, China; 2017 [141]</p>	<ul style="list-style-type: none"> ➤ A novel coupling design has been proposed 	
<p>Georgia Tech, USA; Tsinghua University, China; University of Chinese Academy of Sciences, China. 2018 [142]</p>	<ul style="list-style-type: none"> ➤ A buoy-like LS TENG has been shown here to harvest wave energy even of very low frequency ➤ Highest $I_{sc} = 290 \mu\text{A}$; $Q = 16725 \text{ nC}$ and $V_{oc} = 300 \text{ V}$ were obtained 	

	<p>➤ The reported TENG worked as self-powered SOS system</p>	
--	--	--

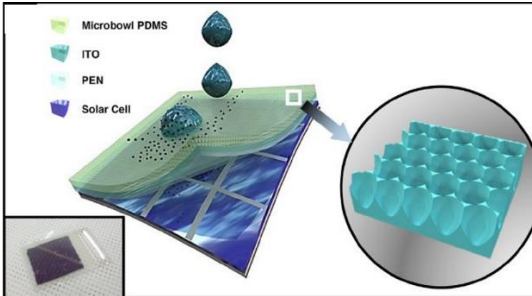
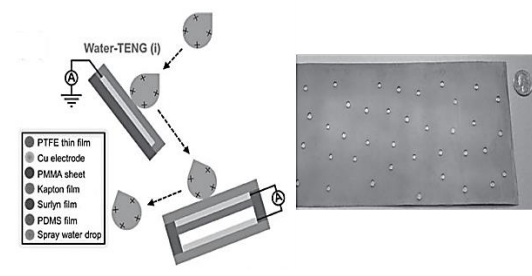
The summarized works mentioned above in tabular form particularly concerned on harvesting energy from higher or low frequency waves. These works showed the grater prospects of harvesting water wave energy by direct interfacial contact electrification or by utilizing the impact force provided by the wave itself. Although there are some drawbacks like complex device design, unavailability of uniform wave force and incongruity of output parameters (higher open circuit voltage and lowest short-circuit current) is still a concern for commercialization of these devices, the effort made so far has come out with tremendous improvement towards the dream “Blue Energy Harvesting”.

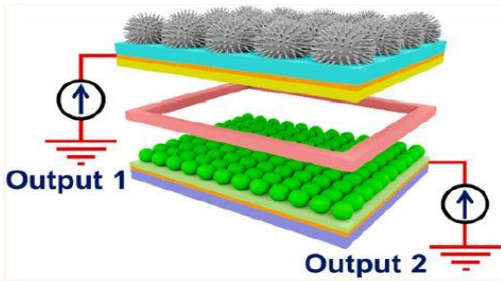
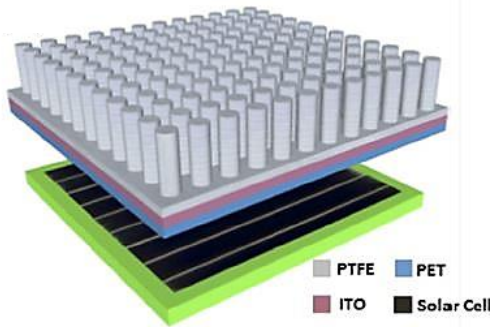
There is another liquid energy that is quite miniscule in size and shape, but has been proved quite convenient to energy harvesting, especially in triboelectric energy harvesting. The name of this liquid substance is “droplet”. Along with the wave energy harvesting, scientists have been persistent so far to harvest triboelectric energy by exploiting the kinetic motion of droplet over a processed material surface. The phenomena of water droplet contact electrification was primarily found by Yatsuzuka et. al in 1993 [143]. They investigated the phenomena basically not to find the triboelectrification concept, but to find a proper solution to the unexpected electrification usually occurred while washing devices with pure water. They performed their experiment with water droplets rolling on PTFE polymer surface and concluded with some pivotal conclusions: sliding electrification will increase when sliding speed of the water droplet is faster and the conductivity of the droplet is lower; surface charge density grows higher with thinner polymer surface; and sliding electrification is also influenced by the force working between the static

charges on the polymer surface and charges in ground metal plate. Based on these decisive statements, the triboelectric phenomenon can be investigated by optimizing several parameters for the aim of energy harvesting. After being discovered in 2012 for the first time, the application of TENG device has been extended to various types of energy harvesting. Energy harvesting from water droplet is not an exception.

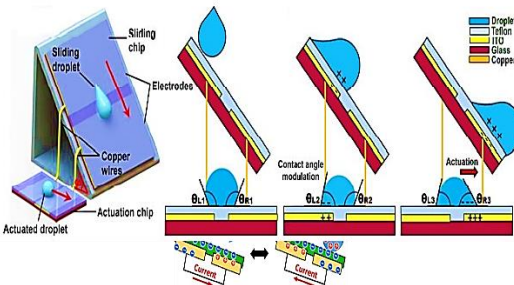
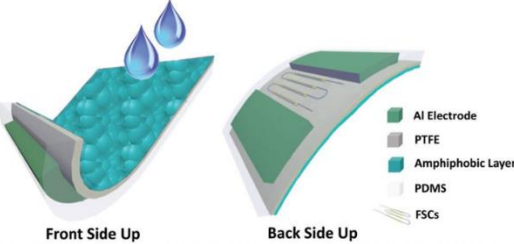
Instead of writing individual progress on this particular energy harvesting, a brief summary is provided below in **Table 3**.

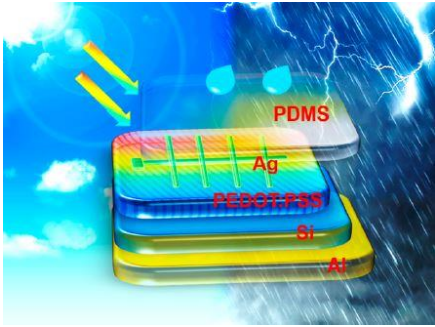
Table 3: Recently reported articles on droplet-solid surface contact based triboelectrification

Research Institutes	Summary	Device Structure
Korea Advanced Institute of Science & Technology (KAIST), South Korea, 2014 [58]	<ul style="list-style-type: none"> ➤ A micro-bowl array structured transparent PDMS surface was prepared as a solid contact surface ➤ Hydrophobicity was 150° ➤ Output $I_{sc}= 128 \text{ nA}$; $V_{oc}= 7\text{V}$; Power= $0.27 \mu\text{W}$ 	
Georgia Tech, USA; Beijing Institute of Nanoenergy & Nanosystems, China; Hennan University, China. [59]	<ul style="list-style-type: none"> ➤ A PTFE surface with hierarchial micro/nano-structures was exposed to dripping and sliding water droplet over it. ➤ Hydrophobicity was 169° ➤ Output generated by 30 μL droplet was 9.3 V (V_{oc}) and $17\mu\text{A}$ (I_{sc}) 	

<p>Georgia Tech, USA; Beijing Institute of Nanoenergy & Nanosystems, China; Hennan University, China. [61]</p>	<ul style="list-style-type: none"> ➤ Hybrid TENG structure has been proposed here (water-solid, solid-solid contacts) ➤ TiO₂ layer was used as solid surface for droplet sliding, PTFE-SiO₂ was used for solid-solid contact. ➤ For 40 mLs⁻¹ water stream flow impact, I_{sc} for output 1 and 2 were 43 μA and 18 μA respectively ➤ Output power was 1.31 Wm⁻² and 0.38 Wm⁻² for output 1&2 respectively 	
<p>Georgia Tech, USA; Shanghai University, China; Chung-Ang University, South Korea; Chinese academy of sciences, China. [144]</p>	<ul style="list-style-type: none"> ➤ A Si-based solar cell and droplet energy harvesting TENG have been integrated ➤ Solar cell generated V_{oc}= 0.43 V and Current density= 4.2 Am⁻²; and TENG produced V_{oc}= 30 V and Current density= 4.2 mA^m⁻². ➤ Hydrophobicity of TENG device surface was measured 169° 	

<p>Bilkent University, Turkey, 2016. [145]</p>	<ul style="list-style-type: none"> ➤ A modified PVDF microtube was prepared and connected with a MEMS device ➤ The test showed with increasing droplet volume; output voltages increased. The increasing Isc rate was quite high ~120 μA for 65 μL 	
<p>PosTECH, South Korea; KITECH, South Korea 2017 [146]</p>	<ul style="list-style-type: none"> ➤ In this work lotus leaf was taken as the contact surface due its default natural hydrophobicity ➤ Thermal nanoprinting was further applied to increase surface roughness 	
<p>SKKU Advanced Institute of Nanotechnology (SAINT), South Korea; Zhejiang University, China. 2016 [62]</p>	<ul style="list-style-type: none"> ➤ A monolayer graphene was synthesized on PTFE polymer film ➤ Pseudo-capacitance between droplet and graphene layer increased the triboelectrification ➤ Obtained power from this triboelectrification was around 1.9 μW 	

<p>Dalian University of Technology, China, 2018 [147]</p>	<ul style="list-style-type: none"> ➤ In this work, utilizing the triboelectric output voltage generated from droplet-polymer contact electrification, droplet actuation has been demonstrated on an actuation chip ➤ This work represents the potential of droplet triboelectrification in electro wetting micro-fluidic devices 	
<p>University of Science & Technology, China. 2018 [148]</p>	<ul style="list-style-type: none"> ➤ A very novel TENG structure has been shown here, which consists of an amphiphobic layer as a triboelectric surface and fiber capacitor structure underneath for the purpose of triboelectric power generation and storage at the same time. ➤ An application of the proposed device has been tested on a rain coat, which shows $V_{oc} = 4V$ by continuous water flow for 100 s 	

<p>Soochow University, China, 2018 [57]</p>	<ul style="list-style-type: none"> ➤ Solar cell and rain drop energy harvesting TENG device have been integrated in one compact structure ➤ A simply imprinted-PDMS transparent film and imprinted-PEDOT: PSS film was synthesized to put together with a common electrode for both devices ➤ The integrated device showed $I_{sc}= 33 \text{ nA}$ and $V_{oc}= 2.14 \text{ V}$ 	
---	--	--

Drawbacks of previous works and Originality of the present work

All the reports presented on droplet-based triboelectric energy harvesting so far from the beginning were and still are monotonously focused on fabrication of superhydrophobic surfaces using sophisticated, cost ineffective and complex experimentation. Although solid-solid contact based TENGs have reported a number of approaches to improve device performance, liquid-droplet based TENGs did not address such variations yet. Therefore, the concern of this thesis is to work on synthesis of such a nanocomposite film- comprised of triboelectric polymer and graphene oxide derivative as a filler- which can optimize the concerned energy harvesting potential by optimizing several parameters of the film itself. The thesis will further demonstrate in the upcoming sections how the pristine/nanocomposite film thickness, filler quantity optimization, filler alignment can simultaneously optimize hydrophobicity, dielectric properties and subsequently output triboelectric performance.

Chapter 3

Experimental Procedures and Material Characterization

3.1 Experimental Procedures

Several experimental steps were followed to synthesize a suitable nanocomposite matrix with our desired properties. Firstly, polymer selection was one of the most crucial steps before approaching to selection of other things. Secondly, filler selection was the following step as depending the choice of this material, properties of the whole polymer composite will be tuned. Finally, hydrophobicity optimization was another important point of consideration for implementing the current work successfully.

As we know already, any organic/inorganic substance can show triboelectric performance. Depending on the usual applications of TENG devices, several material choices are seemingly available e.g. organic-inorganic hydrogels with ceramic fillers provides a novel platform for smart strain sensing application [149], conductive polyaniline can accelerate electron transfer phenomenon while interacting with the surrounding environment [150], porous metal-polymer composites can come with higher surface area and can be applied to gas sensing applications [151] etc. However, hydrophilicity, alike polarity and more conductivity may become a drawback for their potential use in triboelectric applications. Therefore, the triboelectric series provides us with a list of polymers and other materials from where we can make suitable choice depending on the requirement of our work. Since we are working on energy harvesting from water droplet, its quite possible that while the droplet was being generated and passed through air its positively or negatively charged. Since most of the reports have reported so far that the chance of water droplets

to be charged positively is quite higher, we chose to go for selection of tribo-negative polymer in the series. Among the different polymers, we chose PDMS due to its several advantages over other choices. It generates negative static charges when comes in contact with any other triboelectric positive surfaces. Its quite biocompatible as its use is very popular in bioMEMS skin, hair problem solutions and foods. PDMS is very flexible and can be deformed to any desired shapes without strong possibility of damage. Moreover, its transparency has become a blessing for solar energy harvesting along with the triboelectric energy harvesting.

In case of making filler material selection although several fillers like ceramic, metal-nanoparticles, graphene derivatives are available, we chose rGO because of its aforementioned unique structural, electronegativity, presence of functional groups, electron trapping potentiality properties. Although other graphene derivative could be considered, but its simple synthesis, long lasting storage potential without agglomeration in comparison to graphene and carbon nanotubes, and higher capacitance [66,68] can offer unique benefits over other carbon-based fillers. The optimized oxygen containing functional groups also impart it better dispersion, higher electrical conductivity and less adsorption [66,69–71]. These functional groups also possibly may bless this graphene derivative with the utility to create bonding with its host matrix for electrical/mechanical property improvement, whereas graphene/other carbon nanofillers do not have such functional groups in their pristine condition [72]. Moreover, optimized conductivity of rGO mostly avoids the risk of dielectric breakdown, which may happen for highly conductive graphene [73], carbon nanospheres [74], carbon nanotube [75] filler included composites at a very lower percolation threshold. Furthermore, while graphene oxide (GO) has poor conductivity, higher hydrophilicity due to presence of numerous oxygen based functional groups [76–78], rGO has comparatively higher conductivity and hydrophobicity because of the reduction of these functional groups.

Finally, the hydrophobicity of the prepared nanocomposite samples was justified by the alignment of filler flakes on the nanocomposite surface. As better filler alignment may result in regular surface wrinkling, which can impart the surface with better surface roughness. This is very convenient for droplet's rapid separation after contact. Furthermore, the thickness effect was also studied, and assumptions have proposed in favor of hydrophobicity.

3.1.1 Materials

PDMS elastomer and cross-linker were purchased from HSSTS-sylgard. The rGO was obtained from Chengdu Organic Chemicals Co., Ltd. All other chemicals and solvents were analytical grade and have been used without further modification or purification.

3.1.2 Preparation of PDMS-rGO nanocomposite solution

In order to synthesize the nanocomposite solution, at first, six PDMS elastomer solutions of same weight (9.56 g) were taken in six separate conical tubes. Varied quantities of rGO (0.5 mg, 0.8 mg, 1.2 mg, 1.8 mg and 2.8 mg) were taken to mix with the curing agent solution (.956 g). The different rGO-curing agent mixture solutions were initially taken through ultrasonication for around 1h individually, which was further followed by magnetic stirring at 700 rpm. These phenomena were conducted to exfoliate the rGO flakes, which are generally bonded with π - π stacking. Then, all the rGO solutions were mixed with the PDMS elastomer solutions and were stirred further at 700 rpm for 1h to get the nanocomposite solution. One pristine PDMS solution (PDMS elastomer-curing agent at 10:1) was also prepared in the same course. Since all the solutions contained numerous air bubbles, they were kept in a vacuum chamber for 30 minutes for degassing.

3.1.3 Fabrication of Single Electrode Mode TENG

The fabrication process flow of the proposed SEM-TENG has been demonstrated in **Fig.15**. Initially six silicon wafer substrates were cleaned with DI water, ethanol, acetone, argon gas flow and subsequently dried on a hot plate at 70°C. Secondly, these substrates were further treated with chlorotrimethylsilane before drop casting process. At the following step, as prepared pristine PDMS (PP) and nanocomposite solutions were poured on to all individual silicon wafer substrates using conventional drop casting process. Afterwards, the solutions were spin coated at different rpm speeds i.e. 250, 350, 450 respectively to obtain thickness variation of each film. The samples were then kept in an oven at 75° for thermal curing for 12h. At the subsequent step, the dried films were peeled off from the underneath Si wafer substrate and Au electrodes were deposited on one side of each film using magnetron sputtering technique. Finally, one edge of a platinum (Pt) wire was attached with each electrode using Silver (Ag) epoxy glue and the other end was connected to ground for making SEM-TENG setup. These SEM-TENG devices have surface area ~ 2 cm*2 cm (length*width), along with 537 μm, 149μm and 141μm thicknesses respectively for each PP and nanocomposite films. **Fig. 16**. Shows the optical images of as prepared PP, nanocomposite film samples as well as the SEM-TENG device setup for experiment.

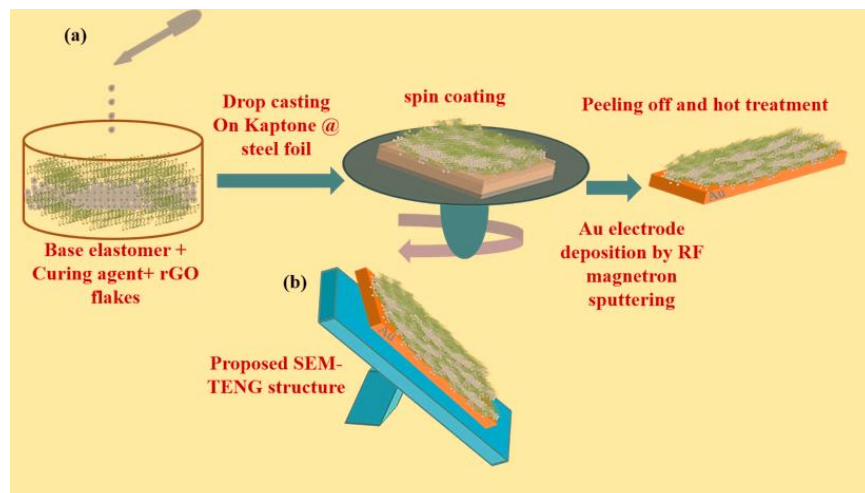


Fig.15. (a) Synthesis procedure of PRNC thin film (b) SEM-TENG structure

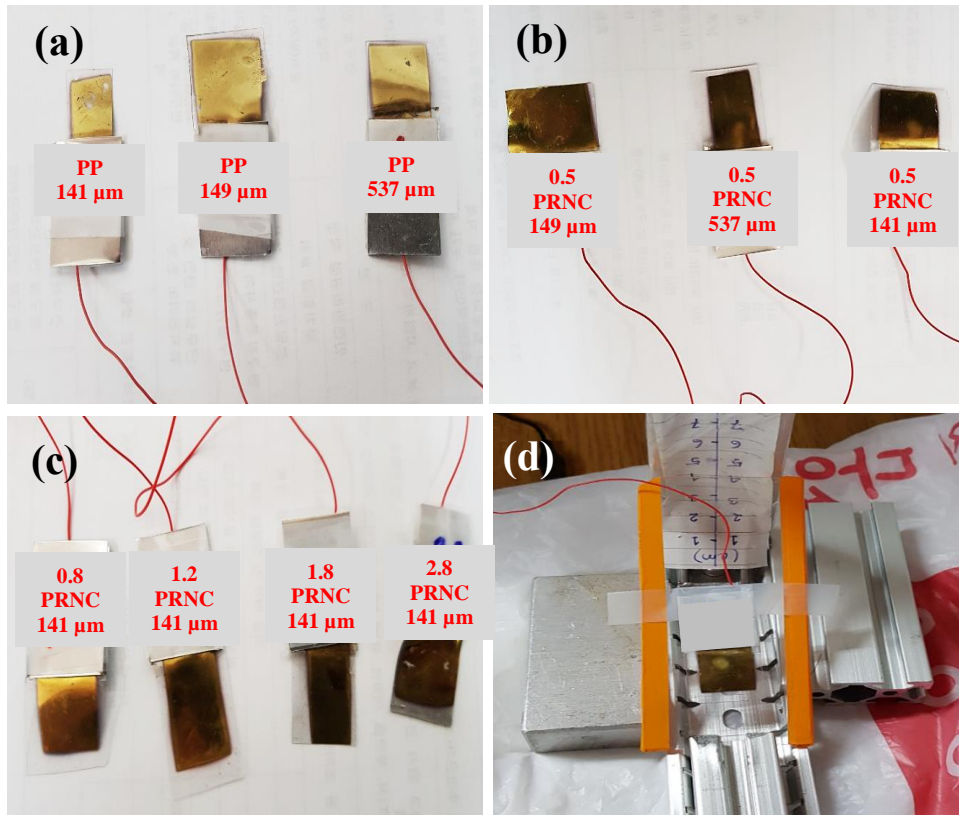


Fig 16. Optical Images of (a) Pristine PDMS films (thickness 141 μm , 149 μm and 537 μm respectively-from left to right); (b) 0.5 PRNC films (thickness 149 μm , 537 μm and 141 μm respectively-from left to right); (c) 0.8 PRNC, 1.2 PRNC, 1.8 PRNC and 2.8 PRNC films

3.2 Quantitative Measurements & Material Characterization

Device Name	Evaluation Parameters
SEM-TENG	Inclined at an angle of 45°, which is the industrially preferred standard (according to ISO 1514:2004 (E)) [58]

Regular ruler	height between the pipette tip and the triboelectric nanocomposite film was maintained at 55 cm
Keithley Digital Multi Meter	Output signals of SEM-TENG device test
Contact Angle Meter (Smart Drop Plus, FEMTOBIOMED)	Water-contact angle measurement
Field Emission Scanning Electron Microscope (Nova Nano230 FE-SEM)	Images of surface and cross-sectional morphologies; and thickness of as prepared films have been studied.
Energy-dispersive x-ray (EDX) spectroscopy (Nova Nano230 FE-SEM)	Quantitative elemental information of prepared samples
Varian 2000 Scimitar spectrometer	Fourier Transformed Infrared (FTIR) spectroscopic analysis
Alpha300S microscope (WITec)	Raman spectra of PP and nanocomposite films were recorded
3D laser scanning Confocal Microscope (VK-X200 series, Keyence, Japan)	Thickness of rGO (with varied amounts) flakes was measured

3.2.1 Scanning Electron Microscopy (SEM)

This is such an electron microscope which is able to capture high resolution images (better 1 nanometer). Images have been produced by scanning the sample surface area with the incidence of electron beam. This focused beam is comprised of numerous electrons which interact with the atoms of surface area under scanning zone and generates information on the morphology and elemental composition. In this research, the surface topographies, various elements' quantitative composition (EDX) and the thickness of the samples have been determined using this characterization technique.

3.2.2 Energy-Dispersive X-ray (EDX) Spectroscopy

This analysis provides the information about the identity of elements present on the surface and their proportional composition. X-ray excitation is generated and is provided to the particular surface zone. As every element present in the scanning zone possess a unique atomic structure, thus depending this structure a set of peaks are appeared indicating the atomic and weight percentage of individual elements. In this thesis, these information were extracted for the prepared samples.

3.2.3 Fourier Transformed Infrared (FTIR) spectroscopy

This a technique where a wide range of infrared can be passed through test samples in order to obtain an infrared spectrum of transmittance or emission. This obtain spectra refers to the molecules' individual vibration characteristics as well. FTIR is the spectroscopy, by the use of which, identification of known and unknown material compounds can be revealed. Moreover, presence of chemical functional groups and their corresponding type of vibration can be achieved. In this work, with FTIR analysis of each test samples, we tried to determine the functional groups or molecular bonding information.

3.2.4 Raman Spectroscopy

This is a non-destructive chemical analysis technique, which gives several information like chemical structure, chemical bonding, phase and defect in a structure through a light scattering process, called Raman scattering. The Raman spectrum profile i.e. peak position and peak intensity usually indicates the identity of a particular material. However, the peak provides information about the concentration of one particular material. In this thesis, the Raman spectrum were used to study the polymer and filler interaction, skeleton structure of filler and defects if there is any due to being embedded in polymer matrix.

3.2.5 Confocal Microscopy

Confocal microscopy is such a technique where a focused fluorescent light is emitted from the microscope to incident on the aimed object for the generation of high-resolution images. Through capturing multiple 2D images throughout a sample, its possible to obtain a 3D image. Height profile, thickness-type parameters are very convenient to measure with the help of this microscope. The only limitation is that its able to read data in micro scale range, not in nanoscale range. Since in this thesis, our filler thickness was in micro-level, thus confocal microscopy worked as the best choice. The optical height was determined by the incident laser from the microscope to the test sample.

3.2.6 Water Contact Angle

Water contact angle of the prepared sample were measured with Smart Drop Plus, FEMTOBIOMED contact angle meter using sessile drop method at the room temperature. The distilled deionized water was used as the droplet to be dropped on the thin pristine polymer and nanocomposite film surfaces for determining their hydrophobicity. Its important to mention that,

several liquids can be used as droplets and thus surface energy measurement is also possible with this given equipment.

3.2.6 X-ray Photoelectron Spectroscopy

This is such a quantitative spectroscopic technique which is able to determine the surface elemental, chemical and electronic state. The spectrum can be achieved through the irradiation of the targeted surface with a beam of x-rays. At the same time, the kinetic energy and quantity of the escaping electrons are also analyzed with this technique. High vacuum e.g. $P < 10^{-9}$ millibar is much desired to perform experimentation on this technique. Usually the output spectra will provide peaks against binding energies of individual molecular bonds present on the surface. Almost all kind of materials i.e. organic/inorganic compounds, metals, polymers, semiconductors, composites etc can be analyzed with this spectroscopy.

Chapter 4

Analysis of Results and Working Mechanism

4.1 Results and Discussion

The fundamental working principle of TENG is based on well-known contact and separation phenomenon between two asymmetric materials with different electron affinities. Thus, it is quite important to ensure that this phenomenon occurs efficiently. As this current work is concerned on triboelectrification between water droplet and as proposed surface, separation of droplets is a very crucial thing to get better triboelectric outputs. In such case, hydrophobic property of these as prepared samples should be addressed well. In order to obtain an optimized hydrophobic nanocomposite surface, a non-uniform/rough surface is more desired rather than having a uniform or flat one. Through this research, we have proved that water-repellent surface can be attained by including optimized quantity of fillers (rGO) material into PDMS polymer matrix. **Fig. 17.** shows the EDS elemental analysis to quantify the effect of rGO addition in polymer matrix. The EDS spectrum for different samples showed their variation according to the filler inclusion phenomenon. For further clarification, the weight percentage (% wt) of the individual element contents i.e. carbon (C), Oxygen (O), Silicon (Si) have been summarized in **Table 4.** A clear tendency of C content rise was observed, and maximum quantity was found 27.12% for 2.8 PRNC. In addition, maximum amount of O content was found for 0.5 PRNC nanocomposite sample containing utmost 24.76% O content, which indicates the presence of O containing functional groups. However, with incorporation of rGO flakes, these functional groups got reduced because of the overlapped/restacked rGO flakes along the basal plane. Therefore, reduction of O content was noticed for further filler integrated nanocomposite samples.

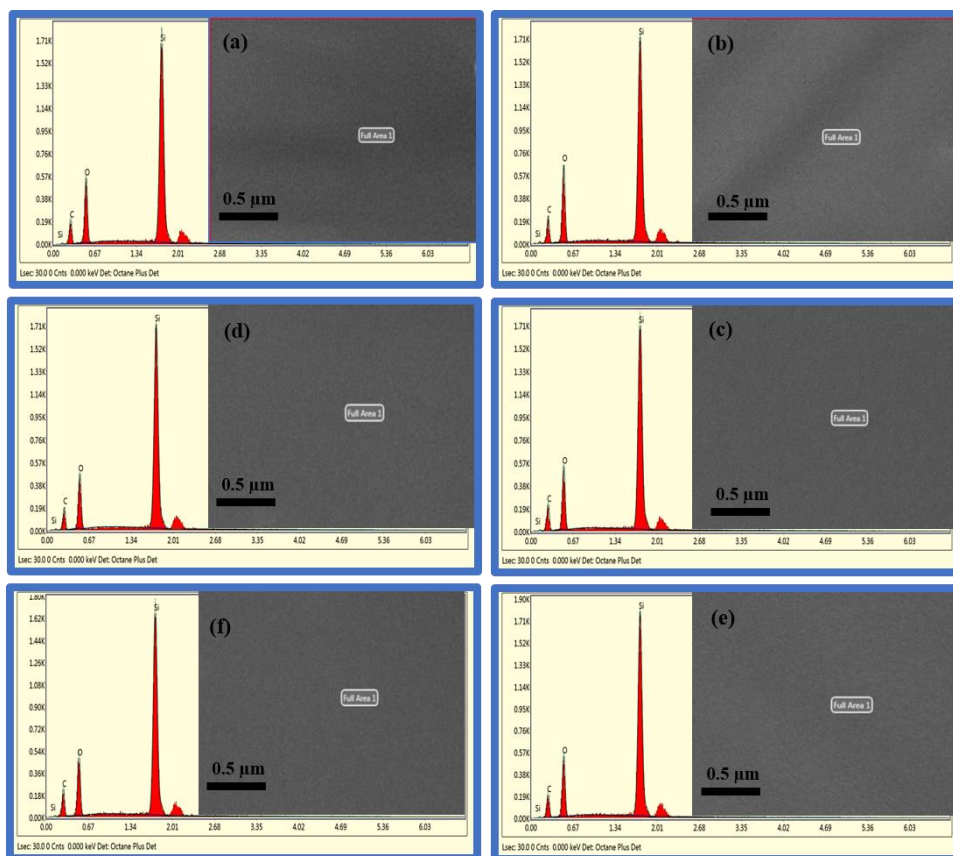


Fig.17. EDS elemental analysis of (a) Pristine PDMS, (b) 0.5 PRNC, (c) 0.8 PRNC, (d) 1.2 PRNC, (e) 1.8 PRNC, and (f) 2.8 PRNC

Table 4. EDS elemental analysis

Element	Pristine PDMS (%wt)	0.5 PRNC (%wt)	0.8 PRNC (%wt)	1.2 PRNC (%wt)	1.8 PRNC (%wt)	2.8 PRNC (%wt)
C	25.26	24.77	26.74	24.41	26.19	27.12
O	22.55	24.76	21.73	20.67	21.99	21.60
Si	52.19	50.47	51.52	54.92	51.82	51.27

Roughness in these resultant nanocomposite surfaces has been induced via formation of wrinkled micro-structure due to the encapsulation of PDMS polymer around dispersed rGO flakes, as seen in FE-SEM surface morphology in **Fig. 18**. It was clearly observed that on the 0.5 PRNC nanocomposite surface the flakes were well-dispersed and formed wave-shaped wrinkled structure (**Fig. 18(b)**), which caused non-uniformity. These rough surface patterns bestowed the nanocomposite surface with better water-repellent property in comparison to flat PP surface (**Fig. 18(a)**). **Fig. 19** represents the optical images of contact angles for triboelectric PP and nanocomposite films. The water contact angle was measured 116.9° for 0.5 PRNC, whereas lower contact angle 107.2° was noticed for PP. However, for 0.8 PRNC (**Fig. 18 (c)**) wrinkled patterns tend to merge due to increased amount of fillers, and hence surface roughness got reduced, which is evident from the contact angle value i.e. 114.1° of this nanocomposite film. With the further quantity increase of rGO flakes in the matrix we found overlapping patterns (**Fig. 18(d)**) on the surface morphology of 1.2 PRNC and eventually some aggregated rGO flakes were visible on the surfaces (**Fig. 18(e,f)**) of 1.8 and 2.8 PRNC films respectively. Therefore, most of the surface of these later samples lacked surface roughness and pertained almost pristine properties, as observed for PP film. Such occurrence instigated surface wetting tendency and lower contact angles i.e. 109.5° , 105° were detected for 1.8 and 2.8 PRNC films respectively as a result.

The dispersion phenomenon of rGO fillers can be further explained by filler amount variation and their effect in PDMS matrix, which can be observed in FE-SEM surface and cross-sectional morphologies shown in Fig. 3 and Fig. 5 respectively. If these both figures are considered together, then it is clearly visible that pristine PDMS is nothing but a plane polymer with no surface perturbation (**Fig. 18(a)**, **Fig. 20(a)**). However, when rGO is added in a very small quantity (0.5 mg) then the surface wrinkling was observed (**Fig. 18(b)**). In this case, the rGO flakes were fully

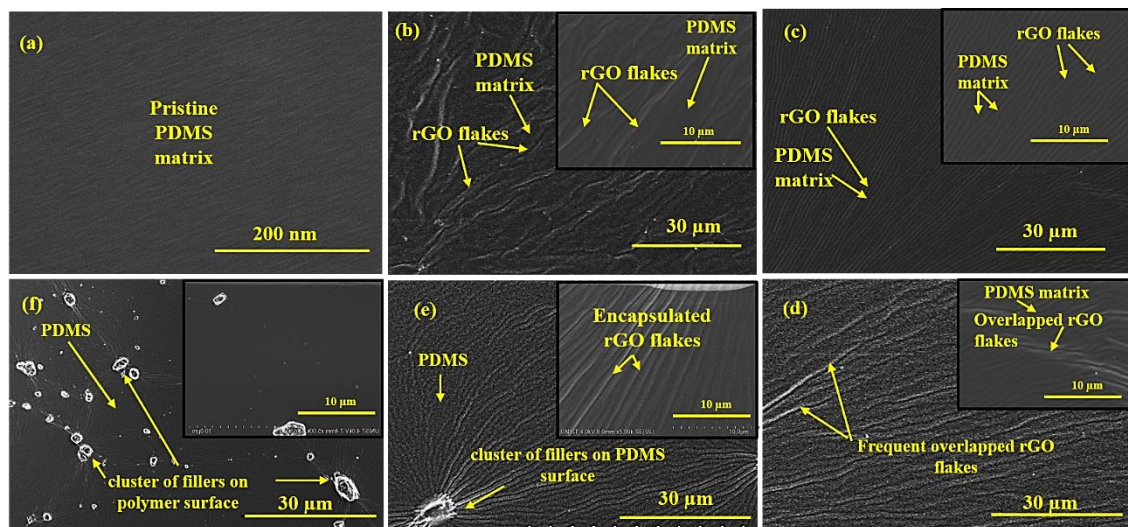


Fig. 18. FE-SEM surface images of (a) Pristine PDMS, (b) 0.5 PRNC, (c) 0.8 PRNC, (d) 1.2 PRNC, (e) 1.8 PRNC, and (f) 2.8 PRNC

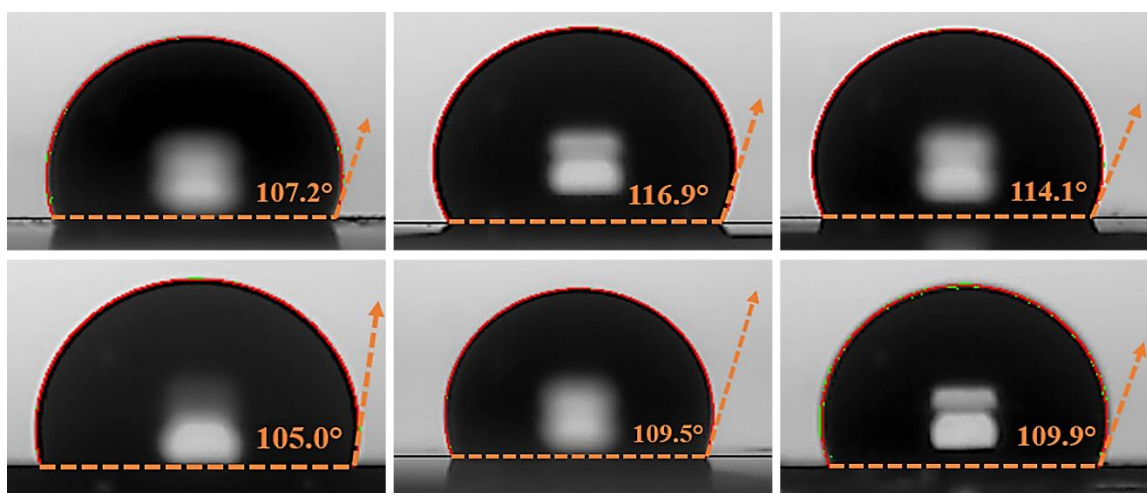


Fig. 19. Optical water-contact angle images of (a) Pristine PDMS, (b) 0.5 PRNC, (c) 0.8 PRNC, (d) 1.2 PRNC, (e) 1.8 PRNC, and (f) 2.8 PRNC

wrapped by the adhesive PDMS polymer after the curing process. These wrinkling seemed quite regular in nature in the surface morphology images and were further elucidated from the cross-section morphology (**Fig. 20(b)**). These regular wrinkling proved the better dispersion of fillers on the surface as well as in the bulk matrix. On the other hand, when a little more filler was added in the polymer e.g. 0.8 PRNC, the wrinkles appeared to coalesce instead of maintaining well-ordered morphology (**Fig. 18(c)**, **Fig. 20(c)**). This scenario indicated the tendency of rGO flakes to consolidate with each other. Therefore, the desired regular dispersion was compromised in this case. This The subsequent samples demonstrated wrinkles originated from overlapping rGO flakes for 1.2 PRNC film (**Fig. 18(d)**, **20(d)**), and clustered filler flakes formed on 1.8 PRNC (**Fig. 18(e)**, **20(e)**) and 2.8 PRNC film (**Fig. 18(f)**, **20(f)**) respectively. In these later samples, we found that the dispersion started to weaken as these flakes were showing high agglomeration behavior owing to their substantial specific energy [152,153]. Therefore, considerably lower amount of filler inclusion has been inferred to be the best choice for this work.

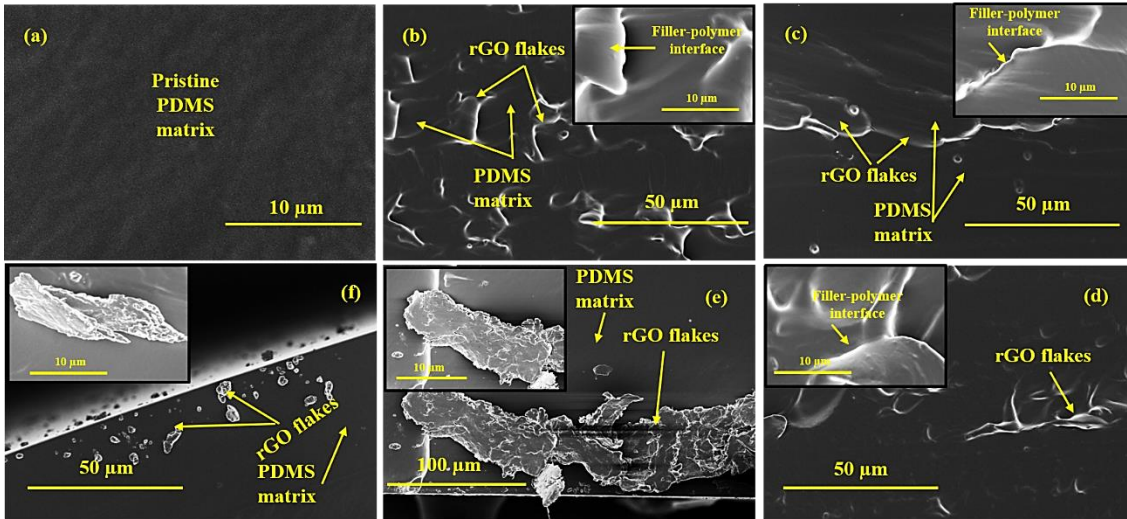


Fig. 20. FE-SEM cross-section images of (a) Pristine PDMS, (b) 0.5 PRNC, (c) 0.8 PRNC, (d) 1.2 PRNC, (e) 1.8 PRNC, and (f) 2.8 PRNC

Confocal Raman spectroscopy (**Fig. 21**) exhibited interaction between PDMS polymer and rGO flakes added into it. The D-band and G-band in case of pristine rGO have been observed at $\sim 1352\text{ cm}^{-1}$ and $\sim 1592\text{ cm}^{-1}$ respectively, which is quite similar to the existing literature [154]. However, when this pristine rGO (PrGO) was used in the PDMS matrix as a filler material with different concentration, the D and G bands behaved quite differently through their wavelength shifting, and peak size and intensity changing phenomena, as observed in Raman spectra. Variations in rGO bands' spectral features, while being infilled in polymer matrix, indicate their interaction with the polymer matrix or between themselves. For instance, intensity decrease of D & G bands of rGO in each nanocomposite spectrum, while being compared with PrGO, may be due to the encapsulation of rGO flakes by polymer. According to existing literatures, wavelength shifts of 0.5 PRNC could be ascribed to filler-polymer interlocking interaction in the matrix [154,155]. But, since both D & G bands were found to be down-shifted, filler-filler interaction could be concluded to be quite higher than filler-polymer [156]. Slight increase in I_D/I_G indicated the perturbation in rGO structure because of the presence of PDMS matrix. However, with the increasing amount of filler content (beyond 0.5 PRNC) e.g. for 0.8 PRNC, the D & G spectra did not shift, if compared with PrGO. Their I_D/I_G , peak size and peak intensities increased instead. Increase of gradual D-band strength and I_D/I_G can be attributed to polymer coating interference on rGO skeleton or coating on carbon particles besides rGO sheets [155]. Furthermore, as we mentioned earlier that stacked or overlapped rGO flakes might cover the functional groups present on the basal plane, this phenomenon could be assumed to induce defect in the rGO structure. At the same time, due to presence of apparently merging rGO sheets, rise in G-band intensity was also observed. Additional filler incorporation caused further augmentation of these properties, which could be clarified from Raman spectrum of succeeding nanocomposite samples. Furthermore, the

underlying reason behind D-band and G-band peaks' unusual broadening of 0.8 PRNC and following samples could be explained with the overlapping of several rGO flakes together, which could form multi-layers of rGO sheets [157]. Finally, peaks originated from PDMS polymer also showed intensity variation owing to the presence of rGO in the matrix. The peak intensity of Si-O-Si symmetric stretching (488 cm^{-1}) increased gradually in nanocomposite samples due to existence of oxygen-based functional groups in rGO fillers. Moreover, enormous carbon rings in the rGO molecular structure contributed to elevate the intensity of Si-C symmetric (708 cm^{-1}) and asymmetric (787 cm^{-1}) stretching present in bulk PDMS matrix.

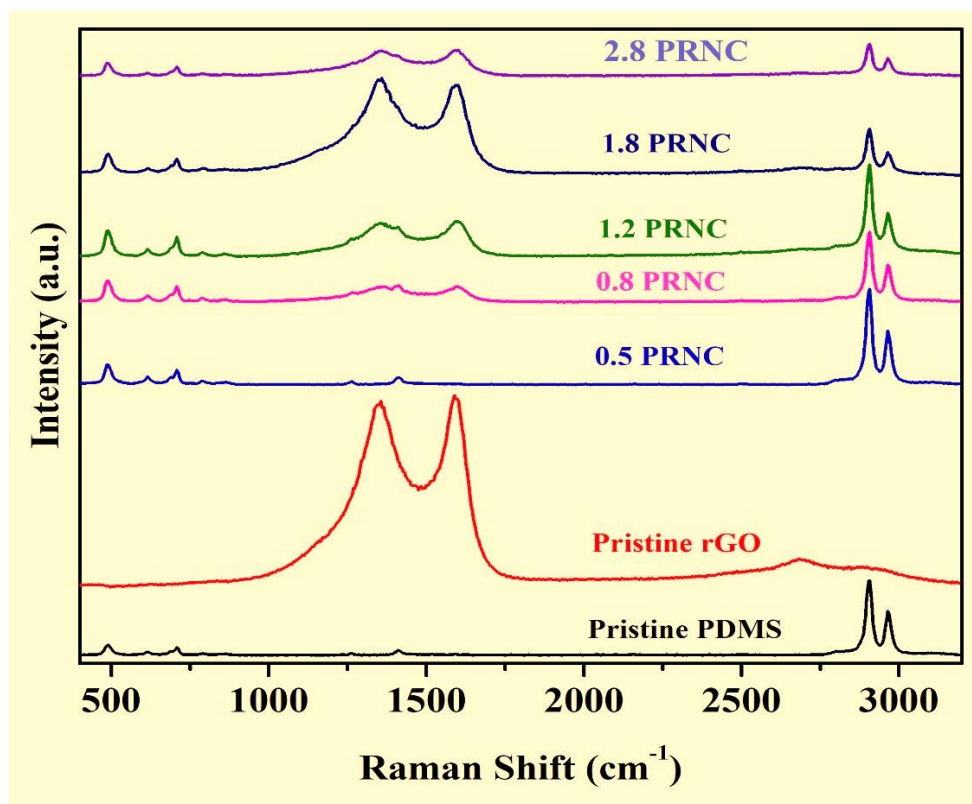


Fig. 21. Confocal Raman Spectroscopy

The evidence of poor chemical interaction between pristine PDMS and rGO can be clarified further from the FTIR spectra of transmittance, as observed in **Fig. 22**. If the spectra of pristine PDMS is

considered prior to nanocomposite sample spectra, then it can be observed that $(\text{Si-CH}_3)_2$ bonding of out-plane oscillations and in-plane bending are present in wavelength $\sim 794 \text{ cm}^{-1}$ and $\sim 1262 \text{ cm}^{-1}$ respectively [158,159]. In addition, doublet peaks at $\sim 1017 \text{ cm}^{-1}$ and $\sim 1080 \text{ cm}^{-1}$ also indicate the presence of symmetric and asymmetric Si-O-Si bonds respectively [158,159]. Moreover, the appearance of Si-C at $\sim 845 \text{ cm}^{-1}$, asymmetric $-\text{CH}_3$ at $\sim 1412 \text{ cm}^{-1}$ and $\sim 2961 \text{ cm}^{-1}$ also complied with the literature [158–160]. Now, after incorporation of rGO fillers, we did not see any noticeable variation in the spectra of nanocomposite samples. This finding confirmed the absence of chemical interaction between the filler and polymer matrix [159]. Therefore, these FTIR results further supported the claim made in Raman spectroscopic analysis that the chance of filler-polymer interaction is very meagre in these proposed nanocomposite samples.

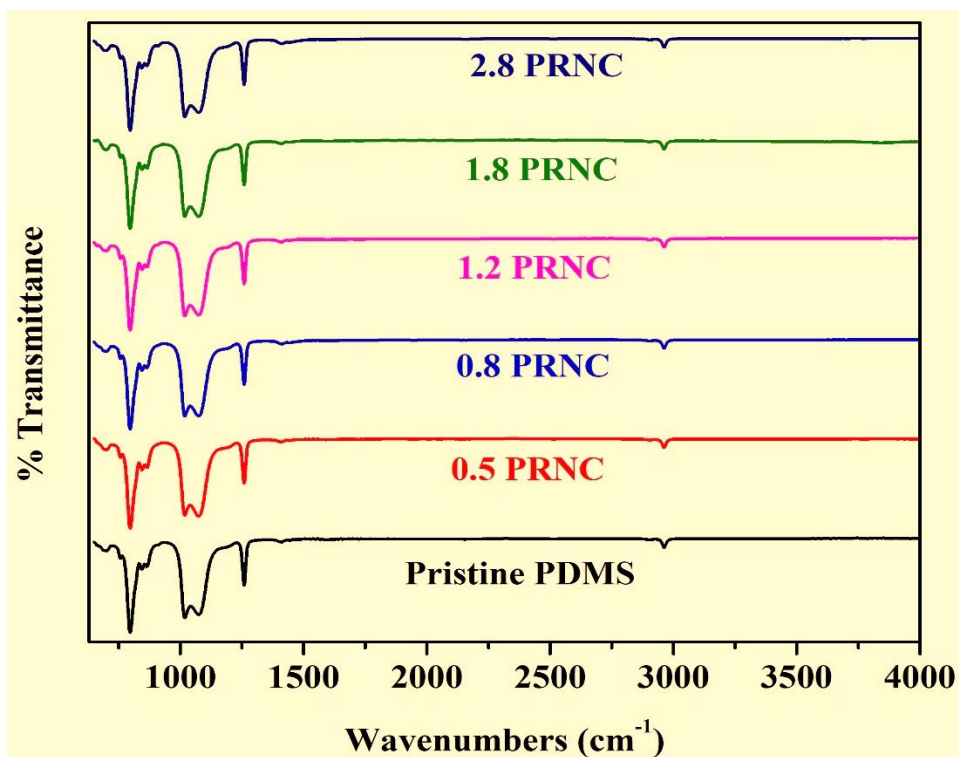


Fig. 22. FTIR Spectra of pristine PDMS and nanocomposite films

XPS characterization of the prepared samples has been used to determine chemical composition and surface state of those synthesized samples. **Table 5** shows the elemental composition of various elements in the test samples. Here an increasing tendency of C and O contents has been observed with the increasing filler quantity inclusion in the polymer matrix. This phenomenon almost matched the trend noticed in EDS (**Fig.17** and **Table 4**). **Fig. 23** demonstrates the survey scan full-spectrum and **Fig. 24** shows the core-level spectra of both pristine and nanocomposite samples. In **Fig. 23**, it can be clearly seen that the intensity of C1s and O1s peaks got higher in the nanocomposite samples compared with pristine PDMS. The reason behind this can be assigned to rGO filler addition. Among all the pristine and nanocomposite samples, 0.5 PRNC shows far higher C1s and O1s peak intensity compared to others. The additional carbon rings and O-based functional groups in rGO structure might be responsible for this. Although succeeding higher quantity filler included samples showed higher C1s peak intensity, their O1s peak intensity fluctuated. This phenomenon signifies the restacking/agglomeration of rGO flakes, as described in Raman spectroscopic analysis (**Fig. 21**). Moreover, the sudden decrease in peak intensity ratio (C1s : O1s) for nanocomposite samples, in comparison to the pristine polymer, further clarifies the significant increase of O content in the nanocomposite samples (as shown in **Table 5**).

Furthermore, the XPS core spectra for each sample, demonstrated in **Fig. 24 (a-f)**, might provide an insight on the presence of various bonds against their respective binding energies. It was found in almost all nanocomposite samples that the C1s spectra's peak binding energies were ~ 284 eV (with approx. deviation ± 0.3). Therefore, the existence of C-C/C-H could be anticipated there, which literally represented the graphene-structure [15–17,97]. Peaks noticed at ~ 532.9 and ~ 101.8 eV in the O1s and Si2p spectra respectively (**Fig. 24 (a-f)**) might be attributed to the existence of SiO₂ [98]. In addition, presence of SiC was also comprehended at ~ 100.7 eV in Si2p spectrum [99]

of each test sample (**Fig. 24 (a-f)**). In case of 0.8 PRNC and 2.8 PRNC samples, appearance of C-O-C was realized in C1s and O1s spectra, which was assumed to occur because of air contamination. As no new peaks appeared in the nanocomposites and no significant peak shifts observed, it can be inferred that there was least chemical interaction occurred between the fillers and polymer. This analysis also reinforced the results of Raman and FTIR analyses.

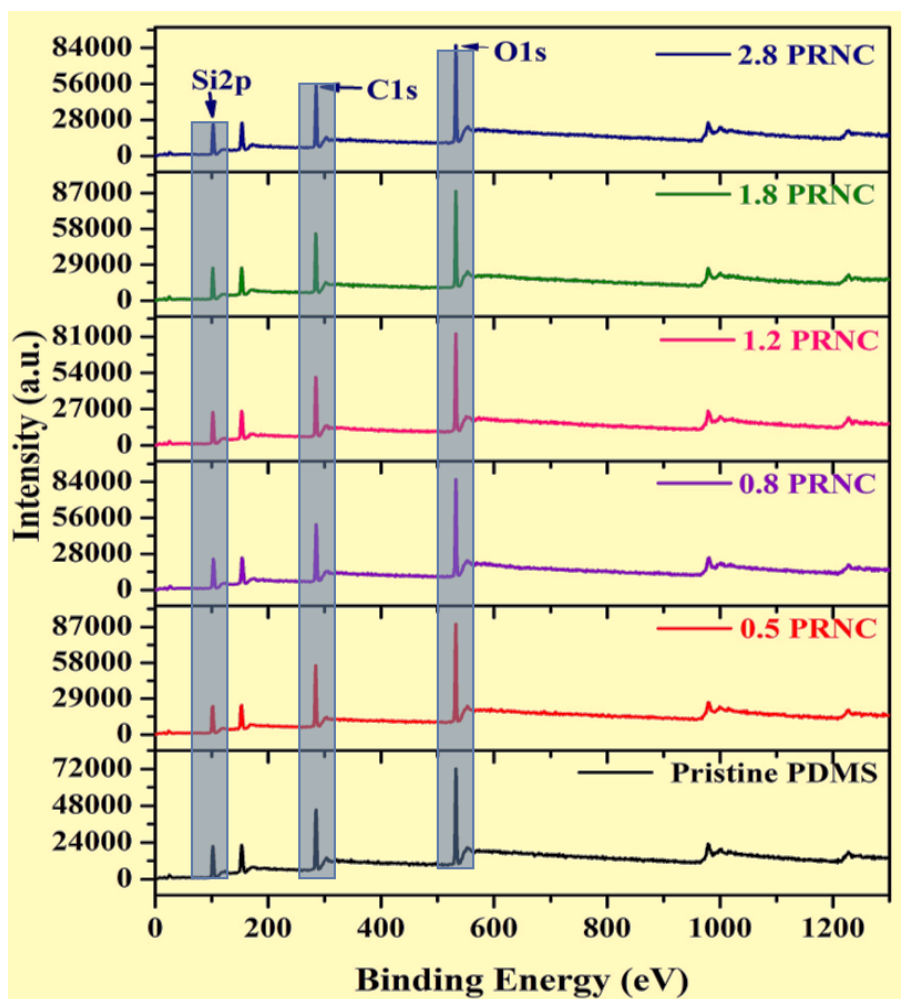
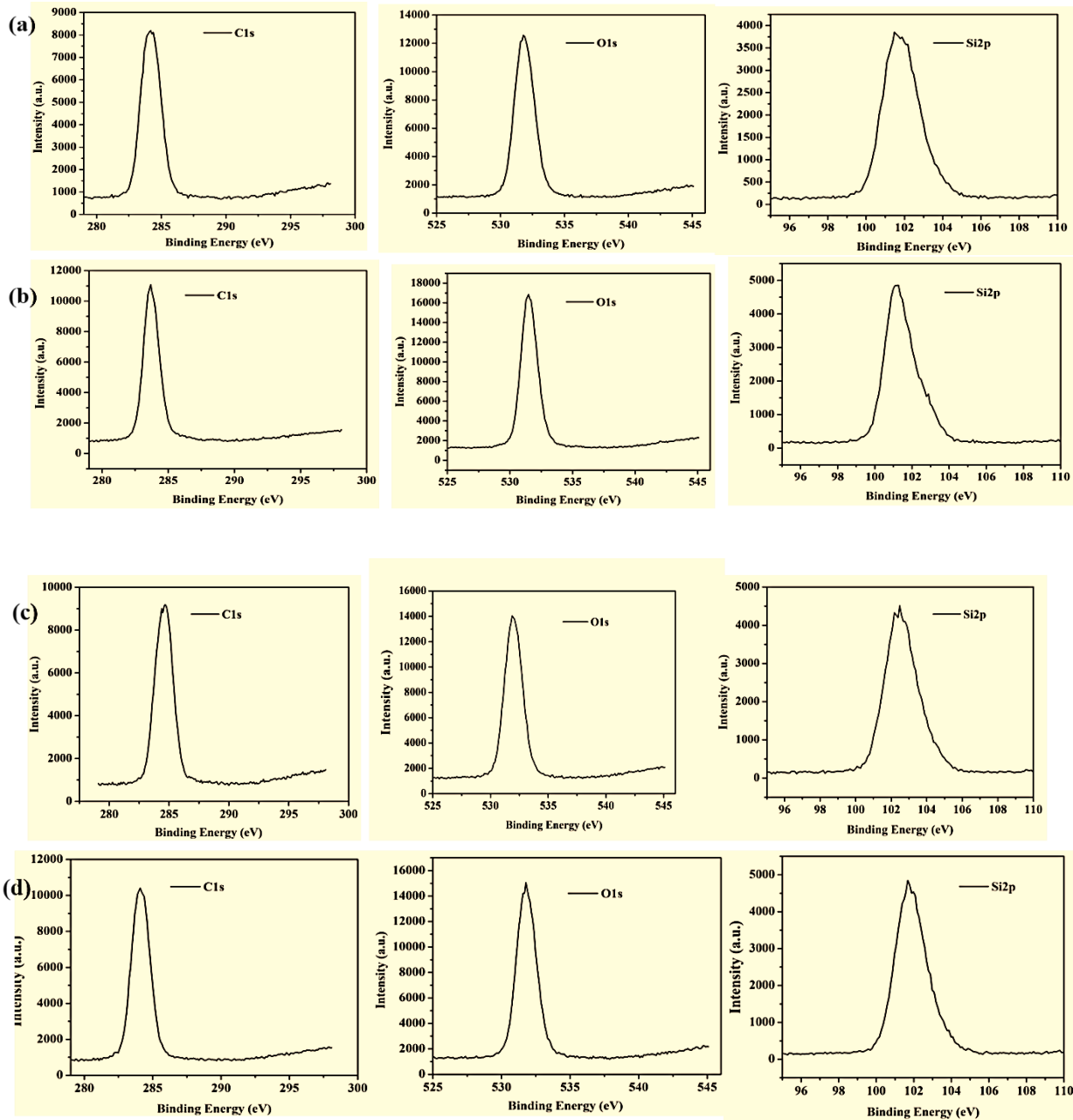


Fig. 23. XPS survey scan spectra for Pristine PDMS and nanocomposite films



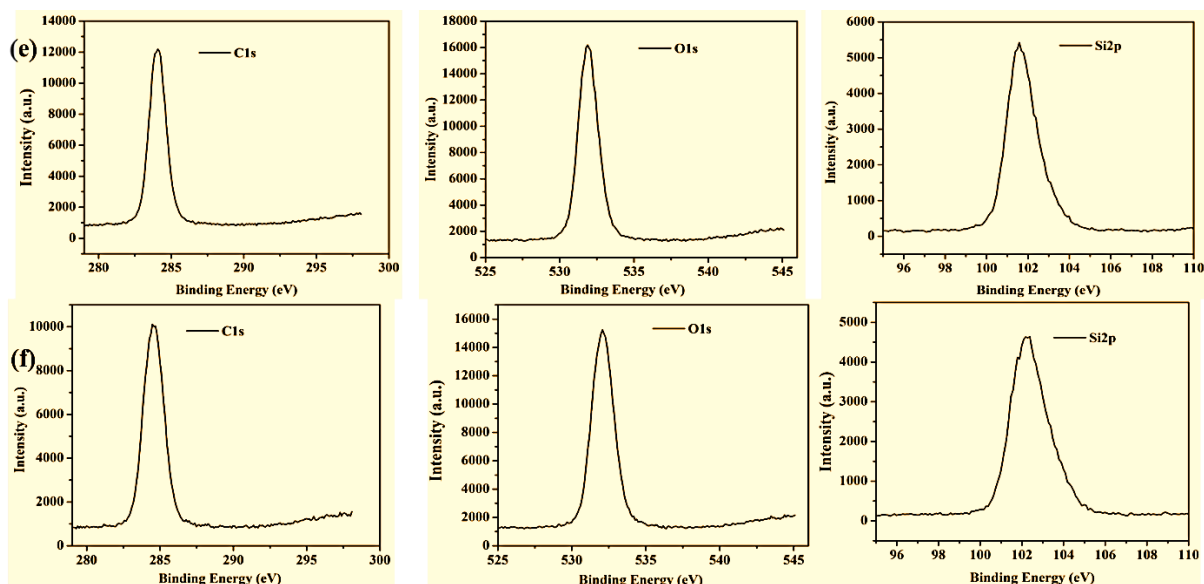


Fig. 24. XPS Core spectra for (a) Pristine PDMS; (b) 0.5 PRNC; (c) 0.8 PRNC; (d) 1.2 PRNC; (e) 1.8 PRNC; and (f) 2.8 PRNC.

Table 5. XPS analysis results for Pristine PDMS and nanocomposite samples

Sample	C (% at)	O (% at)	Si (% at)	Peak Intensity Ratio (C1s:O1s)
Pristine PDMS	44.46	27.08	28.46	1.561
0.5 PRNC	43.23	29.01	26.63	0.675
0.8 PRNC	43.95	27.44	28.61	0.642
1.2 PRNC	46.11	26.16	27.73	0.680
1.8 PRNC	45.43	27.31	27.26	0.738
2.8 PRNC	43.32	27.53	29.15	0.640

In order to clarify the performance of several nanocomposite films and to make logical comparison between them, it's also pivotal to study the thickness of rGO flakes. For this purpose, several aqueous solutions of rGO samples were prepared. In each solution, different quantities of rGO was dispersed in DI water and sonication was done for 30 minutes for each as prepared solution. Then one single drop of each solution was dropped over a properly cleaned silicon wafer substrate. After curing those droplets in an oven at $\sim 70^{\circ}\text{C}$ for 1 hour, only dispersed rGO flakes were obtained on

the substrate as the water particles evaporated during the heating. A confocal microscope was used to measure the thickness of the remaining rGO flakes on each substrate. **Fig. 25** revealed the average flake thickness through 3D topographical profiles, where the color code bar at the upper left of each profile indicated the numerical value of dispersed rGO flakes' thickness. Average thickness can easily be identified by spotting the “green color” and maximum thickness can be discerned by the “red color” on the topographic profiles and color code bars. From **Fig. 25(a)**, the average

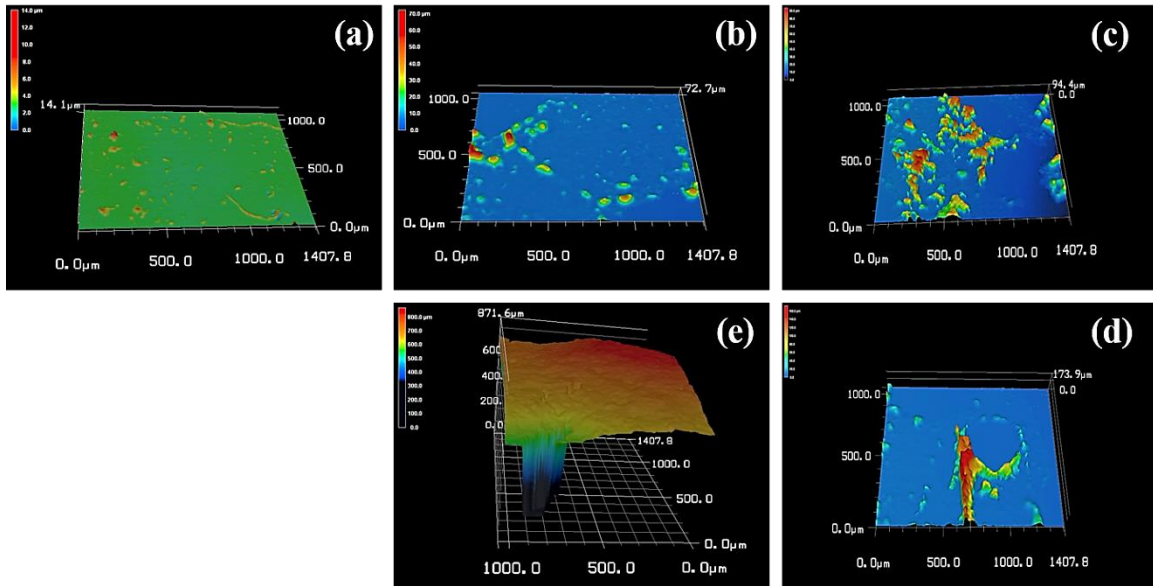


Fig. 25. Average rGO flakes' thickness for (a) 0.5 mg, (b) 0.8 mg, (c) 1.2 mg, (d) 1.8 mg and (e) 2.8 mg

Table 6. Average and Maximum thickness of dispersed rGO flakes with varied quantity

Sample	Average Flakes Thickness (μm)	Maximum Flakes Thickness (μm)
0.5 mg rGO	~4 μm	~14.1 μm
0.8 mg rGO	~20 μm	~72.7 μm
1.2 mg rGO	~40 μm	~94.4 μm
1.8 mg rGO	~60 μm	~173.9 μm

2.8 mg rGO	~700 μm	~836.1 μm
------------	--------------------	----------------------

thickness was found $\sim 2\text{-}4\ \mu\text{m}$ for 0.5mg rGO sample and flakes were spotted in well-dispersed condition throughout the whole surface. However, for the immediate higher quantity (0.8 mg) of rGO sample, as shown in Fig. **25(b)**, the average thickness raised to $\sim 20\text{-}30\ \mu\text{m}$. In this case, along with thickness proliferation, aggregation was also detected although dispersion was better than the following samples. These phenomena resembled with the surface and cross-sectional morphologies of 0.8 PRNC film in **Fig. 18(c) and 20(c)**. Highest average flake thickness was found for 2.8 mg sample (Fig. **25(e)**), which was around $\sim 700\ \mu\text{m}$ and maximum thickness was noticed $\sim 836.1\ \mu\text{m}$ for this very sample. This observation also validated the agglomerated rGO flakes on polymer surface and cross-section (**Fig. 18 (f), 20 (f)**). The average and maximum flake thicknesses of varied rGO samples have been presented in **Table. 6** for better comprehension.

For further illustration of efficacy of the nanocomposite films, the alignment of rGO sheets have been considered. Previous literature [52] has proved that spin-coating assisted nanocomposite films would provide better dispersion and alignment of filler sheets in the polymer matrix. In addition, Wand D.R. et al have shown that along with good dispersion of fillers, strong interfacial interaction can also be achieved by spin-assisted coating [161]. These several favorable properties were also observed in surface and cross-section morphology analysis, (as shown in **Fig. 18** and **Fig. 20**) and Raman spectroscopic analysis (as illustrated earlier) for the nanocomposite films presented in this current work. After measuring the output voltages of PP, 0.5 PRNC, 0.8 PRNC, 1.2 PRNC, 1.8 PRNC and 2.8 PRNC films (as shown in **Fig. 26**), it has been investigated that 0.5 PRNC induced more output peak to peak voltage $\sim 2\text{V}$ (**Fig. 26(b)**). Topmost I_{SC} peak was observed

~2 nA (**Fig. 32 (b)**) from this nanocomposite film-water droplet contact triboelectrification output.

These results validated the aforementioned discussion of 0.5

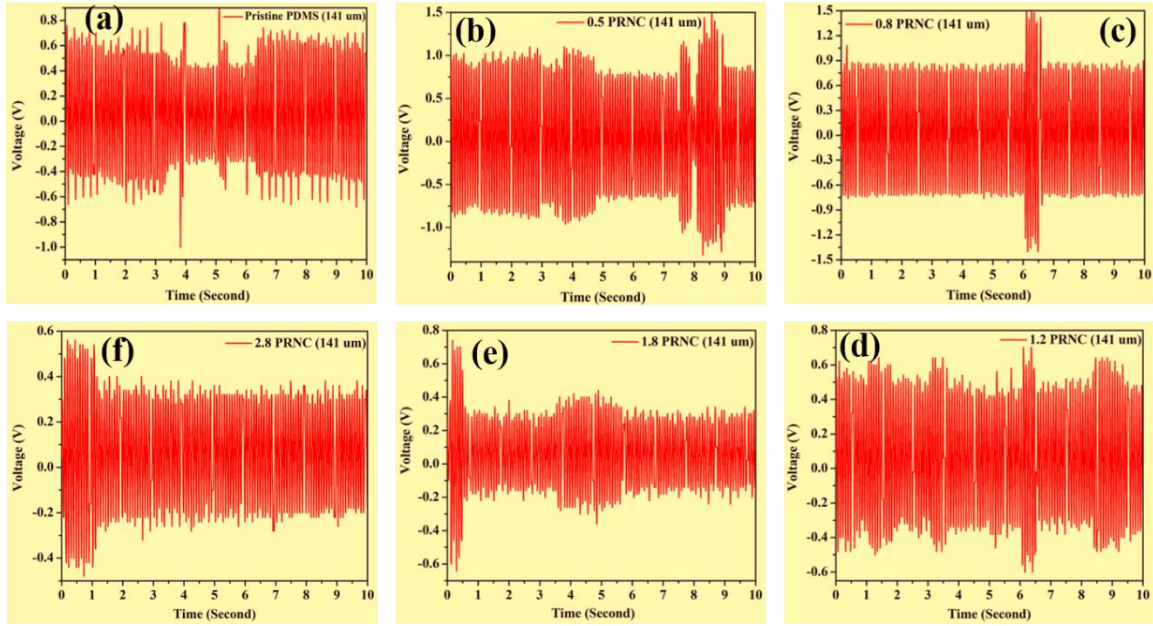


Fig. 26. Open Circuit Voltage (V_{oc}) of (a) Pristine PDMS, (b) 0.5 PRNC, (c) 0.8 PRNC, (d) 1.2 PRNC, (e) 1.8 PRNC, and (f) 2.8 PRNC

PRNC to be an efficient triboelectric material. Until now the reasons behind this optimized output could be assigned to proper dispersion of filler flakes in polymer matrix and their alignment, filler thickness, interfacial interaction, surface roughness due to evolving of wrinkled micro-structure. In addition to these, dielectric properties and thickness of these as fabricated test films are also significant factors to further optimize their suitability.

To explain more, dielectric properties of PP and rGO@PDMS nanocomposite films were measured at room temperature and over the frequency range from 2×10^4 Hz to 1×10^5 Hz. Samples were prepared by depositing Au electrode in circular pattern (area of each circular electrode were determined 0.5 mm^2) using RF magnetron sputtering technique. **Fig. 27 (a)** shows the dielectric

constant trend for varied filler incorporated nanocomposites over the above-mentioned frequency range. Several changes have been identified while analyzing the gradual increasing and then decreasing attitude of dielectric constant curves. The sharp rise of dielectric constant from PP to 0.5 PRNC indicates the formation of numerous micro-capacitor model due to increasing rGO concentration. For instance, for pure PDMS thin film, the dielectric constant was found ~ 8.6 at frequency 60 kHz, whereas for 0.5 PRNC the constant was noticed at ~ 22.7 under same frequency. This happened due to the rGO filler addition in the container matrix. Here the rGO fillers can be regarded as electrodes and polymer matrix can be interpreted as dielectric medium. Therefore, two adjacent rGO sheets and thin polymer film in between can form capacitor model. Myriad capacitors were formed in this process and can be addressed as micro-capacitors. These newly formed micro-capacitors promoted the capacitance of the thin triboelectric composite films, which consequently enhanced the dielectric constant. Hence, voltage generated due to contact separation of the sliding droplets over the film surface will be distributed among these micro-capacitors and amplified voltage and more electrical energy storage can be realized [52,53]. However, following higher filler quantity enhanced nanocomposite films showed gradual decrease of dielectric constant values at identical frequency. This can be attributed to the van der waals forces acting between the amphiphilic rGO flakes which resultantly decrease the distance between them as the filler concentration increases in the polymer. In 0.8 PRNC film, the filler flakes tend to come close to each other and ended up merging in several places. Therefore, formation of consistent micro-capacitors got compromised, which resulted in declination of dielectric values. Further drop was observed for 1.2 PRNC due to mass overlapping of flakes in frequent places and in case of 1.8 PRNC film the flakes appeared on the surface as cluster due to gravimetric sedimentation. This phenomenon causes to form an asymmetric composite film [153,162]. If dielectric constant curves

for individual triboelectric films is carefully analyzed, then it should be perceived that for the lower frequency value the constant was higher. The underlying reason behind this might be higher span of relaxation time through which the dipoles can reorient under an applied electric field. On the contrary, a reverse tendency occurred at higher frequency and dielectric constant fell off [163].

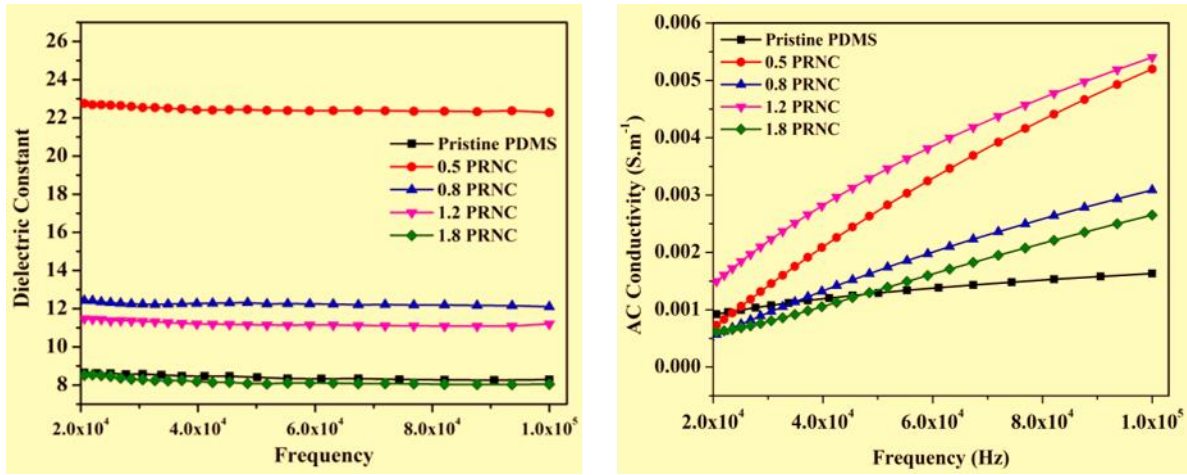


Fig. 27. (a) Dielectric Constant, (b) AC conductivity

In addition to dielectric properties, AC conductivity values under same frequency has been presented in **Fig. 27 (b)**. The conductivity got higher at the higher frequencies as increasing frequency would induce extra electrons, accumulated in the micro-capacitors, to hop across the filler-polymer interface [164]. It has been realized that lower filler mixed composite matrix posed higher conductivity ($\sim 0.32 \text{ S} \cdot \text{m}^{-1}$) than the pristine polymer film ($\sim 0.14 \text{ S} \cdot \text{m}^{-1}$) in this research. The reason can be ascribed to better conductive network between fillers at lower threshold. However, it also has been noted that conductivity trend revealed a very irregular trend onwards for other nanocomposite films. Although the filler flakes seemed to be merged for 0.8 PRNC in several places on surface, insubstantial conductivity might result from the absence of likewise rGO amalgamation across the entire measuring section. This is also an indirect indication of non-uniform dispersion of fillers throughout this whole nanocomposite sample. 1.2 PRNC film showed

highest conductivity ($\sim 0.37 \text{ S.m}^{-1}$) due to highly agglomerated and overlapped rGO flakes, whereas 1.8 PRNC thin film manifested far poorer conductivity ($\sim 0.15 \text{ S. m}^{-1}$), very close to pristine polymer film. Highly clustered flakes over polymer surface can be the rationale for this, while most of the polymer matrix lacked filler to form proposed capacitor model. Therefore, dielectric and conductivity properties were pretty adjacent to PP film.

Furthermore, the thickness effect of each nanocomposite film was also considered along with the parameters discussed before. The thickness of the as prepared nanocomposite films has been shown in **Fig. 28**. Prepared pristine and nanocomposite triboelectric samples have been tested for three different thicknesses $537 \mu\text{m}$, $149 \mu\text{m}$ and $141 \mu\text{m}$ respectively. At first, we compared between the thicknesses of three PP samples. A clear comparison of thickness difference has been shown in **Fig. 29** & **Fig. 30** for PP and 0.5 PRNC triboelectric nanocomposite films respectively. The peak to peak open circuit potential differences (V_{OC}) were found $\sim 0.5 \text{ V}$, $\sim 0.9 \text{ V}$ and $\sim 1 \text{ V}$ for $537 \mu\text{m}$, $149 \mu\text{m}$ and $141 \mu\text{m}$ thicknesses respectively, **Fig 31**. Similarly, we measured the same parameters for 0.5 PRNC sample and obtained $\sim 0.4 \text{ V}$, $\sim 2 \text{ V}$, $\sim 2 \text{ V}$ respectively (**Fig. 32**). From these observations, it was evident that thinner films came up with better output performance. The

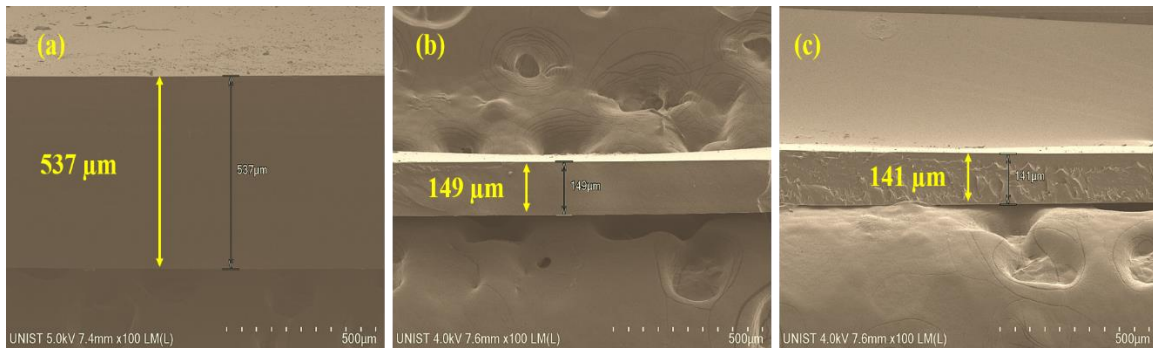


Fig. 28. (a,b,c) SEM Cross-sectional thickness of gradually thinning films

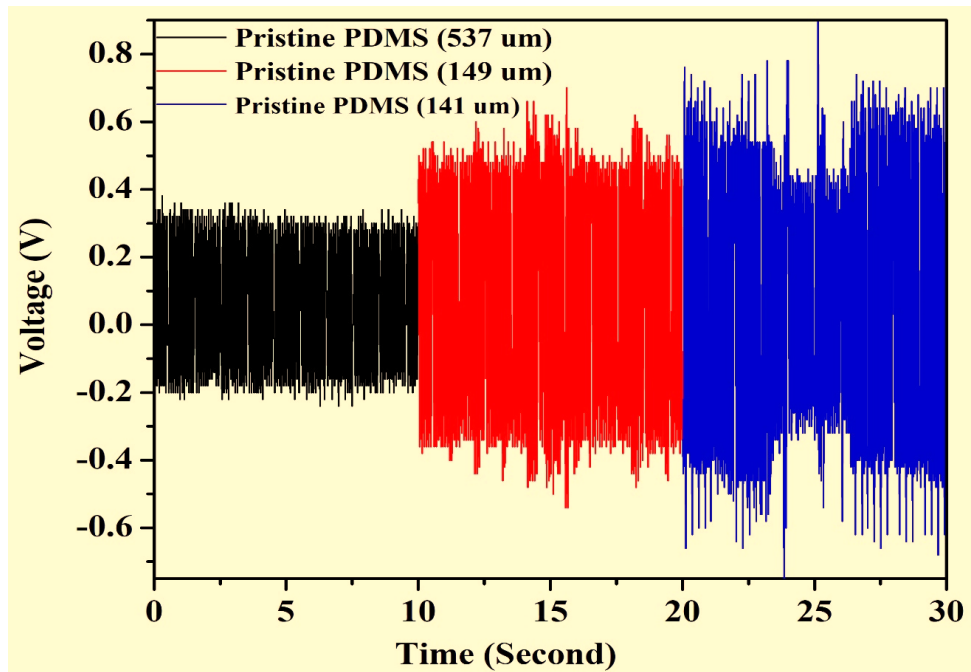


Fig. 29. Open Circuit Voltage (V_{oc}) comparison of Pristine PDMS with thickness variation

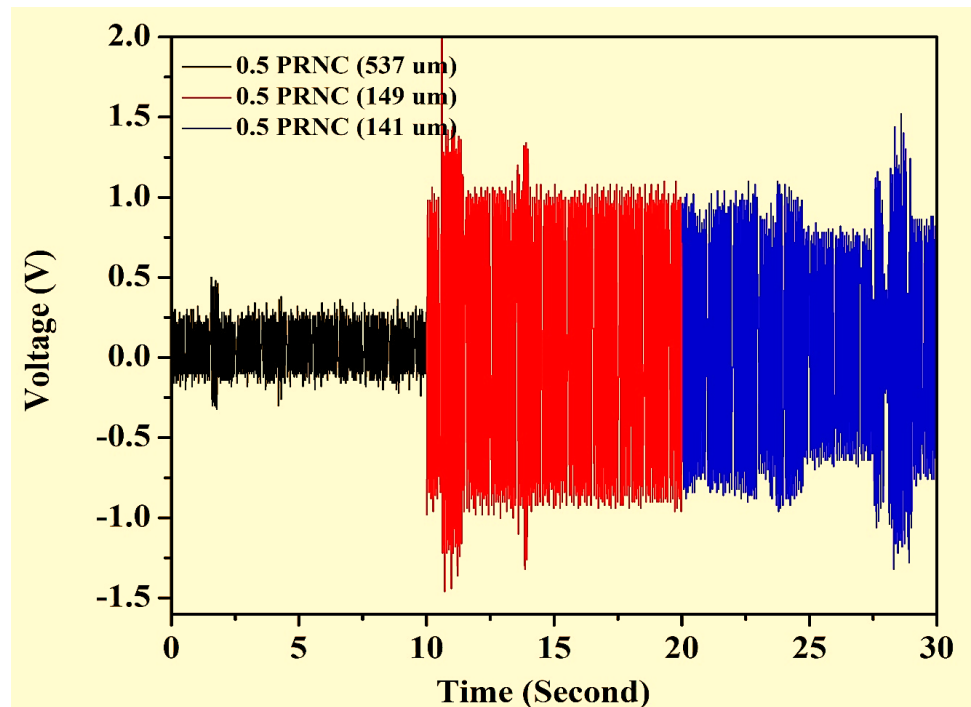


Fig. 30 Open Circuit Voltage (V_{oc}) comparison of 0.5 PRNC with thickness variation

underlying cause can be ascribed to two major assumptions: i) as film thickness decreases more encapsulated filler (rGO) flakes would appear on the surface, in comparison to the same amount of fillers included in thicker film samples, which contributed to the surface roughness, and ii) density of micro-capacitors in thinner film is higher than thicker film-thus induced voltage should be higher in the thinnest nanocomposite films. Hence, all the succeeding films were measured for the thinnest films only.

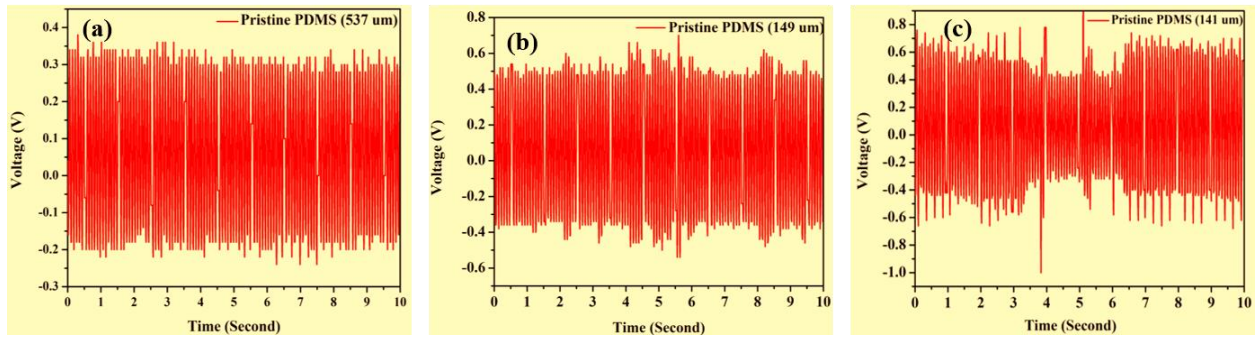


Fig. 31. Open Circuit Voltage (V_{oc}) of PP with (a) 537 μm , (b) 149 μm (c) 141 μm

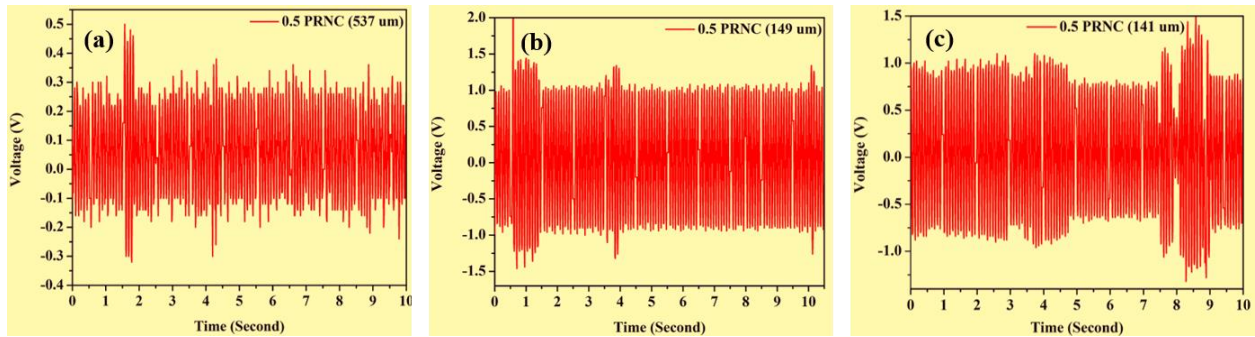


Fig. 32. Open Circuit Voltage (V_{oc}) of 0.5 PRNC with (a) 537 μm , (b) 149 μm (c) 141 μm

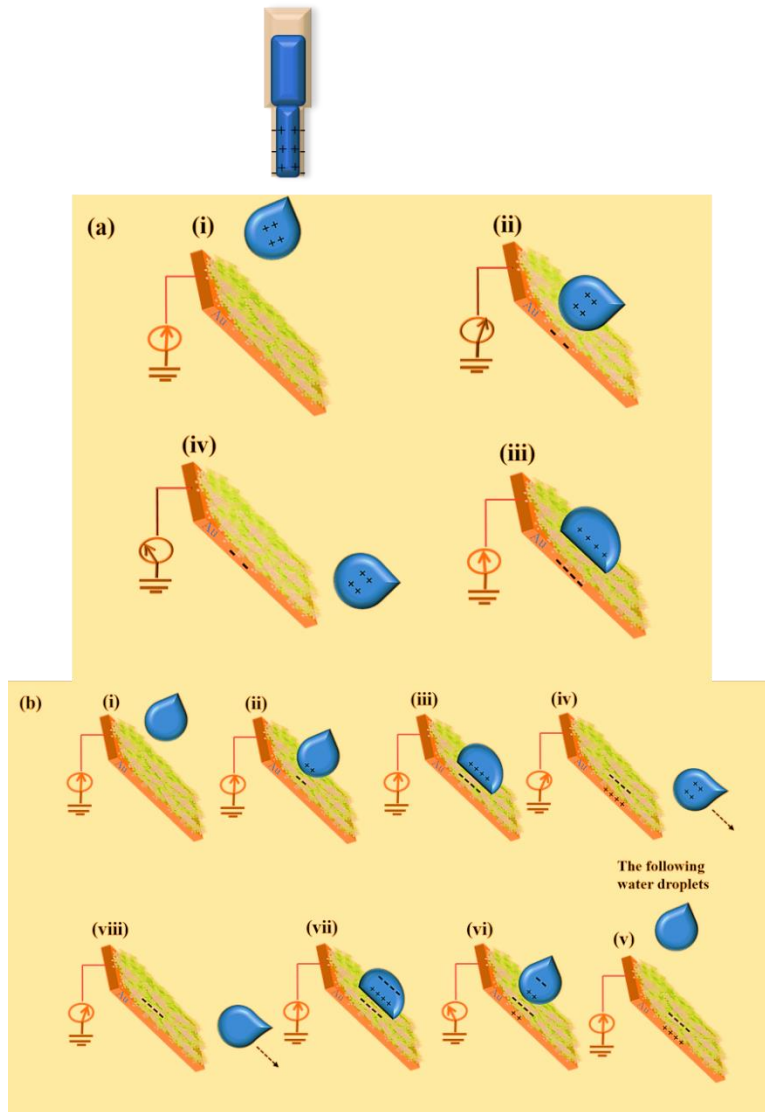
4.2 Working Mechanism

Like all other modes of TENG, the operating principle of this proposed SEM-TENG is based on electrostatic induction and triboelectric effect. The conventional mechanism along with the

enhanced energy storage phenomenon has been explained in detail through a schematic diagram as shown in **Fig. 33(a) (i-iv)**. Firstly, water droplet is charged positively while making contact electrification with the pipette tube (PTFE) from where it was dropped and with air through which it travels towards the targeted triboelectric surface [59]. Since PTFE is highly negative (according to the triboelectric series), therefore it can be assumed that the droplet generated would have contained positive charges in itself. As close as the that charged water droplet approached the prepared triboelectric nanocomposite surface, a positive potential difference was induced between the ground and Au electrode, which consequently made the electrons to flow from ground to Au electrode to nullify the potential difference. However, a negative potential difference was induced between electrode and ground when water droplet completely rolled off the contact surface. In this case the electron flow direction was reverse. It should be noted that the better wrinkled structured surface, 0.5 PRNC film found in the optimization, will assist to complete droplet removal from surface owing to the roughness it introduced.

Fig. 33(b)(i-viii) demonstrated the mechanism of triboelectric phenomenon between nanocomposite surface and sliding water droplet. The triboelectric output can be achieved from the dripping and sliding of droplet over the preferred surface via forming electrical double layer (EDL) between them. Since rGO carries negative charges, as reported by Navjat Kour et al [23], and PDMS is also negative in triboelectric series therefore, it can be inferred that the whole polymer composite will act as a negative surface for energy harvesting. Thus, when the droplet came in contact with nanocomposite surface, surface ionization of nanocomposite occurred. This made the droplet to be positively charged and the surface to be charged negatively. Therefore, electrical neutrality was sustained as long as the droplet kept rolling over the surface. As soon as the droplet left the surface, charge was preserved on the surface due to the nature of dielectric

electret. A negative potential difference was created between electrode and ground, and electron flow was occurred from electrode to ground to neutralize this until the charge equilibrium was achieved. When the following water droplets contacted the surface then uninterrupted output can be gained. This working mechanism has been demonstrated schematically in **Fig. 33 (b) (v-viii)**.



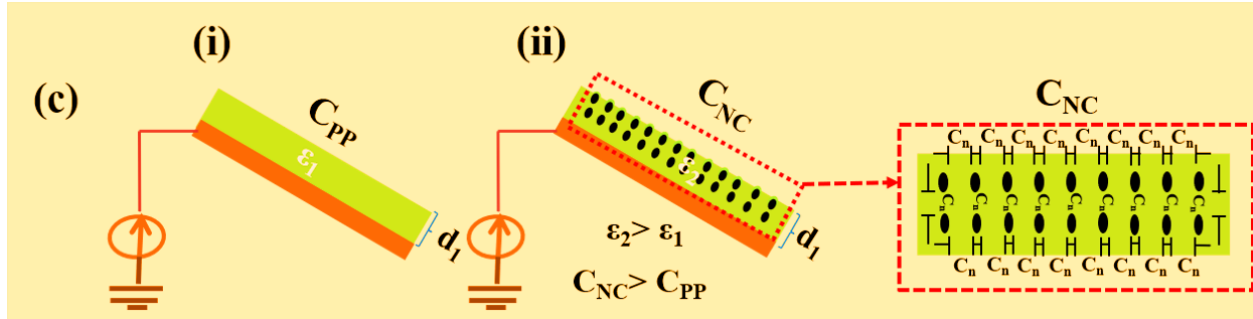


Fig. 33. working mechanism of SEM-TENG device (a) when droplet was pre-charged due to triboelectrification with Pipette/air, (b) when contact electrification occurred between droplet and thin triboelectric films, and (c) micro-capacitor model due to optimized filler addition.

It is also crucial to notice that the water droplet contact outputs showed higher peaks, as marked in dotted rectangle in Fig. 8 (a-f). On the contrary, in the same figure, separation peaks revealed lower output peaks but apparently consistent and lasted longer in most cases. The reason might be attributed to slower separation process, which also matched with the literature of identical phenomenon [59].

This triboelectric effect can be explained further with the variation of filler amount mixed with pure PDMS matrix. A clear performance comparison can be made between PP and filler enhanced nanocomposites based on the capacitance effect. If the polymer is considered in the pristine condition and since its dielectric constant at frequency 60 kHz was known along with the film thickness (141 μm), then the capacitance can be measured with the following equation:

$$C_{PP} = \frac{\epsilon_1 A}{d}$$

Where ϵ_1 = dielectric constant of PP film, A= Area of friction area, and d= film thickness. **Table 7** presented the capacitance value with respect to the dielectric constants measured for each sample films. Calculated capacitance, $C_1=24.39$, indicated the quantitative measurement of charge storage

threshold of PP film upon generation of triboelectric charges when friction occurred between two contact surfaces. These charges cannot move due to higher insulating properties of bulk PDMS electret. Since the charge generation in pristine triboelectric film is affected by the capacitance, it can also be concluded prudently that enhancing this capacitance property would generate more charges on surface. Therefore, to increase the capacitance, it was necessary to tune the bulk matrix of PDMS with fillers. rGO conductive fillers would increase the number of micro-capacitors by forming filler-dielectric-filler structure, as presented in **Fig. 33 (c) (ii)** by changing the dielectric

Table 7. Dielectric Constant and Capacitance of as synthesized films

Dielectric Properties	Pristine PDMS	0.5 PRNC	0.8 PRNC	1.2 PRNC	1.8 PRNC
Dielectric constant	8.6	22.7	12.5	11.5	8.4
Capacitance	24.39	64.4	35.46	32.62	23.83

property and capacitance of the matrix. The capacitance of this new nanocomposite can be estimated by the following equation:

$$C_{NC} = \frac{\epsilon_2 A}{d}$$

Where ϵ_2 = dielectric constant of nanocomposite film. These micro-capacitors enhanced capacitance would enhance the charge density of nanocomposite film under the same friction occurrence. In addition, filler enhanced nanocomposites of same thickness as PP indirectly proved the reduction of pristine polymer film thickness inside the bulk matrix [53]. However, too much addition of fillers can cause agglomeration inside the matrix, which would cause downturn of the capacitance values. Therefore, it was pivotal to check the dielectric properties and the output performance of the proposed TENG to figure out the optimized filler quantity. When low quantity

filler i.e. 0.5 mg was added in the polymer, quite higher capacitance 64.4 was realized than pristine polymer without any filler. This enriched capacitance indicated the better dispersion of filler sheets with minimal thickness and well-formed numerous micro-capacitors throughout the nanocomposite sample that can boost up the output performance. When the voltage is generated due to triboelectrification, these micro-capacitors distributed the voltage among them and potential difference was greatly increased for 0.5 PRNC film compared to PP film, which can be further verified by the open circuit voltage (V_{OC}) results presented in **Fig 26 (a, b)**. V_{OC} was found $\sim 1V$ and $\sim 2V$ for PP and 0.5 PRNC triboelectric films respectively. However, for further increase of filler quantity resulted in downfall of capacitance values. 0.8 PRNC film showed capacitance ~ 35.46 , which was quite lower in comparison to 0.5 PRNC. In this case, filler flakes tempted to merge with each other instead of forming capacitor-like morphology in the matrix. Although the dispersion of fillers was apparently better in many places, lower capacitance ratified the stacking phenomenon of filler sheets in the polymer matrix. As a consequence, V_{OC} ($\sim 1.65 V$) reduced during droplet-nanocomposite surface contact electrification (**Fig. 26 (c)**). Further increment of fillers tended to decrease the capacitance even lower. The reason of which can be attributed to the same phenomenon we mentioned earlier: undesired higher agglomeration and clustered fillers inside the polymer matrix or on the surface. It was worthy to mention that 1.8 PRNC nanocomposite film displayed very close capacitance (~ 8.4) to PP film. Apart from this, the filler flake's thickness drastically increased to $60 \mu m$ for this nanocomposite film. The effects of decreasing capacitance were further followed by decreasing SEM-TENG's performance i.e. $\sim 0.9 V$, $\sim 0.49V$ and $\sim 0.54 V$ for succeeding nanocomposite films, represented in **Fig 26 (d, e, f)**. From this discussion, it can be concluded that 0.5 PRNC is the best optimized triboelectric nanocomposite film that generated more voltage due to its uniform capacitor model as well as

induced surface roughness. The observed output close-circuit current (I_{SC}) for all triboelectric nanocomposite films of uniform thickness (141 μ m) has been presented in **Fig. 34**.

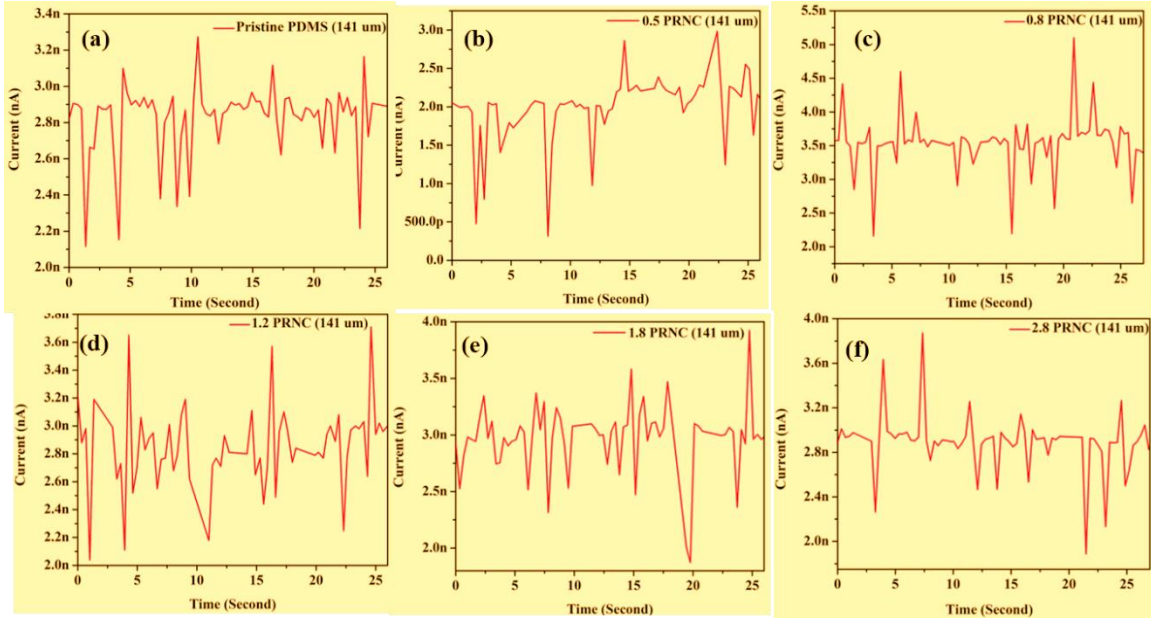


Fig. 34. Close Circuit Current (I_{SC}) of (a) Pristine PDMS, (b) 0.5 PRNC, (c) 0.8 PRNC, (d) 1.2 PRNC, (e) 1.8 PRNC, and (f) 2.8 PRNC

Chapter 5

Conclusion and Future Work Direction

5.1 Conclusion

In brief, we prepared several triboelectric pristine polymer and nanocomposite films to fabricate SEM-TENG devices as well as to test their prospects for droplet-based triboelectrification. Here we varied the amount of fillers to optimize the energy harvesting outputs. While running experiments on these samples, we found that lower filler enhanced nanocomposites showed better dispersion, surface roughness due to wrinkled patterns, higher hydrophobicity, dielectric properties etc. Moreover, the output performance also has been found greater as much as the films became thinner. Through several nano-characterization techniques, dielectric and quantitative output measurements, we also tried to demonstrate that how increasing filler amount beyond a certain extent can cause gradual deterioration of hydrophobic and dielectric properties of the nanocomposite films. Finally, we have successfully concluded that 0.5 PRNC triboelectric film of 141 μm thickness presented superior results e.g. water contact angle 116° , dielectric constant ~ 22.7 , $\sim 0.32 \text{ Sm}^{-1}$, Capacitance ~ 64.4 , $I_{sc} \sim 2 \text{ nA}$ and $V_{OC} = 2 \text{ V}$ in comparison to other thin PP and nanocomposite films. This work represents a very simple and efficient way to harvest triboelectric energy from meagre droplet movement. The electrical energy generated through this triboelectrification can be applied directly to charge capacitors for its subsequent application to power small-scale sensors or electronic devices.

5.2 Future Work Direction

The hydrophobicity improvement is the biggest challenge to implement following merely chemical process. Although the present work has come up with a new aspect of hydrophobicity optimization,

the objective of getting a superhydrophobic surface is the toughest job without further interference. Therefore, in order to make it superhydrophobic or reducing the surface energy to minimum level, the following works can be done-

- Inductive Coupled Plasma-Reactive Ion Etching (ICP-RIE) can be performed on the as synthesized pristine and nanocomposite surfaces, as this will certainly increase surface roughness to higher level
- If certain condition can be applied to grow nanowires on surface, then air diffusion resistance will be increased, which will cause higher water repelling phenomenon following contact as a consequence
- Furthermore, higher etching time can cause damage to filler flakes. In such case, 2/3 minutes etching may possibly remove the polymer layer and may cause the filler flakes appeared on the surface. Then the flakes themselves will induce surface roughness.

5.3 Publications

1. **Abu Naushad Parvez**, Md Habibur Rahaman, Hyeon Cheol Kim, Kyoung Kwan Ahn, “Optimization of Triboelectric Energy Harvesting from Falling Water Droplet on to Wrinkled Polydimethylsiloxane-Reduced Graphene Oxide Nanocomposite Surface”, **Composites Part B: Engineering, Submitted (Currently Under Review)**.
2. Ravi Kumar Cheedarala, **Abu Naushad Parvez**, Kyoung Kwan Ahn, “Electric Impulse Spring Assisted Contact Separation Mode Triboelectric Nanogenerator Fabricated from Polyaniline Emeraldine Salt and Woven Carbon Fibers”, **Nano Energy**, doi: <https://doi.org/10.1016/j.nanoen.2018.08.066>

References

- [1] Lee M, Bae J, Lee J, Lee C-S, Hong S, Wang ZL. Self-powered environmental sensor system driven by nanogenerators. *Energy Environ Sci* 2011;4:3359–63. doi:10.1039/C1EE01558C.
- [2] Wang ZL, Song J. Piezoelectric nanogenerators based on zinc oxide nanowire arrays. *Science* 2006. doi:10.1126/science.1124005.
- [3] Wu W, Pan C, Zhang Y, Wen X, Wang ZL. Piezotronics and piezo-phototronics - From single nanodevices to array of devices and then to integrated functional system. *Nano Today* 2013. doi:10.1016/j.nantod.2013.11.002.
- [4] Lu MP, Song J, Lu MY, Chen MT, Gao Y, Chen LJ, et al. Piezoelectric nanogenerator using p-type ZnO nanowire arrays. *Nano Lett* 2009. doi:10.1021/nl900115y.
- [5] Kim S, Gupta MK, Lee KY, Sohn A, Kim TY, Shin KS, et al. Transparent flexible graphene triboelectric nanogenerators. *Adv Mater* 2014. doi:10.1002/adma.201400172.
- [6] Cheedarala RK, Parvez AN, Ahn KK. Electric impulse spring-assisted contact separation mode triboelectric nanogenerator fabricated from polyaniline emeraldine salt and woven carbon fibers. *Nano Energy* 2018. doi:10.1016/j.nanoen.2018.08.066.
- [7] Fan FR, Lin L, Zhu G, Wu W, Zhang R, Wang ZL. Transparent triboelectric nanogenerators and self-powered pressure sensors based on micropatterned plastic films. *Nano Lett* 2012. doi:10.1021/nl300988z.
- [8] Wang S, Lin L, Xie Y, Jing Q, Niu S, Wang ZL. Sliding-triboelectric nanogenerators based on in-plane charge-separation mechanism. *Nano Lett* 2013. doi:10.1021/nl400738p.
- [9] Yang Y, Jung JH, Yun BK, Zhang F, Pradel KC, Guo W, et al. Flexible pyroelectric nanogenerators using a composite structure of lead-free KNbO₃ nanowires. *Adv Mater* 2012. doi:10.1002/adma.201201414.
- [10] Bowen CR, Taylor J, Lebourbar E, Zabek D, Chauhan A, Vaish R. Pyroelectric materials and devices for energy harvesting applications. *Energy Environ Sci* 2014. doi:10.1039/c4ee01759e.
- [11] Yang Y, Guo W, Pradel KC, Zhu G, Zhou Y, Zhang Y, et al. Pyroelectric nanogenerators for harvesting thermoelectric energy. *Nano Lett* 2012. doi:10.1021/nl3003039.

- [12] Fan FR, Tian ZQ, Lin Wang Z. Flexible triboelectric generator. *Nano Energy* 2012. doi:10.1016/j.nanoen.2012.01.004.
- [13] Wang ZL. Triboelectric nanogenerators as new energy technology and self-powered sensors - Principles, problems and perspectives. *Faraday Discuss* 2014. doi:10.1039/c4fd00159a.
- [14] Wang ZL. Triboelectric nanogenerators as new energy technology for self-powered systems and as active mechanical and chemical sensors. *ACS Nano* 2013. doi:10.1021/nn404614z.
- [15] Yang J, Chen J, Yang Y, Zhang H, Yang W, Bai P, et al. Broadband vibrational energy harvesting based on a triboelectric nanogenerator. *Adv Energy Mater* 2014. doi:10.1002/aenm.201301322.
- [16] Fan X, Chen J, Yang J, Bai P, Li Z, Wang ZL. Ultrathin, rollable, paper-based triboelectric nanogenerator for acoustic energy harvesting and self-powered sound recording. *ACS Nano* 2015. doi:10.1021/acsnano.5b00618.
- [17] Zhu G, Lin ZH, Jing Q, Bai P, Pan C, Yang Y, et al. Toward large-scale energy harvesting by a nanoparticle-enhanced triboelectric nanogenerator. *Nano Lett* 2013. doi:10.1021/nl4001053.
- [18] Wen Z, Chen J, Yeh MH, Guo H, Li Z, Fan X, et al. Blow-driven triboelectric nanogenerator as an active alcohol breath analyzer. *Nano Energy* 2015. doi:10.1016/j.nanoen.2015.06.006.
- [19] Jing Q, Zhu G, Bai P, Xie Y, Chen J, Han RPS, et al. Case-encapsulated triboelectric nanogenerator for harvesting energy from reciprocating sliding motion. *ACS Nano* 2014. doi:10.1021/nn500694y.
- [20] Zhu G, Chen J, Liu Y, Bai P, Zhou YS, Jing Q, et al. Linear-grating triboelectric generator based on sliding electrification. *Nano Lett* 2013. doi:10.1021/nl4008985.
- [21] Niu S, Liu Y, Wang S, Lin L, Zhou YS, Hu Y, et al. Theory of sliding-mode triboelectric nanogenerators. *Adv Mater* 2013. doi:10.1002/adma.201302808.
- [22] Zhang H, Yang Y, Zhong X, Su Y, Zhou Y, Hu C, et al. Single-electrode-based rotating triboelectric nanogenerator for harvesting energy from tires. *ACS Nano* 2014. doi:10.1021/nn4053292.
- [23] Kaur N, Bahadur J, Panwar V, Singh P, Rathi K, Pal K. Effective energy harvesting from a single electrode based triboelectric nanogenerator. *Sci Rep* 2016. doi:10.1038/srep38835.

- [24] Yang Y, Zhang H, Chen J, Jing Q, Zhou YS, Wen X, et al. Single-electrode-based sliding triboelectric nanogenerator for self-powered displacement vector sensor system. *ACS Nano* 2013. doi:10.1021/nm403021m.
- [25] Yang Y, Zhou YS, Zhang H, Liu Y, Lee S, Wang ZL. A single-electrode based triboelectric nanogenerator as self-powered tracking system. *Adv Mater* 2013. doi:10.1002/adma.201302453.
- [26] Niu S, Liu Y, Chen X, Wang S, Zhou YS, Lin L, et al. Theory of freestanding triboelectric-layer-based nanogenerators. *Nano Energy* 2015. doi:10.1016/j.nanoen.2015.01.013.
- [27] Wang S, Xie Y, Niu S, Lin L, Wang ZL. Freestanding triboelectric-layer-based nanogenerators for harvesting energy from a moving object or human motion in contact and non-contact modes. *Adv Mater* 2014. doi:10.1002/adma.201305303.
- [28] Zhou T, Zhang C, Han CB, Fan FR, Tang W, Wang ZL. Woven structured triboelectric nanogenerator for wearable devices. *ACS Appl Mater Interfaces* 2014. doi:10.1021/am504110u.
- [29] Yang W, Chen J, Wen X, Jing Q, Yang J, Su Y, et al. Triboelectrification based motion sensor for human-machine interfacing. *ACS Appl Mater Interfaces* 2014. doi:10.1021/am500864t.
- [30] Pu X, Li L, Liu M, Jiang C, Du C, Zhao Z, et al. Wearable Self-Charging Power Textile Based on Flexible Yarn Supercapacitors and Fabric Nanogenerators. *Adv Mater* 2016. doi:10.1002/adma.201504403.
- [31] Lai YC, Deng J, Zhang SL, Niu S, Guo H, Wang ZL. Single-Thread-Based Wearable and Highly Stretchable Triboelectric Nanogenerators and Their Applications in Cloth-Based Self-Powered Human-Interactive and Biomedical Sensing. *Adv Funct Mater* 2017. doi:10.1002/adfm.201604462.
- [32] Seol ML, Woo JH, Jeon SB, Kim D, Park SJ, Hur J, et al. Vertically stacked thin triboelectric nanogenerator for wind energy harvesting. *Nano Energy* 2015. doi:10.1016/j.nanoen.2014.11.016.
- [33] Yang Y, Zhu G, Zhang H, Chen J, Zhong X, Lin ZH, et al. Triboelectric nanogenerator for harvesting wind energy and as self-powered wind vector sensor system. *ACS Nano* 2013. doi:10.1021/nm4043157.

- [34] Chen B, Yang Y, Wang ZL. Scavenging Wind Energy by Triboelectric Nanogenerators. *Adv Energy Mater* 2018. doi:10.1002/aenm.201702649.
- [35] Khan U, Kim SW. Triboelectric Nanogenerators for Blue Energy Harvesting. *ACS Nano* 2016;10:6429–32. doi:10.1021/acsnano.6b04213.
- [36] Wang ZL, Jiang T, Xu L. Toward the blue energy dream by triboelectric nanogenerator networks. *Nano Energy* 2017;39:9–23. doi:10.1016/j.nanoen.2017.06.035.
- [37] Pradel KC, Jing Q, Wang ZL, Chen J, Yang J, Wen Z, et al. Networks of Triboelectric Nanogenerators for Harvesting Water Wave Energy: A Potential Approach toward Blue Energy. *ACS Nano* 2015;9:3324–31. doi:10.1021/acsnano.5b00534.
- [38] Jing Q, Yang W, Bai P, Wang ZL, Zhu G, Chen J, et al. Harvesting Water Wave Energy by Asymmetric Screening of Electrostatic Charges on a Nanostructured Hydrophobic Thin-Film Surface. *ACS Nano* 2014;8:6031–7. doi:10.1021/nn5012732.
- [39] Bai P, Zhu G, Liu Y, Chen J, Jing Q, Yang W, et al. Cylindrical rotating triboelectric nanogenerator. *ACS Nano* 2013. doi:10.1021/nn402491y.
- [40] Guo H, Chen J, Yeh MH, Fan X, Wen Z, Li Z, et al. An ultrarobust high-performance triboelectric nanogenerator based on charge replenishment. *ACS Nano* 2015. doi:10.1021/acsnano.5b01830.
- [41] Lin L, Wang S, Xie Y, Jing Q, Niu S, Hu Y, et al. Segmentally structured disk triboelectric nanogenerator for harvesting rotational mechanical energy. *Nano Lett* 2013. doi:10.1021/nl4013002.
- [42] Wang ZL, Chen J, Lin L. Progress in triboelectric nanogenerators as a new energy technology and self-powered sensors. *Energy Environ Sci* 2015. doi:10.1039/c5ee01532d.
- [43] Dai K, Wang X, Yi F, Jiang C, Li R, You Z. Triboelectric nanogenerators as self-powered acceleration sensor under high-g impact. *Nano Energy* 2018. doi:10.1016/j.nanoen.2017.12.022.
- [44] Song W, Gan B, Jiang T, Zhang Y, Yu A, Yuan H, et al. Nanopillar Arrayed Triboelectric Nanogenerator as a Self-Powered Sensitive Sensor for a Sleep Monitoring System. *ACS Nano* 2016. doi:10.1021/acsnano.6b04344.
- [45] Bhushan B, Hansford D, Lee KK. Surface modification of silicon and polydimethylsiloxane surfaces with vapor-phase-deposited ultrathin fluorosilane films for biomedical nanodevices. *J Vac Sci Technol Vac Surf Films* 2006. doi:10.1116/1.2167077.

- [46] Chen J, Guo H, He X, Liu G, Xi Y, Shi H, et al. Enhancing Performance of Triboelectric Nanogenerator by Filling High Dielectric Nanoparticles into Sponge PDMS Film. *ACS Appl Mater Interfaces* 2016;8:736–44. doi:10.1021/acsami.5b09907.
- [47] Yang W, Chen J, Wen X, Jing Q, Yang J, Su Y, et al. Triboelectrification based motion sensor for human-machine interfacing. *ACS Appl Mater Interfaces* 2014;6:7479–84. doi:10.1021/am500864t.
- [48] Lin ZH, Cheng G, Lin L, Lee S, Wang ZL. Water-solid surface contact electrification and its use for harvesting liquid-wave energy. *Angew Chem - Int Ed* 2013;52:12545–9. doi:10.1002/anie.201307249.
- [49] Wang S, Xie Y, Niu S, Lin L, Liu C, Zhou YS, et al. Maximum surface charge density for triboelectric nanogenerators achieved by ionized-air injection: Methodology and theoretical understanding. *Adv Mater* 2014. doi:10.1002/adma.201402491.
- [50] Kim MK, Kim MS, Kwon HB, Jo SE, Kim YJ. Wearable triboelectric nanogenerator using a plasma-etched PDMS-CNT composite for a physical activity sensor. *RSC Adv* 2017;7:48368–73. doi:10.1039/c7ra07623a.
- [51] Yang B, Wang L, Wang X, Zhu Y, Liu J, Chen X, et al. A flexible and biocompatible triboelectric nanogenerator with tunable internal resistance for powering wearable devices. *Sci Rep* 2016;6:1–10. doi:10.1038/srep22233.
- [52] Xia X, Chen J, Liu G, Javed MS, Wang X, Hu C. Aligning graphene sheets in PDMS for improving output performance of triboelectric nanogenerator. *Carbon* 2017;111:569–76. doi:10.1016/j.carbon.2016.10.041.
- [53] He X, Guo H, Yue X, Gao J, Xi Y, Hu C. Improving energy conversion efficiency for triboelectric nanogenerator with capacitor structure by maximizing surface charge density. *Nanoscale* 2015;7:1896–903. doi:10.1039/c4nr05512h.
- [54] Harnchana V, Ngoc H Van, He W, Rasheed A, Park H, Amornkitbamrung V, et al. Enhanced Power Output of a Triboelectric Nanogenerator using Poly(dimethylsiloxane) Modified with Graphene Oxide and Sodium Dodecyl Sulfate. *ACS Appl Mater Interfaces* 2018. doi:10.1021/acsami.8b02495.
- [55] Huang T, Lu M, Yu H, Zhang Q, Wang H, Zhu M. Enhanced power output of a triboelectric nanogenerator composed of electrospun nanofiber mats doped with graphene oxide. *Sci Rep* 2015. doi:10.1038/srep13942.

- [56] Tian H, Ma S, Zhao HM, Wu C, Ge J, Xie D, et al. Flexible electrostatic nanogenerator using graphene oxide film. *Nanoscale* 2013. doi:10.1039/c3nr01658g.
- [57] Liu Y, Sun N, Liu J, Wen Z, Sun X, Lee ST, et al. Integrating a Silicon Solar Cell with a Triboelectric Nanogenerator via a Mutual Electrode for Harvesting Energy from Sunlight and Raindrops. *ACS Nano* 2018. doi:10.1021/acsnano.8b00416.
- [58] Jeon SB, Kim D, Yoon GW, Yoon JB, Choi YK. Self-cleaning hybrid energy harvester to generate power from raindrop and sunlight. *Nano Energy* 2015. doi:10.1016/j.nanoen.2015.01.039.
- [59] Lin ZH, Cheng G, Lee S, Pradel KC, Wang ZL. Harvesting water drop energy by a sequential contact-electrification and electrostatic-induction process. *Adv Mater* 2014. doi:10.1002/adma.201400373.
- [60] Li X, Tao J, Zhu J, Pan C. A nanowire based triboelectric nanogenerator for harvesting water wave energy and its applications. *APL Mater* 2017;5. doi:10.1063/1.4977216.
- [61] Zong-Hong Lin, Gang Cheng, Wenzhuo Wu, Ken C. Pradel and ZL. Dual-Mode Triboelectric Nanogenerator for Harvesting Water Energy and as a. *ACS Nano* 2014;8:6440.
- [62] Kwak SS, Lin S, Lee JH, Ryu H, Kim TY, Zhong H, et al. Triboelectrification-Induced Large Electric Power Generation from a Single Moving Droplet on Graphene/Polytetrafluoroethylene. *ACS Nano* 2016. doi:10.1021/acsnano.6b03032.
- [63] Belyaeva LA, van Deursen PMG, Barbetsea KI, Schneider GF. Hydrophilicity of Graphene in Water through Transparency to Polar and Dispersive Interactions. *Adv Mater* 2018. doi:10.1002/adma.201703274.
- [64] Wang W, Zhao C, Li P. Tuning the electronic properties of graphene oxide nanoribbons with armchair edges through lithium doping. *RSC Adv* 2016. doi:10.1039/c6ra06132j.
- [65] Kirubasankar B, Murugadoss V, Lin J, Ding T, Dong M, Liu H, et al. In situ grown nickel selenide on graphene nanohybrid electrodes for high energy density asymmetric supercapacitors. *Nanoscale* 2018;10:20414–25. doi:10.1039/c8nr06345a.
- [66] Le K, Wang Z, Wang F, Wang Q, Shao Q, Murugadoss V, et al. Sandwich-like NiCo Layered Double Hydroxides/Reduced Graphene Oxide Nanocomposite Cathode for High Energy Density Asymmetric Supercapacitors. *Dalton Trans* 2019;48:5193–202. doi:10.1039/c9dt00615j.

- [67] Wu C, Kim TW, Choi HY. Reduced graphene-oxide acting as electron-trapping sites in the friction layer for giant triboelectric enhancement. *Nano Energy* 2017;32:542–50. doi:10.1016/j.nanoen.2016.12.035.
- [68] Zhang J, Zhang Z, Jiao Y, Yang H, Li Y, Zhang J, et al. The graphene/lanthanum oxide nanocomposites as electrode materials of supercapacitors. *J Power Sources* 2019;419:99–105. doi:10.1016/j.jpowsour.2019.02.059.
- [69] Khim Chng EL, Chua CK, Pumera M. Graphene oxide nanoribbons exhibit significantly greater toxicity than graphene oxide nanoplatelets. *Nanoscale* 2014. doi:10.1039/c4nr03608e.
- [70] Huang YX, Liu XW, Xie JF, Sheng GP, Wang GY, Zhang YY, et al. Graphene oxide nanoribbons greatly enhance extracellular electron transfer in bio-electrochemical systems. *Chem Commun* 2011. doi:10.1039/c1cc10159e.
- [71] Zhang J, Li P, Zhang Z, Wang X, Tang J, Liu H, et al. Solvent-free graphene liquids: Promising candidates for lubricants without the base oil. *J Colloid Interface Sci* 2019;542:159–67. doi:10.1016/j.jcis.2019.01.135.
- [72] Zaheer U, Khurram AA, Subhani T. A treatise on multiscale glass fiber epoxy matrix composites containing graphene nanoplatelets. *Adv Compos Hybrid Mater* 2018;1:705–21. doi:10.1007/s42114-018-0057-y.
- [73] Liu M, Meng Q, Yang Z, Zhao X, Liu T. Ultra-long-term cycling stability of an integrated carbon-sulfur membrane with dual shuttle-inhibiting layers of graphene “nets” and a porous carbon skin. *Chem Commun* 2018;54:5090–3. doi:10.1039/c8cc01889h.
- [74] Gu H, Xu X, Dong M, Xie P, Shao Q, Fan R, et al. Carbon nanospheres induced high negative permittivity in nanosilver-polydopamine metacomposites. *Carbon* 2019;147:550–8. doi:10.1016/j.carbon.2019.03.028.
- [75] Wu Z, Gao S, Chen L, Jiang D, Shao Q, Zhang B, et al. Electrically Insulated Epoxy Nanocomposites Reinforced with Synergistic Core–Shell SiO₂@MWCNTs and Montmorillonite Bifillers. *Macromol Chem Phys* 2017;218:1–9. doi:10.1002/macp.201700357.
- [76] Zhu G, Cui X, Zhang Y, Chen S, Dong M, Liu H, et al. Poly (vinyl butyral)/Graphene oxide/poly (methylhydrosiloxane) nanocomposite coating for improved aluminum alloy anticorrosion. *Polymer* 2019;172:415–22. doi:10.1016/j.polymer.2019.03.056.

- [77] Ma R, Wang Y, Qi H, Shi C, Wei G, Xiao L, et al. Nanocomposite sponges of sodium alginate/graphene oxide/polyvinyl alcohol as potential wound dressing: In vitro and in vivo evaluation. *Compos Part B Eng* 2019. doi:10.1016/j.compositesb.2019.03.006.
- [78] Qian Y, Yuan Y, Wang H, Liu H, Zhang J, Shi S, et al. Highly efficient uranium adsorption by salicylaldoxime/polydopamine graphene oxide nanocomposites. *J Mater Chem A* 2018;6:24676–85. doi:10.1039/C8TA09486A.
- [79] Boisseau S, Despesse G, Ahmed B. Electrostatic Conversion for Vibration Energy Harvesting. *Small-Scale Energy Harvest.*, 2012. doi:10.5772/51360.
- [80] Roundy S, Wright PK, Rabaey J. A study of low level vibrations as a power source for wireless sensor nodes. *Comput Commun* 2003;26:1131–44. doi:10.1016/S0140-3664(02)00248-7.
- [81] Cook-Chennault KA, Thambi N, Sastry AM. Powering MEMS portable devices—a review of non-regenerative and regenerative power supply systems with special emphasis on piezoelectric energy harvesting systems. *Smart Mater Struct* 2008;17:043001. doi:10.1088/0964-1726/17/4/043001.
- [82] Beeby SP, Tudor MJ, White NM. Energy harvesting vibration sources for microsystems applications. *Meas Sci Technol* 2006;17:R175–95. doi:10.1088/0957-0233/17/12/R01.
- [83] Zou H, Chen H, Zhu X. Piezoelectric energy harvesting from vibrations induced by jet-resonator system. *Mechatronics* 2015;26:29–35. doi:10.1016/j.mechatronics.2015.01.002.
- [84] Piezoelectric energy harvesting from hybrid vibrations - IOPscience n.d. <https://iopscience.iop.org/article/10.1088/0964-1726/23/2/025026/meta> (accessed April 6, 2019).
- [85] A review on energy harvesting approaches for renewable energies from ambient vibrations and acoustic waves using piezoelectricity - IOPscience n.d. <https://iopscience.iop.org/article/10.1088/1361-665X/aa7bfb/meta> (accessed April 6, 2019).
- [86] A micro electromagnetic generator for vibration energy harvesting - IOPscience n.d. <https://iopscience.iop.org/article/10.1088/0960-1317/17/7/007> (accessed April 6, 2019).
- [87] Bouendeu E, Greiner A, Smith PJ, Korvink JG. A Low-Cost Electromagnetic Generator for Vibration Energy Harvesting. *IEEE Sens J* 2011;11:107–13. doi:10.1109/JSEN.2010.2050310.

- [88] Chae SH, Ju S, Choi Y, Chi Y-E, Ji C-H. Electromagnetic Linear Vibration Energy Harvester Using Sliding Permanent Magnet Array and Ferrofluid as a Lubricant. *Micromachines* 2017;8. doi:10.3390/mi8100288.
- [89] Zhang Y, Wang T, Zhang A, Peng Z, Luo D, Chen R, et al. Electrostatic energy harvesting device with dual resonant structure for wideband random vibration sources at low frequency. *Rev Sci Instrum* 2016;87:125001. doi:10.1063/1.4968811.
- [90] Madinei H, Khodaparast HH, Adhikari S, Friswell MI. A Hybrid Piezoelectric and Electrostatic Vibration Energy Harvester. In: Brandt A, Singhal R, editors. *Shock Vib. Aircraft/Aerospace Energy Harvest. Acoust. Opt. Vol. 9*, Springer International Publishing; 2016, p. 189–95.
- [91] Goldemberg J. The promise of clean energy. *Energy Policy* 2006;34:2185–90. doi:10.1016/j.enpol.2005.03.009.
- [92] Kvemdokk S. Depletion of fossil fuels and the impacts of global warming, 2003.
- [93] McGlade C, Ekins P. The geographical distribution of fossil fuels unused when limiting global warming to 2 °C. *Nature* 2015;517:187–90. doi:10.1038/nature14016.
- [94] Phase-out of incandescent light bulbs. Wikipedia 2019.
- [95] Anton SR, Sodano HA. A review of power harvesting using piezoelectric materials (2003–2006). *Smart Mater Struct* 2007;16:R1–R21. doi:10.1088/0964-1726/16/3/R01.
- [96] Liu H, Zhong J, Lee C, Lee S-W, Lin L. A comprehensive review on piezoelectric energy harvesting technology: Materials, mechanisms, and applications. *Appl Phys Rev* 2018;5:041306. doi:10.1063/1.5074184.
- [97] Fang J, Wang X, Lin T. Electrical power generator from randomly oriented electrospun poly(vinylidene fluoride) nanofibre membranes. *J Mater Chem* 2011;21:11088–91. doi:10.1039/C1JM11445J.
- [98] The effect of RGO on dielectric and energy harvesting properties of P(VDF-TrFE) matrix by optimizing electroactive b phase without traditional polling process n.d.
- [99] Pan C-T, Yen C-K, Wang S-Y, Lai Y-C, Lin L, Huang JC, et al. Near-field electrospinning enhances the energy harvesting of hollow PVDF piezoelectric fibers. *RSC Adv* 2015;5:85073–81. doi:10.1039/C5RA16604G.

- [100] Lee J-H, Yoon H-J, Kim TY, Gupta MK, Lee JH, Seung W, et al. Micropatterned P(VDF-TrFE) Film-Based Piezoelectric Nanogenerators for Highly Sensitive Self-Powered Pressure Sensors. *Adv Funct Mater* 2015;25:3203–9. doi:10.1002/adfm.201500856.
- [101] Anton S, Farinholt K, Erturk A. Piezoelectret foam-based vibration energy harvesting. *J Intell Mater Syst Struct* 2014;25:1681–92. doi:10.1177/1045389X14541501.
- [102] Wang X, Mao Y, Zhao P. Nanoporous piezoelectric polymer films for mechanical energy harvesting. US9444030B2, 2016.
- [103] Kar-Gupta R, Venkatesh TA. Electromechanical response of porous piezoelectric materials: Effects of porosity distribution. *Appl Phys Lett* 2007;91:062904. doi:10.1063/1.2766960.
- [104] Emirates Aviation University, Aljadiri RT, Taha LY, Windsor University, Ivey P, Birmingham City University. Electrostatic Energy Harvesting Systems: A Better Understanding of Their Sustainability. *J Clean Energy Technol* 2017;5:409–16. doi:10.18178/JOCET.2017.5.5.407.
- [105] Khan FU, Qadir MU. State-of-the-art in vibration-based electrostatic energy harvesting. *J Micromechanics Microengineering* 2016;26:103001. doi:10.1088/0960-1317/26/10/103001.
- [106] Sterken T, Baert K, Puers R, Borghs G. Power extraction from ambient vibration. Proc. SAFE-ProRISC-SeSens, Dutch Technology Foundation STW; 2001.
- [107] Beeby SP, O'Donnell T. Electromagnetic Energy Harvesting. In: Priya S, Inman DJ, editors. *Energy Harvest. Technol.*, Boston, MA: Springer US; 2009, p. 129–61. doi:10.1007/978-0-387-76464-1_5.
- [108] Du Toit NE. Modeling and design of a MEMS piezoelectric vibration energy harvester. Thesis. Massachusetts Institute of Technology, 2005.
- [109] Fan F-R, Tian Z-Q, Lin Wang Z. Flexible triboelectric generator. *Nano Energy* 2012;1:328–34. doi:10.1016/j.nanoen.2012.01.004.
- [110] Wang ZL, Chen J, Lin L. Progress in triboelectric nanogenerators as a new energy technology and self-powered sensors. *Energy Environ Sci* 2015;8:2250–82. doi:10.1039/C5EE01532D.
- [111] Wang Z, Lin L, Chen J, Niu S, Zi Y. *Triboelectric Nanogenerators*. Springer International Publishing; 2016.

- [112] Shin S-Y, Saravanakumar B, Ramadoss A, Kim SJ. Fabrication of PDMS-based triboelectric nanogenerator for self-sustained power source application. *Int J Energy Res* 2016;40:288–97. doi:10.1002/er.3376.
- [113] Musa UG, Cezan SD, Baytekin B, Baytekin HT. The Charging Events in Contact-Separation Electrification. *Sci Rep* 2018;8:2472. doi:10.1038/s41598-018-20413-1.
- [114] Galembeck F, Burgo TAL, Balestrin LBS, Gouveia RF, Silva CA, Galembeck A. Friction, tribochemistry and triboelectricity: recent progress and perspectives. *RSC Adv* 2014;4:64280–98. doi:10.1039/C4RA09604E.
- [115] Diaz AF, Felix-Navarro RM. A semi-quantitative tribo-electric series for polymeric materials: the influence of chemical structure and properties. *J Electrostat* 2004;62:277–90. doi:10.1016/j.elstat.2004.05.005.
- [116] Electrostatic Charging Due to Separation of Ions at Interfaces: Contact Electrification of Ionic Electrets - McCarty - 2008 - *Angewandte Chemie International Edition* - Wiley Online Library n.d. <https://onlinelibrary.wiley.com/doi/full/10.1002/anie.200701812> (accessed April 11, 2019).
- [117] Lowell J. Constraints on contact charging of insulators. I. Spatial localisation of insulator states. *J Phys Appl Phys* 1986;19:95–104. doi:10.1088/0022-3727/19/1/014.
- [118] Liu C, Bard AJ. Electrons on dielectrics and contact electrification. *Chem Phys Lett* 2009;480:145–56. doi:10.1016/j.cplett.2009.08.045.
- [119] Liu C, Bard AJ. Electrostatic electrochemistry at insulators. *Nat Mater* 2008;7:505–9. doi:10.1038/nmat2160.
- [120] McCarty LS, Winkleman A, Whitesides GM. Ionic Electrets: Electrostatic Charging of Surfaces by Transferring Mobile Ions upon Contact. *J Am Chem Soc* 2007;129:4075–88. doi:10.1021/ja067301e.
- [121] Soh S, Liu H, Cademartiri R, Yoon HJ, Whitesides GM. Charging of Multiple Interacting Particles by Contact Electrification. *J Am Chem Soc* 2014;136:13348–54. doi:10.1021/ja506830p.
- [122] Cheedarala RK, Duy LC, Ahn KK. Double characteristic BNO-SPI-TENGs for robust contact electrification by vertical contact separation mode through ion and electron charge transfer. *Nano Energy* 2018;44:430–7. doi:10.1016/j.nanoen.2017.12.019.

- [123] Williams MW. Triboelectric charging of insulating polymers—some new perspectives. *AIP Adv* 2012;2:010701. doi:10.1063/1.3687233.
- [124] Pence S, Novotny VJ, Diaz AF. Effect of Surface Moisture on Contact Charge of Polymers Containing Ions. *Langmuir* 1994;10:592–6. doi:10.1021/la00014a042.
- [125] Salaneck WR, Paton A, Clark DT. Double mass transfer during polymer-polymer contacts. *J Appl Phys* 1976;47:144–7. doi:10.1063/1.322306.
- [126] Baytekin HT, Patashinski AZ, Branicki M, Baytekin B, Soh S, Grzybowski BA. The Mosaic of Surface Charge in Contact Electrification. *Science* 2011;333:308–12. doi:10.1126/science.1201512.
- [127] Wen Z, Fu J, Han L, Liu Y, Peng M, Zheng L, et al. Toward self-powered photodetection enabled by triboelectric nanogenerators. *J Mater Chem C* 2018;6:11893–902. doi:10.1039/C8TC02964D.
- [128] Chen J, Wang ZL. Reviving Vibration Energy Harvesting and Self-Powered Sensing by a Triboelectric Nanogenerator. *Joule* 2017;1:480–521. doi:10.1016/j.joule.2017.09.004.
- [129] Henniker J. Triboelectricity in Polymers. *Nature* 1962;196:474. doi:10.1038/196474a0.
- [130] Contact electrification of insulating materials - IOPscience n.d. <https://iopscience.iop.org/article/10.1088/0022-3727/44/45/453001/meta> (accessed April 23, 2019).
- [131] Niu S, Wang S, Lin L, Liu Y, Zhou YS, Hu Y, et al. Theoretical study of contact-mode triboelectric nanogenerators as an effective power source. *Energy Environ Sci* 2013;6:3576–83. doi:10.1039/C3EE42571A.
- [132] Niu S, Liu Y, Wang S, Lin L, Zhou YS, Hu Y, et al. Theoretical Investigation and Structural Optimization of Single-Electrode Triboelectric Nanogenerators. *Adv Funct Mater* 2014;24:3332–40. doi:10.1002/adfm.201303799.
- [133] Hou T-C, Yang Y, Zhang H, Chen J, Chen L-J, Lin Wang Z. Triboelectric nanogenerator built inside shoe insole for harvesting walking energy. *Nano Energy* 2013;2:856–62. doi:10.1016/j.nanoen.2013.03.001.
- [134] Cui S, Zheng Y, Liang J, Wang D. Triboelectrification based on double-layered polyaniline nanofibers for self-powered cathodic protection driven by wind. *Nano Res* 2018;11:1873–82. doi:10.1007/s12274-017-1805-y.

- [135] Xie Y, Wang S, Lin L, Jing Q, Lin Z-H, Niu S, et al. Rotary Triboelectric Nanogenerator Based on a Hybridized Mechanism for Harvesting Wind Energy. *ACS Nano* 2013;7:7119–25. doi:10.1021/nn402477h.
- [136] Zhu G, Chen J, Zhang T, Jing Q, Wang ZL. Radial-arrayed rotary electrification for high performance triboelectric generator. *Nat Commun* 2014;5:3426. doi:10.1038/ncomms4426.
- [137] Zhao XJ, Zhu G, Fan YJ, Li HY, Wang ZL. Triboelectric Charging at the Nanostructured Solid/Liquid Interface for Area-Scalable Wave Energy Conversion and Its Use in Corrosion Protection. *ACS Nano* 2015;9:7671–7. doi:10.1021/acs.nano.5b03093.
- [138] Wen X, Yang W, Jing Q, Wang ZL. Harvesting Broadband Kinetic Impact Energy from Mechanical Triggering/Vibration and Water Waves. *ACS Nano* 2014;8:7405–12. doi:10.1021/nn502618f.
- [139] Su Y, Wen X, Zhu G, Yang J, Chen J, Bai P, et al. Hybrid triboelectric nanogenerator for harvesting water wave energy and as a self-powered distress signal emitter. *Nano Energy* 2014;9:186–95. doi:10.1016/j.nanoen.2014.07.006.
- [140] Xiao TX, Jiang T, Zhu JX, Liang X, Xu L, Shao JJ, et al. Silicone-Based Triboelectric Nanogenerator for Water Wave Energy Harvesting. *ACS Appl Mater Interfaces* 2018;10:3616–23. doi:10.1021/acsami.7b17239.
- [141] Xu L, Jiang T, Lin P, Shao JJ, He C, Zhong W, et al. Coupled Triboelectric Nanogenerator Networks for Efficient Water Wave Energy Harvesting. *ACS Nano* 2018;12:1849–58. doi:10.1021/acs.nano.7b08674.
- [142] Li X, Tao J, Wang X, Zhu J, Pan C, Wang ZL. Networks of High Performance Triboelectric Nanogenerators Based on Liquid–Solid Interface Contact Electrification for Harvesting Low-Frequency Blue Energy. *Adv Energy Mater* 2018;8:1800705. doi:10.1002/aenm.201800705.
- [143] Yatsuzuka K, Mizuno Y, Asano K. Electrification phenomena of pure water droplets dripping and sliding on a polymer surface. *J Electrostat* 1994;32:157–71. doi:10.1016/0304-3886(94)90005-1.
- [144] Zheng L, Lin Z-H, Cheng G, Wu W, Wen X, Lee S, et al. Silicon-based hybrid cell for harvesting solar energy and raindrop electrostatic energy. *Nano Energy* 2014;9:291–300. doi:10.1016/j.nanoen.2014.07.024.

- [145] Kanik M, Marcali M, Yunusa M, Elbuken C, Bayindir M. Continuous Triboelectric Power Harvesting and Biochemical Sensing Inside Poly(vinylidene fluoride) Hollow Fibers Using Microfluidic Droplet Generation. *Adv Mater Technol* 2016;1:1600190. doi:10.1002/admt.201600190.
- [146] Choi D, Kim DW, Yoo D, Cha KJ, La M, Kim DS. Spontaneous occurrence of liquid-solid contact electrification in nature: Toward a robust triboelectric nanogenerator inspired by the natural lotus leaf. *Nano Energy* 2017;36:250–9. doi:10.1016/j.nanoen.2017.04.026.
- [147] Chen G, Liu X, Li S, Dong M, Jiang D. A droplet energy harvesting and actuation system for self-powered digital microfluidics. *Lab Chip* 2018;18:1026–34. doi:10.1039/C7LC01259D.
- [148] Zhang Q, Liang Q, Liao Q, Ma M, Gao F, Zhao X, et al. An Amphiphobic Hydraulic Triboelectric Nanogenerator for a Self-Cleaning and Self-Charging Power System. *Adv Funct Mater* 2018;28:1803117. doi:10.1002/adfm.201803117.
- [149] Gu H, Zhang H, Ma C, Sun H, Liu C, Dai K, et al. Smart strain sensing organic-inorganic hybrid hydrogels with nano barium ferrite as the cross-linker. *J Mater Chem C* 2019. doi:10.1039/c8tc05448g.
- [150] Hu Q, Zhou N, Gong K, Liu H, Liu Q, Sun D, et al. Intracellular Polymer Substances Induced Conductive Polyaniline for Improved Methane Production from Anaerobic Wastewater Treatment. *ACS Sustain Chem Eng* 2019. doi:10.1021/acssuschemeng.8b05847.
- [151] Chen Q, Yin Q, Dong A, Gao Y, Qian Y, Wang D, et al. Metal complex hybrid composites based on fullerene-bearing porous polycarbazole for H₂, CO₂ and CH₄ uptake and heterogeneous hydrogenation catalysis. *Polymer* 2019. doi:10.1016/j.polymer.2019.02.056.
- [152] Shang J, Zhang Y, Yu L, Luan X, Shen B, Zhang Z, et al. Fabrication and enhanced dielectric properties of graphene-polyvinylidene fluoride functional hybrid films with a polyaniline interlayer. *J Mater Chem A* 2013. doi:10.1039/c2ta00602b.
- [153] Habibur RM, Yaqoob U, Muhammad S, Uddin ASMI, Kim HC. The effect of RGO on dielectric and energy harvesting properties of P(VDF-TrFE) matrix by optimizing electroactive β phase without traditional polling process. *Mater Chem Phys* 2018. doi:10.1016/j.matchemphys.2018.05.010.

- [154] Feng H, Li Y, Li J. Strong reduced graphene oxide-polymer composites: Hydrogels and wires. *RSC Adv* 2012. doi:10.1039/c2ra20644g.
- [155] Sinani VA, Gheith MK, Yaroslavov AA, Rakhnyanskaya AA, Sun K, Mamedov AA, et al. Aqueous dispersions of single-wall and multiwall carbon nanotubes with designed amphiphilic polycations. *J Am Chem Soc* 2005. doi:10.1021/ja045670+.
- [156] Ciambelli P, Cirillo C, Casa M, Adami R, Georgiev V, Petrova-Doycheva I, et al. Effects of Graphene Nanoplatelets and Multiwall Carbon Nanotubes on the Structure and Mechanical Properties of Poly(lactic acid) Composites: A Comparative Study. *Appl Sci* 2019;9:469. doi:10.3390/app9030469.
- [157] Ferrari AC, Meyer JC, Scardaci V, Casiraghi C, Lazzeri M, Mauri F, et al. Raman spectrum of graphene and graphene layers. *Phys Rev Lett* 2006;97:1–4. doi:10.1103/PhysRevLett.97.187401.
- [158] Sun K, Xie P, Wang Z, Su T, Shao Q, Ryu JE, et al. Flexible polydimethylsiloxane/multiwalled carbon nanotubes membranous metacomposites with negative permittivity. *Polymer* 2017. doi:10.1016/j.polymer.2017.07.083.
- [159] Rajitha G, Dash RK. Optically transparent and high dielectric constant reduced graphene oxide (RGO)-PDMS based flexible composite for wearable and flexible sensors. *Sens Actuators Phys* 2018. doi:10.1016/j.sna.2018.04.040.
- [160] Shahzad MI, Giorcelli M, Shahzad N, Guastella S, Castellino M, Jagdale P, et al. Study of carbon nanotubes based Polydimethylsiloxane composite films. *J. Phys. Conf. Ser.*, 2013. doi:10.1088/1742-6596/439/1/012010.
- [161] Tong W, Zhang Y, Yu L, Luan X, An Q, Zhang Q, et al. Novel method for the fabrication of flexible film with oriented arrays of graphene in poly(vinylidene fluoride-co-hexafluoropropylene) with low dielectric loss. *J Phys Chem C* 2014. doi:10.1021/jp411828e.
- [162] Kumar P, Kumar A, Cho KY, Das TK, Sudarsan V. An asymmetric electrically conducting self-aligned graphene/polymer composite thin film for efficient electromagnetic interference shielding. *AIP Adv* 2017;7. doi:10.1063/1.4973535.
- [163] Zhang L, Shan X, Bass P, Tong Y, Rolin TD, Hill CW, et al. Process and Microstructure to Achieve Ultra-high Dielectric Constant in Ceramic-Polymer Composites. *Sci Rep* 2016. doi:10.1038/srep35763.

- [164] Xia X, Zhong Z, Weng GJ. Maxwell–Wagner–Sillars mechanism in the frequency dependence of electrical conductivity and dielectric permittivity of graphene-polymer nanocomposites. *Mech Mater* 2017;109:42–50. doi:10.1016/j.mechmat.2017.03.014.